UC Santa Barbara
UC Santa Barbara Electronic Theses and Dissertations

Title
Exciton Diffusion Length in Solution-Processed Small Molecules

Permalink
https://escholarship.org/uc/item/1wx6n5t1

Author
Lin, Jason

Publication Date
2014

Peer reviewed|Thesis/dissertation

eScholarship.org
Powered by the California Digital Library
University of California

UNIVERSITY OF CALIFORNIA

Santa Barbara

Exciton Diffusion Length in Solution-Processed Small Molecules

A dissertation submitted in partial satisfaction of the
requirements for the degree Doctor of Philosophy
in Chemistry

by

Jason Lin

Committee in charge:
Professor Thuc-Quyen Nguyen, Chair
Professor Guillermo C. Bazan
Professor Fred Wudl
Professor Michael L. Chabinyc

December 2014

The dissertation of Jason Lin is approved.

Michael L. Chabinyc

Guillermo C. Bazan

Fred Wudl

Thuc-Quyen Nguyen, Committee Chair

November 2014

Exciton Diffusion Length in Solution-Processed Small Molecules

Copyright © 2014

by

Jason Lin

ACKNOWLEDGEMENTS

I would not be here today without the continued support for my advisor, professor Thuc-Quyen Nguyen. Thank you for always believing in me and pushing me to be my very best. I would also like to thank my committee members, professor Guillermo C. Bazan, professor Fred Wudl, and professor Michael L. Chabinyc for serving as my committee members. In addition, I would like to thank the National Science Foundation (NSF) Division of Materials Research, NSF-SOLAR for the financial support.

A special thanks goes to my many colleagues at UCSB. This dissertation would not be possible without our many discussions and collaborations. Thank you to my UCLA friends who never stop believing in me from the start to end. I am extremely grateful to Hee-won Kim whom has supported me during the most challenging times of my graduate career. Most of all, thank you Mom, Dad, and Michael. Your continued support and love gave me the strength to overcome my struggles academically and physically early in my life making this day possible.

Thank you all for being there for me when it mattered most.

VITA OF JASON LIN

Nov 2014

EDUCATION

University of California, Santa Barbara (UCSB)
Ph.D., Chemistry, expected November 2014
Dissertation: Exciton Diffusion Length in Organic Semiconductors
Advisor: Prof. Thuc-Quyen Nguyen

University of California, Los Angeles (UCLA)
B.S., Physical Chemistry, 2008
Project: Encapsulation of Fluorescent Polymers by Cowpea Chlorotic Mottle Virus
Advisor: Sarah H. Tolbert

PROFESSIONAL EMPLOYMENT

Teaching Assistant, Department of Chemistry and Biochemistry University of California, Santa Barbara. 2008-2014

PUBLICATIONS

(1) Lin, J. D. A.; Mikhnenko, O. V.; Poll, T. S. van der; Bazan, G. C.; Nguyen, T. Temperature Dependence of Exciton Diffusion in a Small Molecule Organic Semiconductor Processed With and Without Additive. Adv. Mater. 2014, (Submitted).
(2) Guide, M.; Lin, J. D. A.; Proctor, C. M.; Chen, J.; García-Cervera, C.; Nguyen, T.-Q. Effect of Copper Metalation of Tetrabenzoporphyrin Donor Material on Organic Solar Cell Performance. J. Mater. Chem. A 2014, 2, 7890–7896.
(3) Lin, J. D. A.; Liu, J.; Kim, C.; Tamayo, A. B.; Proctor, C. M.; Nguyen, T.-Q. T. Effect of Structural Variation on Photovoltaic Characteristics of Phenyl Substituted Diketopyrrolopyrroles. RSC Adv. 2014, 4, 14101–14108.
(4) Lin, J. D. A.; Mikhnenko, O. V.; Chen, J.; Masri, Z.; Ruseckas, A.; Mikhailovsky, A.; Raab, R. P.; Liu, J.; Blom, P. W. M.; Loi, M. A.; et al. Systematic Study of Exciton Diffusion Length in Organic Semiconductors by Six Experimental Methods. Mater. Horiz. 2014, 1, 280–285.
(5) Walker, B.; Liu, J.; Kim, C.; Welch, G. C.; Park, J. K.; Lin, J.; Zalar, P.; Proctor, C. M.; Seo, J. H.; Bazan, G. C.; et al. Optimization of Energy Levels by Molecular Design: Evaluation of Bis-Diketopyrrolopyrrole Molecular Donor Materials for Bulk Heterojunction Solar Cells. Energy Environ. Sci. 2013, 6, 952–962.
(6) Mikhnenko, O. V.; Kuik, M.; Lin, J.; van der Kaap, N.; Nguyen, T.-Q.; Blom, P. W. M. Trap-Limited Exciton Diffusion in Organic Semiconductors. Adv. Mater. 2013, 1–6.
(7) Liu, J.; Sun, Y.; Moonsin, P.; Kuik, M.; Proctor, C. M.; Lin, J.; Hsu, B. B.; Promarak, V.; Heeger, A. J.; Nguyen, T.-Q. Tri-Diketopyrrolopyrrole Molecular Donor Materials

for High-Performance Solution-Processed Bulk Heterojunction Solar Cells. Adv. Mater. 2013, 25, 5898–5903.

(8) Zhang, Y.; Kim, C.; Lin, J.; Nguyen, T. Solution-Processed Ambipolar Field-Effect Transistor Based on Diketopyrrolopyrrole Functionalized with Benzothiadiazole. Adv. Funct. Mater. 2012, 22, 97–105.

(9) Mikhnenko, O. V.; Lin, J.; Shu, Y.; Anthony, J. E.; Blom, P. W. M.; Nguyen, T.-Q.; Loi, M. A. Effect of Thermal Annealing on Exciton Diffusion in a Diketopyrrolopyrrole Derivative. Phys. Chem. Chem. Phys. 2012, 14, 14196–14201.

(10) Kim, C.; Liu, J.; Lin, J.; Tamayo, A. B.; Walker, B.; Wu, G.; Nguyen, T.-Q. Influence of Structural Variation on the Solid-State Properties of Diketopyrrolopyrrole-Based Oligophenylenethiophenes: Single-Crystal Structures, Thermal Properties, Optical Bandgaps, Energy Levels, Film Morphology, and Hole Mobility. Chem Mater 2012, 24, 1699–1709.

(11) Duong, D. T.; Walker, B.; Lin, J.; Kim, C.; Love, J.; Purushothaman, B.; Anthony, J. E.; Nguyen, T.-Q. Molecular Solubility and Hansen Solubility Parameters for the Analysis of Phase Separation in Bulk Heterojunctions. J. Polym. Sci. Part B Polym. Phys. 2012, 50, 1405–1413.

(12) Ng, B. C.; Chan, S. T.; Lin, J.; Tolbert, S. H. Using Polymer Conformation to Control Architecture in Semiconducting Polymer/Viral Capsid Assemblies. ACS Nano 2011.

AWARDS

- Nominated for Teaching Assistant Award, University of California, Santa Barbara. 2013.
- Excellence in Mentoring Undergraduates in Scientific Research Award, University of
- California, Santa Barbara, 2012.
- Material Research Laboratory Travel Fellowship, University of California, Santa Barbara. 2010.
- Phi Lambda Upsilon Award, University of California, Santa Barbara, 2009.
- Nominated for Teaching Assistant Award, University of California, Santa Barbara. 2009.

ORAL PRESENTATIONS

- Dependence of Exciton Diffusion Length on Measurement Technique and Chemical Structure, Annual UCSB-SCUT Workshop in University of California, Santa Barbara, 2012.
- Effect of structural variation on material properties and photovoltaic characteristics of phenyl substituted diketopyrrolopyrroles, 53rd Electronic Materials Conference in University of California, Santa Barbara, 2011.

ABSTRACT

Exciton Diffusion Length in Solution-Processed Small Molecules

by

Jason Lin

Organic photovoltaic (OPV) devices have the potential to be a cost-efficient, clean, and renewable energy source. A fundamental process in OPV devices which directly impacts the device performance is the diffusion length of Coulombically bound electron-hole pairs or excitons. It is therefore important to investigate how chemical structure and processing conditions impact the exciton diffusion length. This study is difficult to perform with the current body of literature since compounds in separate works differ by a number of chemical modifications. Comparisons between works are further complicated by the use of different techniques to measure the exciton diffusion length. To resolve these issues, the first aim of this dissertation is to compare the fabrication, measurement, and analysis procedure for six different techniques to measure exciton diffusion length. We find that bulk quenching techniques are preferred over surface quenching techniques which require elaborate fabrication procedures, multiple measurements, and a number of assumptions in the analysis process. The second aim of this dissertation is to investigate how chemical structure and processing conditions impact the exciton diffusion length. We find that decreasing the conjugation length in a small molecule leads to an enhancement in the exciton diffusion length while replacing the linear alkyl chains with bulky ethyl hexyl groups has no significant effect. Lastly, we show that processing films with a high boiling point solvent leads to an enhancement in the exciton trap density which directly reduces the exciton diffusion length.

TABLE OF CONTENTS

Permissions

Lin, J. D. A.; Liu, J.; Kim, C.; Tamayo, A. B.; Proctor, C. M.; Nguyen, T.-Q. T. Effect of Structural Variation on Photovoltaic Characteristics of Phenyl Substituted Diketopyrrolopyrroles. RSC Adv. 2014, 4, 14101–14108.- Reproduced by permission of The Royal Society of Chemistry (RSC) on behalf of the Centre National de la Recherche Scientifique (CNRS) and the RSC

Lin, J. D. A.; Mikhnenko, O. V.; Chen, J.; Masri, Z.; Ruseckas, A.; Mikhailovsky, A.; Raab, R. P.; Liu, J.; Blom, P. W. M.; Loi, M. A.; et al. Systematic Study of Exciton Diffusion Length in Organic Semiconductors by Six Experimental Methods. Mater. Horiz. 2014, 1, 280–285. - Reproduced by permission of The Royal Society of Chemistry (RSC) on behalf of the Centre National de la Recherche Scientifique (CNRS) and the RSC

Chapter 1. Introduction

1.1 Overview

Organic Photovoltaics have the potential to be a clean and cost effective energy source. Efficiencies up to 8.62% have been achieved.[1] One advantage of OPVs is that the compounds can be synthesized to be solution processable thereby enabling low-cost, large area processing techniques such as screen printing,[2] doctor blading,[3] ink-jet printing,[4] and spray coating.[5] However, there must be further improvements in OPV efficiencies in order to make them competitive with inorganic solar cells and realize commercialization. This requires a better understanding of how chemical structure impacts the optical, physical, and electrical properties.

1.2 Energy Levels in Organic Semiconductors

An organic semiconductor is a material mainly composed of carbon and hydrogen with an electrical conductivity between that of insulators and that of metals. In organic semiconductors the pi orbitals on the carbons interact with one another creating an equal number of molecular energy levels as described by molecular orbital theory.[6] The carbon atom is a source of electrons for filling the lowest-energy molecular orbital to the highest molecular orbital. The last orbital filled is called the highest occupied molecular orbital (HOMO), while the molecular energy level above the HOMO is referred to as the lowest unoccupied molecular orbital (LUMO). As discussed in the next section, organic semiconductors can absorb photons with energies equal to its HOMO-LUMO energy difference thereby creating excitons.

1.3 Excitons in Organic Semiconductors

When an organic semiconductor absorbs a photon, an electron in the HOMO level is promoted to the LUMO level generating a hole (unfilled molecular orbital) in the HOMO level. Due to columbic attractions, the electron is strongly bound to the hole.[7] This electron-hole pair is defined as an exciton. In organic semiconductors excitons behave like a particle diffusing in a random walk fashion. In most organic semiconductors excitons diffuse 5 – 15 nm. In the next section we discuss the working principle of OPVs and the role of excitons.

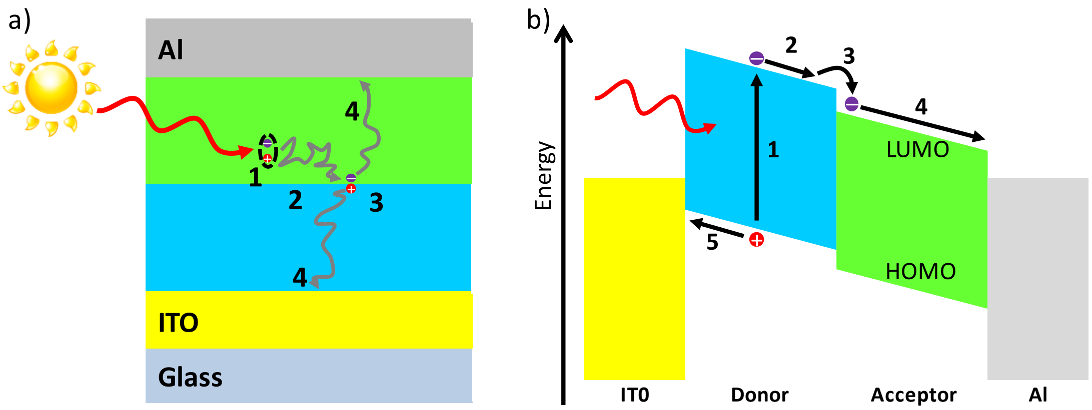

Figure 1.1. Working principle of bilayer film organic photovoltaics as depicted a) spatially and b) energetically. The four main processes shown are (1) charge generation, (2) exciton diffusion, (3) charge separation, and (4) charge extraction and collection.

1.4 Working Principle of Organic Photovoltaics

The simplest architecture for an OPV is a bilayer or planar structure (Figure 1.1a). In this configuration, the active layer is composed of electron donating and accepting materials. The active layer is sandwiched between a cathode such as Aluminium and a transparent and conductive anode such as Indium Tin Oxide (ITO). As shown in Figure 1.1, the performance of an OPV is determined by the efficiency of four main processes: (1) Efficiency of photon absorption and exciton generation (η_A). (2) Efficiency of exciton or electron-hole pair diffusion (η_D). (3) Efficiency of exciton charge transfer (η_{CT}) which creates free charges. (4) Efficiency of charge carrier collection (η_{CC}) yielding current. The product of these four efficiencies equals the external quantum efficiency (η_{EQE}). The donor and acceptor layer should have thicknesses roughly equivalent to double the exciton diffusion length in order to maximize the exciton diffusion efficiency and absorption. The four main processes can also be visualized in an energy diagram as shown in Figure 1.1b. Figure 1.1b shows that the LUMO offset between the donor and acceptor must be large enough to overcome the exciton binding energy which can be in the range 0.5 – 1 eV. The energy diagram also shows that an internal field is created under short circuit conditions. This filed provides a driving force for electrons to drift to the aluminium cathode and holes to drift to the ITO anode.

The exciton diffusion length in most organic semiconductors is roughly 5 – 15 nm. As a consequence, the donor and acceptor layers must be thin enough so that excitons are able to diffuse to the donor-acceptor interface whereby charge separation may occur. However, reducing the film thickness also results in a loss of photon absorption. In order to maximize both harvesting of excitons and photon absorption, the donor and acceptor materials can be blended together forming intimately mixed bulk heterojunction (BHJ) morphology as shown in Figure 1.2. Mixing the donor and acceptor materials reduces the distance in which excitons must travel to reach a donor-acceptor interface thereby enhancing the exciton harvesting efficiency. Using the BHJ device structure, small molecules OPVs have achieved efficiencies of 5 – 8%.[8–15] In both bilayer and BHJ films, the optimal performance is obtained by finely tuning the processing conditions in order to balance the efficiency of exciton generation, exciton harvesting, charge transport, and charge collection. Enhancing the exciton diffusion length in these materials it would relax the morphological requirements to obtain efficient exciton harvesting. As a result, the charge transport and collection efficiency could be further optimized to yield higher performing devices.

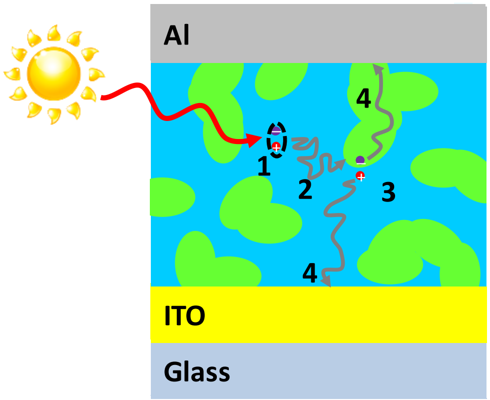

Figure 1.2. Depiction of an organic photovoltaic device with a bulk heterojunction device structure. The four main processes shown are (1) charge generation, (2) exciton diffusion, (3) charge separation, and (4) charge extraction and collection.

1.5 Energy Transfer Processes

Exciton diffusion may occur through cascade energy transfer, Dexter transfer, and Förster resonance energy transfer (FRET).[16–20] Cascade energy transfer occurs when a photon is emitted by one molecule and absorbed by another. This mechanism is more likely to occur in films which are thicker than 50 nm and have a significant overlap between its emission and absorption spectrum. Dexter transfer occurs through the direct exchange of electrons between an excited donor unit and a nearby acceptor unit. Since electrons are directly transferred in this mechanism, there must be sufficient overlap between the electron densities of the excite donor and ground state acceptor units with a length scale of 0.1 - 1 nm. For distances above 1 nm, excitons have a greater probability migrating through FRET. Förster transfer occurs when an excited donor unit transfers it energy to an acceptor unit through a non-radiative dipole-dipole coupling interaction. Efficient FRET requires (1) sufficient spectral overlap between the luminescent excited state donor unit and the nearby ground state acceptor unit, (2) a length scale less than 10 nm, and (3) adequate alignment of dipoles.

1.6 Relationship between FRET and Exciton Diffusion Length

Using Förster theory it is possible to calculate the distance at which a donor and acceptor chromophore has a transfer efficiency of 50%. This distance is referred to as the Förster radius R_0 and calculated from the spectral overlap using the following equation:

$$R_0{}^6 = \frac{9000(\ln 10)k^2 Q_Y}{128\pi^5 N_A n^4} \int_0^\infty F(\lambda)\varepsilon(\lambda)\lambda^4 d\lambda, \tag{1}$$

where k^2 is the relative orientation of dipoles (k^2 = 0.476 assuming rigid and randomly oriented dipoles), Q_y is the photoluminescence quantum yield (PLQY) in film, n is the average refractive index of the medium in the wavelength range at which spectral overlap is significant, $F(\lambda)$ is the corrected fluorescence intensity of the film with area normalized to unity and $\varepsilon(\lambda)$ is the molar extinction coefficient in film. The quantities can be determined experimentally using UV-Vis absorption, PL, and spectroscopic ellipsometry. Using the Förster radius, it is possible to determine that rate of energy transfer or hopping rate τ_{hop} if the hopping distance R is known using the following equation:

$$\tau_{hop} = \tau\left(\frac{R}{R_0}\right)^6, \tag{2}$$

where τ is the fluorescence lifetime in film and R is the distance between the donor and acceptor chromophores. The average distance between chromophores can be approximated by measuring the film density with X-ray reflectivity.

An excited donor is surrounded by acceptors in three dimensions in a bulk film. If we assume that each acceptor is equivalent and equal distance from the excited donor, there should not be any preferential direction of hopping. As a consequence, the hopping of excitons would mimic a random walk process. According to the Einstein-Smoluchowski theory of random walks, the diffusion coefficient D in a 3D system can be expressed as the following expression.[21]

$$D = \frac{R^2}{6\tau_{hop}}, \tag{3}$$

The diffusion length is defined as the root mean squared displacement of a particle from its initial position during time τ[22]:

$$L_D = \sqrt{\frac{\sum dL_i^2}{N}} = \sqrt{2ZD\tau}, \tag{4}$$

where dL_i is the displacement of a particle i from its original position and N is the total number of excitons. In the case of one-, two-, or three- dimensional diffusion, Z is equal to 1, 2, or 3, respectively.[22] However, in context of exciton diffusion a $\sqrt{2}$ factor is often omitted in Equation (1) and the values of L_D are often reported for the one-dimensional case:

$$L_D = \sqrt{D\tau}. \tag{5}$$

To be consistent with literature, we use Equation (2) to define the exciton diffusion length. In summary, the exciton diffusion length can be thought of as a series of energy transfer processes which behaves as a random walk processes. In the following section, we discuss how the migration of multiple excitons can be modeled with partial differential equations.

1.7 Modeling Exciton Density

In a working OPV, light enters the device and is absorbed by the organic semiconductor thereby creating an exciton density profile in the film. The profile of the exciton density is dependent on a number of factors such as the index of refraction and absorption coefficient of the materials. From the initial exciton density profile, excitons will diffuse from regions of high higher to lower concentrations until they relax within their lifetime or are quenched by an acceptor. The time evolution of the exciton density profile can be model using the partial differential equation:

$$\frac{\partial n(x,t)}{\partial t} = D\frac{\partial^2 n(x,t)}{\partial x^2} - \frac{n(x,t)}{\tau} + G(x,t), \tag{6}$$

where $n(x,t)$ is the exciton density at point x and time t, D is the exciton diffusion constant, τ is the exciton lifetime, and $G(x,t)$ is the exciton generation rate. The first term describes the exciton motion by diffusion, the second term represents exciton recombination, and the third term equates to the generation of excitons by light absorption. As discussed in the next section, Equation (6) is used in a number of techniques to measure exciton diffusion length in order to determine the fraction of excitons which able to diffuse to a quencher.

1.8 Measurement of Singlet Exciton Diffusion Length

As shown in Equation (5), the determination of the exciton diffusion length requires either the direct measurement of exciton diffusion length or the individual measurements of diffusion coefficient and exciton lifetime. For organic semiconductors with strong PL the exciton diffusion length can be determined by measuring the lifetime and modeling of the diffusion coefficient. If the lifetime cannot be determined due to weak PL or short exciton lifetime then the exciton diffusion length must be measured directly. In the following we provide a brief overview of common techniques to measure exciton diffusion length.

1.8.1 Steady-State Surface Quenching

In the Steady-State Surface Quenching (SS-SQ) technique,[23–29] PL in bilayer films with varying thickness of the organic semiconductor layer is measured with SS PL and modeled with a transfer matrix model and diffusion equation in order to fit for the exciton diffusion length that reproduces the measured quenching efficiencies. The main advantage with the SS-SQ technique is the direct measurement of the exciton diffusion length. Fabrication for the SS-SQ technique involves the preparation of bilayers films consisting of a quartz substrate, thin quenching layer, and an organic semiconductor layer of varying thickness. Since many organic semiconductors are sensitive to oxidation when illuminated in the presence of oxygen, PL measurements should be performed under nitrogen or prior to encapsulation. Measurements include SS PL to quantify the quenching efficiency, spectroscopic ellipsometry to determine the optical constants, atomic force microscopy to probe the surface roughness, and profilometry to determine film thicknesses. Analysis for the SS-SQ technique involves modeling optical constants which is used to simulate the initial exciton density profile upon excitation. Lastly, Equation (6) is applied to the initial exciton density profile in order to fit for the diffusion length which reproduces the quenching efficiency obtained from the PL measurements.

A drawback with the SS-SQ technique is the large number of films needed in order to explore a range of thicknesses. Additionally, there are a number of assumptions in the SS-SQ technique which create high demands in the fabrication and measurement process. Assumptions include a consistent morphology of the organic semiconductor at all thicknesses, efficient quenching, and a sharp interface between the organic semiconductor and quencher layer. A previous study showed that a "skin" layer is often present in spin coated organic films.[30] It may also be difficult to find a material which can form a sharp and strongly quenching layer with the organic semiconductor. Lastly, the SS-SQ technique assumes incidence and collection relative to the film requiring precise optical alignments during PL measurements. The SS-SQ technique is best for amorphous organic semiconductors that are able to form a sharp and strongly quenching interface with a quencher. Circumstances when the SS-SQ technique would be preferred over other techniques include the following: (1) bulk quenching techniques cannot be employed, (2) instrumentation to measure TR PL is not available and (3) a direct measurement of the exciton diffusion length is required.

1.8.2 Time-Resolved Surface Quenching

In the Time-Resolved Surface Quenching (TR-SQ) technique,[23,24,31–34] PL in bilayer films with varying thickness of the organic semiconductor layer are measured with TR PL and modeled with a transfer matrix model and diffusion equation in order to fit for the exciton diffusion length that reproduces the measured quenching efficiencies. Since the TR-SQ and SS-SQ techniques share the same fabrication and analysis procedure, both techniques are often performed simultaneously. The main advantage with the TR-SQ technique is the use of TR PL which is less sensitive to the orientation of the excitation beam and PL collection and SS PL. Unlike the SS-SQ technique, the TR-SQ can also yield the exciton diffusion coefficient by plugging in the measured exciton lifetime and exciton diffusion length into Equation (5). The TR-SQ may be difficult to employ accurately when the exciton lifetime is shorter than 500 ps and approaches the instrument response function which could be in the range of 20 − 100 ps. Conditions when the TR-SQ technique would be advantageous over other techniques include the following: (1) bulk quenching techniques cannot be employed and (2) direct measurement of the exciton diffusion length is required.

1.8.3 Exciton–Exciton Annihilation

In the Exciton–exciton annihilation (EEA) technique,[34–39] PL decays in pristine films at varying fluence levels are measured with TR PL and fitted with rate equations in order to fit for the annihilation radius and diffusion coefficient that reproduces the measured quenching efficiencies. The main advantage of the EEA technique is that it does not require a quencher material simplifying the fabrication and analysis. Fabrication for the

EEA technique only requires a pristine film of the organic semiconductor which can be deposited via spin coating or thermal evaporation followed by encapsulation. Measurements for the EEA technique include UV absorption, SS PL, TR PL at varying laser intensities, spectroscopic ellipsometry for determination of optical constants, x-ray reflectivity to determine film density, and profilometry for determination of thickness. The measured exciton lifetimes are subsequently plugged into a rate equation in order to fit for the annihilation rate which enables determination of the diffusion coefficient. The EEA technique assumes a homogenous distribution of molecules and high photostability. The EEA technique may be challenging to employ accurately since most organic semiconductors are easily oxidized and are sensitive to processing conditions which impact intermolecular spacing. As a result of these challenges, the EEA technique is best suited for organic semiconductors with high photostability and a long exciton lifetime. Situations when the EEA technique would be ideal relative to over other techniques include the following: (1) the organic semiconductor is in low quantity or expensive, (2) a suitable quencher is not available, (3) the study requires minimal influence from the presence of a quencher, or (4) advance modeling software is not available.

1.8.4 Bulk Quenching with Monte Carlo Modeling

In the Bulk Quenching with Monte Carlo Modeling (BQ-MC) technique,[39–42] PL decays in blend films with varying concentrations of a quencher are measured with TR PL and modeled with a Monte Carlo simulation to fit for the diffusion coefficient that reproduces the measured quenching efficiencies. The advantage of the BQ-MC technique is the simple fabrication method and minimum number of measurements and assumptions.

Fabrication for the BQ-MC technique involves spin coating of blend solutions of the organic semiconductor with varying quencher concentrations. Measurements include TR PL to determine the exciton lifetime and profilometry to ensure film thickness of roughly 100 nm. The measured exciton lifetimes are fed in to a Monte Carlo simulation which determines the diffusion coefficient necessary in order to reproduce the experimentally measured quenching efficiency. The BQ-MC technique assumes no quenching at interfaces, efficient quenching of excitons by quencher, and homogeneous distribution of the organic semiconductor and acceptor molecules. The BQ-MC technique is ideal for amorphous and soluble organic semiconductors that can homogenously mix with a strong quencher molecule. In most situations the BQ-MC technique is the preferred choice. Scenarios where the BQ-MC technique cannot be used include (1) the organic semiconductor is highly crystalline thereby preventing a homogenous distribution with quencher, (2) the organic semiconductor has poor solubility, or (3) advance modeling software is not available.

1.8.5 Bulk Quenching with Stern–Volmer Equation

In the Bulk quenching with Stern–Volmer modeling (BQ-SV) technique,[39] PL decays in blend films with varying concentrations of a quencher are measured with TR PL and fitted with the Stern–Volmer Equation in order to determine the diffusion coefficient that reproduces the measured quenching efficiencies. Since the BQ-MC and BQ-SV modeling technique share the same fabrication and measurement process both techniques can be performed together. The main advantage of the BQ-SV technique is that it does not require an advance modeling software. Additionally, the BQ-SV technique can be used to extract the exciton trap density as discussed in Chapter 4. The BQ-SV technique assumes mono-exponential photoluminescence decay, no quenching at interfaces, efficient quenching of excitons by quencher, and homogeneous distribution of excitons at donor and acceptor molecules. However, the BQ-SV technique maybe be performed alone if the Monte Carlo software is unavailable, the lifetime is not mono-exponential, or the measurement of exciton trap density is necessary.

1.8.6 FRET Theory

In the FRET theory method,[21,39,43,44] absorption and PL measurements are used to calculate the exciton diffusion coefficient using Förster theory and the Einstein-Smoluchowski theory of random walks. The advantage with the FRET theory method is the straightforward fabrication, measurement, and analysis. The fabrication for the FRET theory technique requires only a film of the pure organic semiconductor which can be prepared via spin coating thereby reducing the amount of material needed. Measurements include UV-visible absorption, SS PL, TR PL, PL quantum yield, and spectroscopic ellipsometry. These measurements are used to calculate the Förster radius and energy transfer rate with Förster theory. The diffusion coefficient can then be determined using the Einstein-Smoluchowski theory of random walks. In practice, the FRET theory technique is difficult to apply accurately since the intermolecular spacing is sensitive to processing conditions and difficult to measure experimentally. For this reason, determination of the exciton diffusion length using FRET theory alone is not recommended. The FRET theory method can help elucidate the observed trends in exciton diffusion lengths when performed in tandem with other techniques.

1.8.7 Microwave Conductivity

In the Microwave Conductivity (MC) technique,[45–47] surface conductivity is measured in bilayers films with TR microwave conductivity and modeled with a diffusion equation in order to fit for the exciton diffusion length that reproduces the measured surface photoconductivity. The MC method is useful for organic semiconductors which are weakly photoluminescent. Fabrication for this method involves the preparation of polycrystalline anatase TiO_2 onto quartz via sol-gel or electron beam evaporation followed by ambient annealing for 24 hours at 450 ^{0}C. Subsequently, the organic semiconductor layer is deposited at varying thicknesses by maintaining the spin speed constants and varying the solution concentration. Measurements include UV-Vis absorption to determine the absorption coefficient and TR microwave conductivity (TRMC) to measure the enhancement in surface photoconductivity in the organic semiconductor and TiO2 bilayers. For analysis, a diffusion model is applied to the exciton density profile in order to fit for the required interfacial electron injection efficiency and exciton diffusion length which reproduces measured enhancement in surface photoconductivity. This technique may be challenging to employ if the TiO2 layer is unable to form a sharp interface which efficiently quenches excitons generated in the organic semiconductor. The MC method is a viable option when bulk quenching methods are not possible or the organic semiconductor is weakly photoluminescent.

1.8.8 Photocurrent Measurements

In the Photocurrent Measurements technique,[23,24,48–59] bilayer device performance is measured in order to determine the fraction of excitons which reach the quencher/organic semiconductor interface which is fed into a transfer matrix and diffusion model in order to fit for exciton diffusion length that reproduces the generated current of the device. The main advantage with the Photocurrents measurements technique is the ability to probe the exciton diffusion length in organic semiconductors with weak PL. The fabrication with this method includes the preparation of a bilayer solar cell composed of aluminium, ITO, quencher layer, and organic semiconductor of varying thicknesses. Measurements include device performance under a solar simulator, spectroscopic ellipsometry to determine optical constants, and profilometry for thickness. For analysis, the experimentally measured thicknesses and optical constants are inputted into a transfer matrix model where Maxwell Equations are used to model the optical electrical field and exciton density profile. A diffusion model is then applied to the exciton density profile in order to fit for the required exciton diffusion length that reproduces the experimentally measured photocurrent. Assumptions in the Photocurrents Measurements technique include the formation of a sharp and efficient exciton quenching interface, 100% charge extraction, and negligible quenching at the electrode/organic semiconductor interface. The large number of measurements and assumptions make the Photocurrent Measurements technique difficult to execute accurately. The Photocurrent Measurements techniques are therefore ideal for organic materials which have shown high charge mobilities and good bilayer device performance. The Photocurrent Measurements technique is preferred when (1) other bulk and quenching techniques are not possible, (2) the organic semiconductor is weakly photoluminescent, or (3) a direct measurement of the exciton diffusion length is required.

1.9 Chapter Summaries

As mentioned in Section 1.4, enhancements in the exciton diffusion length would relax the processing conditions necessary to obtain efficient exciton harvesting. This would then allow for further optimization of the charge generation, transport, and extraction which would lead to increases in device efficiencies. This requires a better understanding of how chemical structure and processing conditions affect the exciton diffusion length. Exciton diffusion lengths have been measured in a number of small molecules and polymers.[21,26,28,29,31,32,34–36,38–41,47,51,53,54,57,60–74] It is difficult to make comparison between works since the techniques used to measure exciton diffusion length differ. There is a need for a body of work which compares techniques used to measure exciton diffusion length. In addition, further investigation is needed to probe the dependence of exciton diffusion length on chemical structure and processing conditions.

The first aim of this thesis is to investigate the relationship between chemical structure and device performance. In **Chapter 2** a class of diketopyrrolopyrrole (DPP) small molecules is used study how solubilizing groups and conjugation length impact the morphology, crystallinity, PL, mobility, and ultimately the device performance. Our studies demonstrate that a material's potential device performance can be limited by slight chemical modifications which prevent device optimization at high donor:acceptor blend ratios and elevated annealing temperatures where charge mobility is balanced and charge collection is enhanced in the donor and acceptor phase.

The second aim of this thesis compares techniques to measure exciton diffusion length and probe the impact of chemical structure on exciton diffusion length. In **Chapter 3** the fabrication, measurement, and analysis procedure for several bilayer and bulk PL quenching techniques is compared and contrasted using compounds studied in Chapter 2. We also study how molecular bulkiness and conjugation length impact the exciton diffusion length. It is shown that decreasing the conjugation length in a small molecule results in an enhancement in the exciton diffusion coefficient and diffusion length. We attribute this to an increase in relative molecular ordering upon decreasing the conjugation length. It is also shown that decreasing the molecular bulkiness by replacement of the ethyl-hexyl groups by the linear alkyl chains has little effect on the resulting exciton diffusion parameters.

The third aim of this thesis is to investigate the mechanism of exciton diffusion length. In **Chapter 4** we compare the exciton diffusion length in thin films processed with and without a high boiling point additive. We find that the exciton diffusion length is significantly reduced in thin films that were processed with a high boiling point additive or annealed, as compared to the as-cast films. Stern-Volmer analysis reveals that additive processing leads to an enhancement in excitonic trap states. The decrease in exciton diffusion length upon processing with the additive is directly related to the diffusion-assisted quenching at these trap states. Additionally, temperature dependent measurements shows that exciton diffusion is dominated by temperature activated hopping, while the contribution of downhill migration to the overall exciton diffusion length is significantly less in our small molecule system than what has been previously observed in a polymer system.[33]

The fourth aim of this thesis compares the exciton diffusion length and power conversion efficiency. In **Chapter 5** the exciton diffusion length is measured for several small molecules which have been used to fabricate solution processed organic photovoltaics with high power conversion efficacies. We find that the two materials with the lowest diffusion length also exhibit the highest exciton trap density. Despite large variances in exciton diffusion length these small molecules yield similar device performance in optimized solar cells.

In **Chapter 6,** we briefly summarize the guiding research questions of this dissertation, approaches taken to answer these questions, and the outcomes of this work. Additionally, possible directions for future work are provided.

1.10 Reference

(1) Dou, L.; You, J.; Yang, J.; Chen, C.-C.; He, Y.; Murase, S.; Moriarty, T.; Emery, K.; Li, G.; Yang, Y. *Nat. Photonics* **2012**, *6*, 180–185.

(2) Krebs, F. C.; Alstrup, J.; Spanggaard, H.; Larsen, K.; Kold, E. *Sol. Energy Mater. Sol. Cells* **2004**, *83*, 293–300.

(3) Schilinsky, P.; Waldauf, C.; Brabec, C. J. *Adv. Funct. Mater.* **2006**, *16*, 1669–1672.

(4) Hoth, C. N.; Schilinsky, P.; Choulis, S. A.; Brabec, C. J. *Nano Lett.* **2008**, *8*, 2806–2813.

(5) Girotto, C.; Rand, B. P.; Genoe, J.; Heremans, P. *Sol. Energy Mater. Sol. Cells* **2009**, *93*, 454–458.

(6) Fleming, I. *Molecular Orbitals and Organic Chemical Reactions*; Student Edition edition.; Wiley: Chichester, West Sussex, U.K, 2009.

(7) Sun; Sam-Shajing. *Organic Photovoltaics: Mechanisms, Materials, and Devices*; Sun, S.-S.; Sariciftci, N. S., Eds.; 1 edition.; CRC Press, 2012.

(8) Welch, G. C.; Perez, L. A.; Hoven, C. V.; Zhang, Y.; Dang, X.-D.; Sharenko, A.; Toney, M. F.; Kramer, E. J.; Nguyen, T.-Q.; Bazan, G. C. *J. Mater. Chem.* **2011**, *21*, 12700–12709.

(9) Liu, X.; Sun, Y.; Perez, L. A.; Wen, W.; Toney, M. F.; Heeger, A. J.; Bazan, G. C. *J. Am. Chem. Soc.* **2012**, *134*, 20609–20612.

(10) Sun, Y.; Welch, G. C.; Leong, W. L.; Takacs, C. J.; Bazan, G. C.; Heeger, A. J. *Nat. Mater.* **2012**, *11*, 44–48.

(11) Van der Poll, T. S.; Love, J. A.; Nguyen, T.-Q.; Bazan, G. C. *Adv. Mater.* **2012**, *24*, 3646–3649.

(12) Zhou, J.; Wan, X.; Liu, Y.; Zuo, Y.; Li, Z.; He, G.; Long, G.; Ni, W.; Li, C.; Su, X.; Chen, Y. *J. Am. Chem. Soc.* **2012**, *134*, 16345–16351.

(13) Shen, S.; Jiang, P.; He, C.; Zhang, J.; Shen, P.; Zhang, Y.; Yi, Y.; Zhang, Z.; Li, Z.; Li, Y. *Chem. Mater.* **2013**, *25*, 2274–2281.
(14) Zhou, J.; Zuo, Y.; Wan, X.; Long, G.; Zhang, Q.; Ni, W.; Liu, Y.; Li, Z.; He, G.; Li, C.; Kan, B.; Li, M.; Chen, Y. *J. Am. Chem. Soc.* **2013**, *135*, 8484–8487.
(15) Roncali, J.; Leriche, P.; Blanchard, P. *Adv. Mater.* **2014**, *26*, 3821–3838.
(16) Berggren, M.; Dodabalapur, A.; Slusher, R. E.; Bao, Z. *Nature* **1997**, *389*, 466–469.
(17) Flamini, R.; Marrocchi, A.; Spalletti, A. *Photochem. Photobiol. Sci.* **2014**, *13*, 1031–1038.
(18) Dexter, D. L. *J. Chem. Phys.* **1953**, *21*, 836–850.
(19) Dexter, D. L.; Knox, R. S.; Förster, T. *Phys. Status Solidi B* **1969**, *34*, K159–K162.
(20) Scholes, G. D. *Annu. Rev. Phys. Chem.* **2003**, *54*, 57–87.
(21) Lunt, R. R.; Giebink, N. C.; Belak, A. A.; Benziger, J. B.; Forrest, S. R. *J. Appl. Phys.* **2009**, *105*, 053711.
(22) Pope, M.; Swenberg, C. E. *Electronic processes in organic crystals and polymers*; Oxford University Press, 1999.
(23) Theander, M.; Yartsev, A.; Zigmantas, D.; Sundström, V.; Mammo, W.; Andersson, M. R.; Inganäs, O. *Phys. Rev. B* **2000**, *61*, 12957.
(24) Peumans, P.; Yakimov, A.; Forrest, S. R. *J. Appl. Phys.* **2003**, *93*, 3693.
(25) Wu, Y.; Zhou, Y. C.; Wu, H. R.; Zhan, Y. Q.; Zhou, J.; Zhang, S. T.; Zhao, J. M.; Wang, Z. J.; Ding, X. M.; Hou, X. Y. *Appl. Phys. Lett.* **2005**, *87*, 044104–044104 – 3.
(26) Scully, S. R.; McGehee, M. D. *J. Appl. Phys.* **2006**, *100*, 034907.
(27) Zhou, Y. C.; Wu, Y.; Ma, L. L.; Zhou, J.; Ding, X. M.; Hou, X. Y. *J. Appl. Phys.* **2006**, *100*, 023712–023712 – 5.
(28) Goh, C.; Scully, S. R.; McGehee, M. D. *J. Appl. Phys.* **2007**, *101*, 114503.
(29) Rim, S.-B.; Fink, R. F.; Schöneboom, J. C.; Erk, P.; Peumans, P. *Appl. Phys. Lett.* **2007**, *91*, 173504–173504 – 3.
(30) Mikhnenko, O. V.; Cordella, F.; Sieval, A. B.; Hummelen, J. C.; Blom, P. W. M.; Loi, M. A. *J. Phys. Chem. B* **2009**, *113*, 9104–9109.
(31) Markov, D. E.; Tanase, C.; Blom, P. W. M.; Wildeman, J. *Phys. Rev. B* **2005**, *72*, 045217.
(32) Markov, D. E.; Amsterdam, E.; Blom, P. W. M.; Sieval, A. B.; Hummelen, J. C. *J. Phys. Chem. A* **2005**, *109*, 5266–5274.
(33) Mikhnenko, O. V.; Cordella, F.; Sieval, A. B.; Hummelen, J. C.; Blom, P. W. M.; Loi, M. A. *J. Phys. Chem. B* **2008**, *112*, 11601–11604.
(34) Shaw, P. E.; Ruseckas, A.; Samuel, I. D. W. *Adv. Mater.* **2008**, *20*, 3516–3520.
(35) Lewis, A. J.; Ruseckas, A.; Gaudin, O. P. M.; Webster, G. R.; Burn, P. L.; Samuel, I. D. W. *Org. Electron.* **2006**, *7*, 452–456.
(36) Cook, S.; Furube, A.; Katoh, R.; Han, L. *Chem. Phys. Lett.* **2009**, *478*, 33–36.
(37) Shaw, P. E.; Ruseckas, A.; Peet, J.; Bazan, G. C.; Samuel, I. D. W. *Adv. Funct. Mater.* **2010**, *20*, 155–161.
(38) Masri, Z.; Ruseckas, A.; Emelianova, E. V.; Wang, L.; Bansal, A. K.; Matheson, A.; Lemke, H. T.; Nielsen, M. M.; Nguyen, H.; Coulembier, O.; Dubois, P.; Beljonne, D.; Samuel, I. D. W. *Adv. Energy Mater.* **2013**, *3*, 1445–1453.

(39) Lin, J. D. A.; Mikhnenko, O. V.; Chen, J.; Masri, Z.; Ruseckas, A.; Mikhailovsky, A.; Raab, R. P.; Liu, J.; Blom, P. W. M.; Loi, M. A.; García-Cervera, C. J.; Samuel, I. D. W.; Nguyen, T.-Q. *Mater. Horiz.* **2014**, *1*, 280–285.

(40) Mikhnenko, O. V.; Azimi, H.; Scharber, M.; Morana, M.; Blom, P. W. M.; Loi, M. A. *Energy Environ. Sci.* **2012**, *5*, 6960–6965.

(41) Mikhnenko, O. V.; Lin, J.; Shu, Y.; Anthony, J. E.; Blom, P. W. M.; Nguyen, T.-Q.; Loi, M. A. *Phys. Chem. Chem. Phys.* **2012**, *14*, 14196–14201.

(42) Raisys, S.; Kazlauskas, K.; Daskeviciene, M.; Malinauskas, T.; Getautis, V.; Jursenas, S. *J. Mater. Chem. C* **2014**, *2*, 4792–4798.

(43) Lunt, R. R.; Benziger, J. B.; Forrest, S. R. *Adv. Mater.* **2010**, *22*, 1233–1236.

(44) Luhman, W. A.; Holmes, R. J. *Adv. Funct. Mater.* **2011**, *21*, 764–771.

(45) Kroeze, J. E.; Savenije, T. J.; Vermeulen, M. J. W.; Warman, J. M. *J. Phys. Chem. B* **2003**, *107*, 7696–7705.

(46) Savenije, T. J.; Siebbeles, L. D. In *Laser Science*; OSA Technical Digest (CD); Optical Society of America, 2010; p. LWC5.

(47) Fravventura, M. C.; Hwang, J.; Suijkerbuijk, J. W. A.; Erk, P.; Siebbeles, L. D. A.; Savenije, T. J. *J. Phys. Chem. Lett.* **2012**, *3*, 2367–2373.

(48) Ghosh, A. K.; Feng, T. *J. Appl. Phys.* **1978**, *49*, 5982–5989.

(49) Wagner, J.; Fritz, T.; Böttcher, H. *Phys. Status Solidi A* **1993**, *136*, 423–432.

(50) Bulović, V.; Forrest, S. R. *Chem. Phys. Lett.* **1995**, *238*, 88–92.

(51) Halls, J. J. M.; Pichler, K.; Friend, R. H.; Moratti, S. C.; Holmes, A. B. *Appl. Phys. Lett.* **1996**, *68*, 3120–3122.

(52) Pettersson, L. A. A.; Roman, L. S.; Inganäs, O. *J. Appl. Phys.* **1999**, *86*, 487.

(53) Stübinger, T.; Brütting, W. *J. Appl. Phys.* **2001**, *90*, 3632–3641.

(54) Yang, C. L.; Tang, Z. K.; Ge, W. K.; Wang, J. N.; Zhang, Z. L.; Jian, X. Y. *Appl. Phys. Lett.* **2003**, *83*, 1737–1739.

(55) Huijser, A.; Savenije, T. J.; Shalav, A.; Siebbeles, L. D. A. *J. Appl. Phys.* **2008**, *104*, 034505–034505 – 10.

(56) Rim, S.-B.; Peumans, P. *J. Appl. Phys.* **2008**, *103*, 124515–124515 – 5.

(57) Qin, D.; Gu, P.; Dhar, R. S.; Razavipour, S. G.; Ban, D. *Phys. Status Solidi A* **2011**, *208*, 1967–1971.

(58) Leow, C.; Ohnishi, T.; Matsumura, M. *J. Phys. Chem. C* **2014**, *118*, 71–76.

(59) Guide, M.; Lin, J. D. A.; Proctor, C. M.; Chen, J.; García-Cervera, C.; Nguyen, T.-Q. *J. Mater. Chem. A* **2014**, *2*, 7890–7896.

(60) Vaubel, G.; Baessler, H. *Mol. Cryst. Liq. Cryst.* **1970**, *12*, 47–56.

(61) Gregg, B. A.; Sprague, J.; Peterson, M. W. *J. Phys. Chem. B* **1997**, *101*, 5362–5369.

(62) Haugeneder, A.; Neges, M.; Kallinger, C.; Spirkl, W.; Lemmer, U.; Feldmann, J.; Scherf, U.; Harth, E.; Gügel, A.; Müllen, K. *Phys. Rev. B* **1999**, *59*, 15346–15351.

(63) Kawamura, Y.; Sasabe, H.; Adachi, C. *Jpn. J. Appl. Phys.* **2004**, *43*, 7729–7730.

(64) Markov, D. E.; Hummelen, J. C.; Blom, P. W. M.; Sieval, A. B. *Phys. Rev. B* **2005**, *72*, 045216.

(65) Bansal, A. K.; Holzer, W.; Penzkofer, A.; Tsuboi, T. *Chem. Phys.* **2006**, *330*, 118–129.

(66) Terao, Y.; Sasabe, H.; Adachi, C. *Appl. Phys. Lett.* **2007**, *90*, 103515–103515 – 3.

(67) Holzhey, A.; Uhrich, C.; Brier, E.; Reinhold, E.; Bäuerle, P.; Leo, K.; Hoffmann, M. *J. Appl. Phys.* **2008**, *104*, 064510–064510 – 8.

(68) Gommans, H.; Schols, S.; Kadashchuk, A.; Heremans, P.; Meskers, S. C. J. *J. Phys. Chem. C* **2009**, *113*, 2974–2979.

(69) Mikhnenko, O. V.; Ruiter, R.; Blom, P. W. M.; Loi, M. A. *Phys. Rev. Lett.* **2012**, *108*, 137401.

(70) Ward, A. J.; Ruseckas, A.; Samuel, I. D. W. *J. Phys. Chem. C* **2012**, *116*, 23931–23937.

(71) Menke, S. M.; Luhman, W. A.; Holmes, R. J. *Nat. Mater.* **2013**, *12*, 152–157.

(72) Bailey, J.; Wright, E. N.; Wang, X.; Walker, A. B.; Bradley, D. D. C.; Kim, J.-S. *J. Appl. Phys.* **2014**, *115*, 204508.

(73) Li, Z.; Zhang, X.; Woellner, C. F.; Lu, G. *Appl. Phys. Lett.* **2014**, *104*, 143303.

(74) Menelaou, C.; Tierney, S.; Blouin, N.; Mitchell, W.; Tiwana, P.; McKerracher, I.; Jagadish, C.; Carrasco, M.; Herz, L. M. *J. Phys. Chem. C* **2014**, *118*, 17351–17361.

Chapter 2. Effect of structural variation on photovoltaic characteristics of phenyl substituted diketopyrrolopyrroles

2.1 Introduction

Organic solar cells have attracted a great deal of interest due to their low cost, solution processibility, light weight, flexibility,[1–4] and recent published efficiencies up to 10%.[5–12] The majority of bulk heterojunction (BHJ) solar cells utilize conjugated polymers as the electron donor. However, conjugated polymers often suffer from batch to batch variation in molecular weights[13] and end group contamination,[14] which has been shown to adversely influence solar cell performance.[13,14] For these reasons, organic solar cells based on solution-processed small molecules have gained attention since small molecules can be synthetically reproducible.[15–28]

Studies on diketopyrrolopyrrole (DPP)-based small molecules have shown that slight modifications in the solubilizing group and thiophene conjugation length can significantly impact the optical properties, morphology, and charge carrier mobility.[29,30] Nanoscale ordering and interchromophore contacts could be enhanced for DPP small molecules by replacing branched alkyl chains with straight chains and by decreasing the length of the alkyl chains.[29] Field effect transistors (FETs) fabricated from DPP derivatives showed that decreasing the alkyl chain length from twelve to six carbons promoted molecular ordering while increasing FET hole mobility.[30] Efficient solar cells have be fabricated from DPP-containing polymers[31–40] and small molecules.[29,30,41–57] A DPP derivative incorporating benzofuran units exhibited long range order, near-infrared absorption, and solar cell efficiencies up to 4.8%[16] or up to 5.5%[41] using three DPP units when optimized with [6,6]-Phenyl C71-butyric acid methyl ester ($PC_{71}BM$).

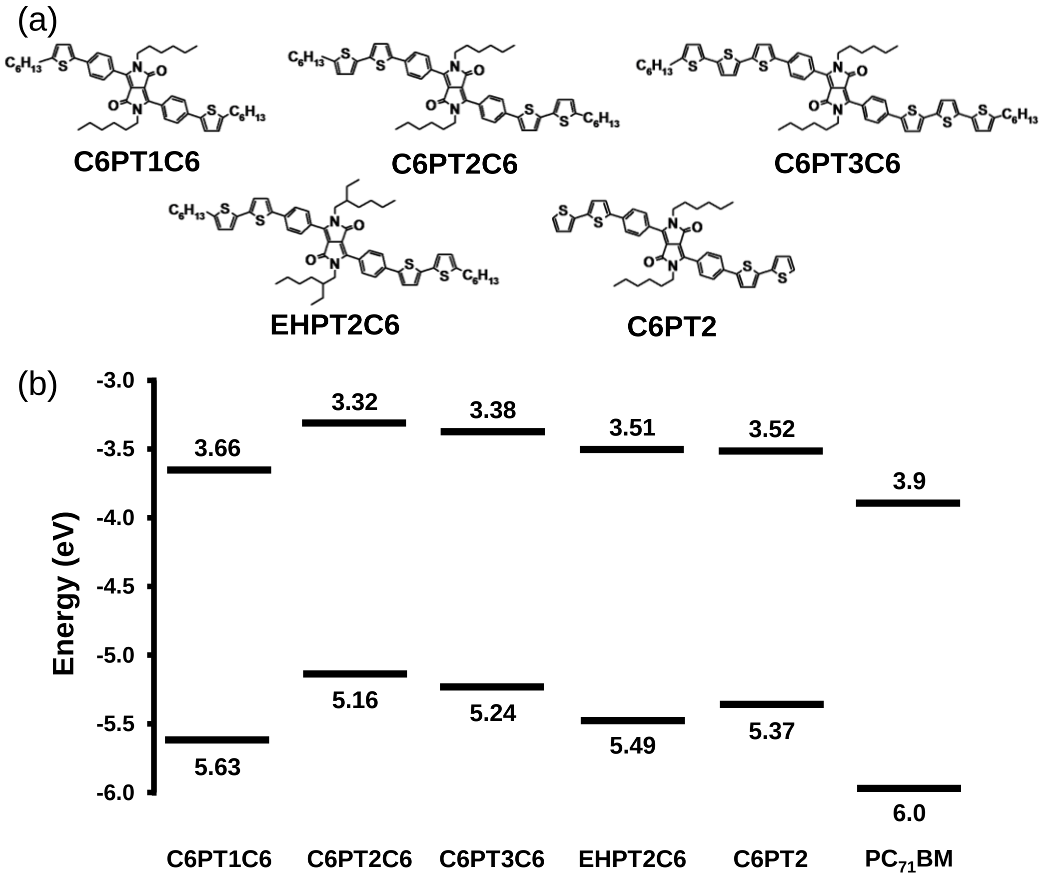

Figure 2.1. (a) Chemical structures for C6PT1C6, C6PT2C6, C6PT3C6, EHPT2C6, and C6PT2. (b) HOMO-LUMO levels of donor and acceptor materials.

In order to make further advancements in the design of DPP-containing donors, it is necessary to understand the relationship between chemical structure and device performance. Small molecules based on DPP units serve as a good model system to study structure-function relationships due to the ability to tune the physical and optoelectronic properties by incorporating different alkyl and aryl groups. In a previous work,[58] our group designed a series of compounds (Figure 2.1a) to study influence of structural variation on the solid-state properties of DPP-based oligophenylenethiophenes. It was shown that slight systematic changes in chemical structures can result in significant changes in material properties such as the crystallinity, morphology, optical bandgap, and mobility. In this work, we build upon our previous study by utilizing the same class of compounds to investigate how systematic chemical modifications impact solar cell device performance. It is shown that slight chemical modification to functional groups and conjugation length can limit device performance due to undesirable phase segregation, charge carrier mobility imbalance, and large domains which limit exciton harvesting.

2.2 Nomenclature

With regards to chemical structure naming for compounds in Figure 2.1, the first two letters are either “C6” or “EH” to represent a six-carbon linear alkyl chain or a branched ethyl-hexyl group respectively which is attached to the lactam nitrogen. The third letter, “P”, represents the presence of a phenyl group adjacent to the DPP core. The fourth and fifth letter can be “T1”, “T2” or “T3” to represent one, two or three thiophenes adjacent to the phenyl units. Lastly, “C6” is added at the end of the chemical name if a six carbon alkyl chain is present on the terminal thiophene units.

2.3 Device Performance

Solar cells devices of the compounds in Figure 2.1a were tested at donor:$PC_{71}BM$ blend ratios ranging from 10:90 to 80:20 for as cast along with 80, 100, and 120 ^{0}C annealed devices as shown in Figure 2.2. The optimized conditions are summarized in Figure 2.3

and Table 1. Figure 2.3 shows that C6PT2C6 yielded the greatest solar cell performance with is attributed to the enhanced current generation as shown from the EQE (Figure 2.3b). Modifications to the conjugation length or solubilizing groups result in a decrease in solar cell device performance. These trends are further discussed in the following sections.

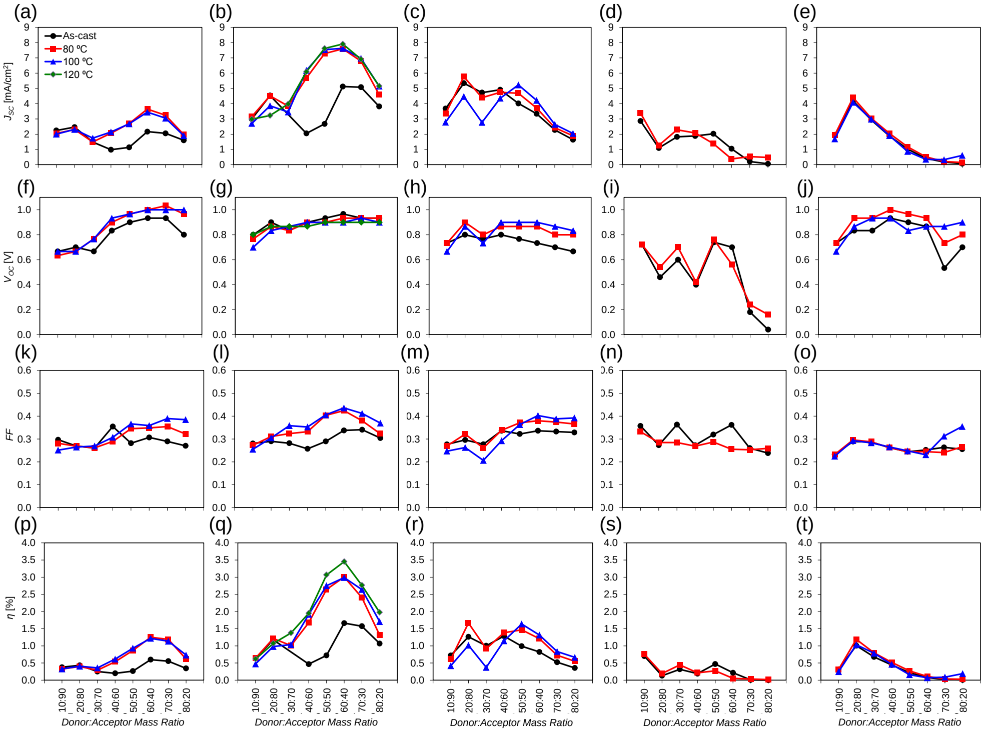

Figure 2.2. Solar cell parameters J_{SC} (a-e), V_{OC} (f-j), FF (k-o), and η% (p-t) are plotted as a function of donor:PC$_{71}$BM mass ratio. DPP donors C6PT1C6 (1st column), C6PT2C6 (2nd column), C6PT3C6 (3rd column), EHPT2C6 (4th column), and C6PT2 (5th column) are shown for as-cast (black circles) films and 10 minute annealed films at 80 ºC (red boxes), 100 ºC (blue triangles), and 120 ºC (green diamonds).

The blend films of C6PT1C6:PC$_{71}$BM, C6PT2C6:PC$_{71}$BM, C6PT3C6:PC$_{71}$BM, EHPT2C6:PC$_{71}$BM, and C6PT2:PC$_{71}$BM optimize at mass ratios of 60:40, 60:40, 20:80, 10:90, and 20:80 which corresponds to donor:acceptor mole ratios of 66:36, 62:38, 19:81, 20:80, and 25:75 respectively. Both C6PT1C6:PC$_{71}$BM and C6PT2C6:PC$_{71}$BM blends optimize at greater donor fractions while C6PT3C6:PC$_{71}$BM, EHPT2C6:PC$_{71}$BM, and C6PT2:PC$_{71}$BM optimize at higher PC$_{71}$BM fractions. We find that the blend ratio significantly impacts the solar cell device performance.

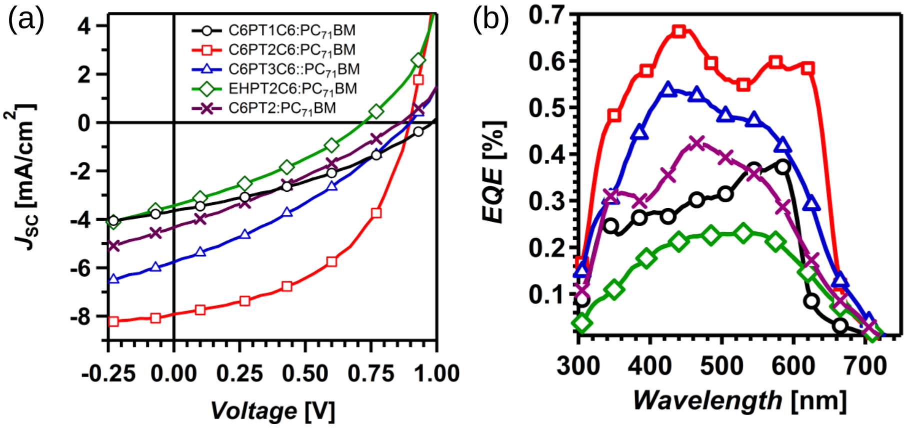

Figure 2.3. (a) J-V characteristics and (b) external quantum efficiency of optimized DPP donors with PC$_{71}$BM.

2.4 Impact of Replacement of Linear Alkyl Chains with Ethyl-Hexyl Groups

To investigate the impact of molecular bulkiness, the linear alkyl chains on the lactam nitrogen units of compound C6PT2C6 is substituted with ethyl-hexyl groups to form compound EHPT2C6. Figure 2.3a and Table 1 shows that the C6PT2C6:PC$_{71}$BM device optimizes at a 60:40 blend ratio and an annealing temperature of 120 °C with an open circuit voltage (V_{OC}) of 0.90 V, short circuit current (J_{SC}) of 7.91 mA/cm^2, fill factor (FF) of 0.49, and power conversion efficiency (PCE) of 3.45 % (Table 1). In comparison, the EHPT2C6:PC$_{71}$BM device optimizes at a 20:80 blend ratio and an annealing temperature of 80 °C which yields a V_{OC} of 0.72 V, J_{SC} of 3.37 mA/cm^2, FF of 0.33, and PCE of 0.76 % (Table 1).

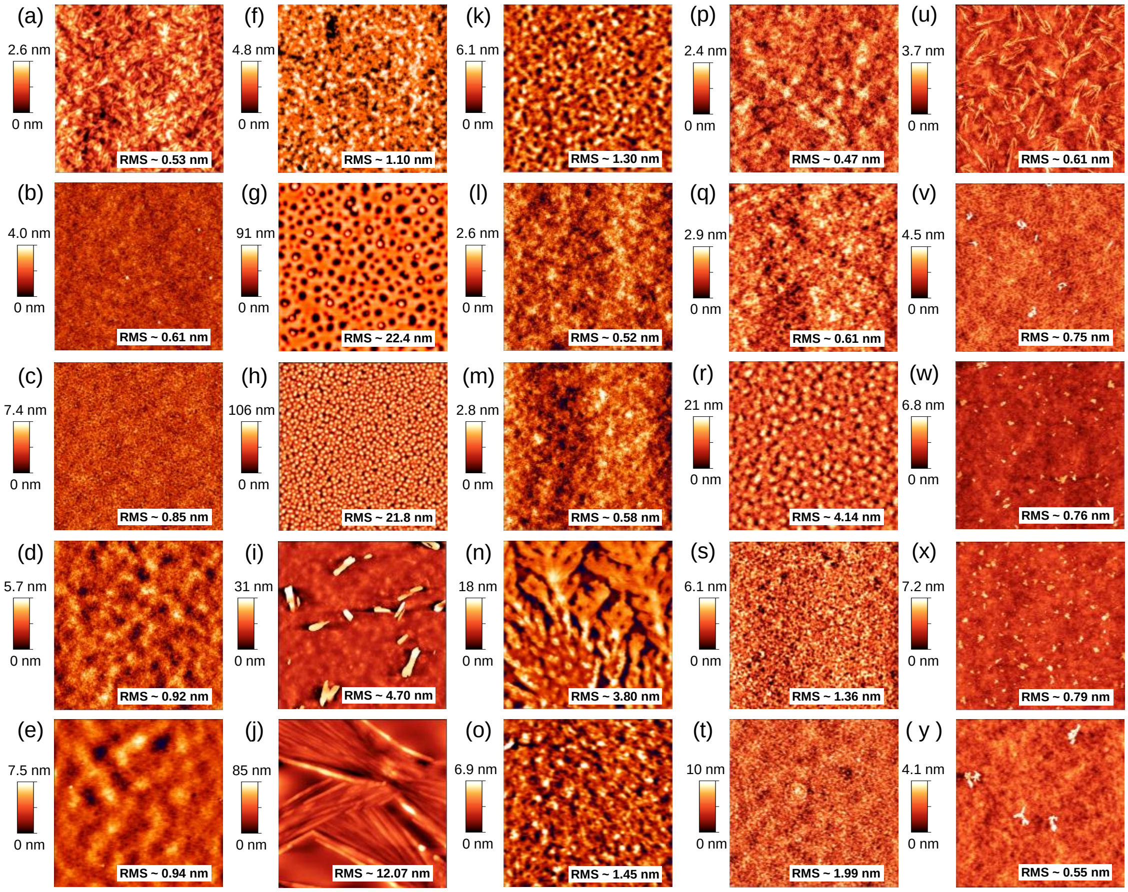

Figure 2.4. Topography images for 80 ^{0}C annealed blend films of C6PT2C6 (a-e), EHPT2C6 (f-j), C6PT2 (k-o), C6PT1C6 (p-t) and C6PT3C6 (u-y) with $PC_{71}BM$ for donor:acceptor blend ratios 10:90 (a, f, k, p, u), 20:80 (b, g, i, q, v), 40:60 (c, h, m, r, w), 60:40 (d, i, n, s, x), and 70:30 (e, j, o, t, y). All image scan sizes are 10 µm × 10 µm.

Figure 2.4 shows the 80 ^{0}C annealed blend film morphologies of compounds in this work at donor:$PC_{71}BM$ blend ratios spanning 10:90 to 80:20. Blend films of C6PT2C6:$PC_{71}BM$ yield featureless topographies and a low root-mean-squared (RMS) roughness around 1 nm (Figure 2.4a-e). This suggests that compounds C6PT2C6 and $PC_{71}BM$ have good miscibility together. In contrast, blend films of EHPT2C6:$PC_{71}BM$ show micron scale aggregates across blend ratios 20:80 to 80:20 (Figure 2.4g-j). An exception is the 10:90 blend ratio which does not yield micron scale aggregates (Figure

2.4f). The efficiency vs. blend ratio plot for EHPT2C6:$PC_{71}BM$ blends (Figure 2.2s) shows that the device performance is lowest for blend ratios which exhibited rough films but is greatest for the 10:90 blend ratio where the film RMS roughness is around 1 nm. In this work we found that films with large scale phase segregation caused shorted devices which explain the poor performance. This result shows that micron scale phase segregation at high donor:acceptor ratios can induce devices optimization at a low donor:acceptor ratio.

Figure 2.4 showed that 20:40 and 40:60 EHPT2C6:$PC_{71}BM$ blends exhibited pitted holes and isolated islands respectively. These features are characteristic of a dewetting process. Newly prepared pristine EHPT2C6 films on PEDOT-PSS are relatively flat with 2.2 nm RMS roughness (Figure 2.5a) and do not exhibit any dewetting. Interestingly, micron long fibers (Figure 2.5b) are formed and the RMS roughness increases to 7.0 nm after 24 hours. This result suggests that EHPT2C6 has a tendency to dewet on PEDOT-PSS surfaces. It is possible that the ethyl-hexyl groups on EHPT2C6 enhance the hydrophobicity which leads to dewetting on the hydrophilic PEDOT-PSS surface. A previous work showed that the thin film dewetting morphology can be controlled by modifying the substrate surface energy.[59] It is interesting to note that the 80:20 EHPT2C6:$PC_{71}BM$ blend (Figure 2.5c) also exhibits a similar morphology to the day old pristine EHPT2C6 film. This suggests that $PC_{71}BM$ enhances the dewetting process. Previous works have shown that dewetting can occur in blends where the components have significant differences in surface energies or are immiscible.[59,60] We find that compound EHPT2C6 has a tendency to dewet on PEDOT-PSS surfaces which is further enhanced with the addition of $PC_{71}BM$. This dewetting process induces device optimization at a low donor:acceptor ratio of 10:90 where dewetting is not present.

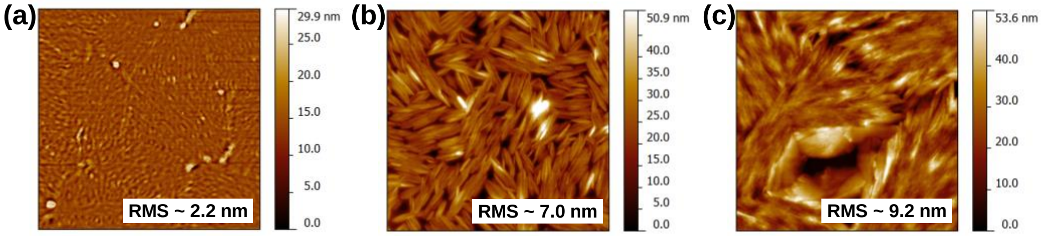

Figure 2.5. Topography images of a newly prepared pristine EHPT2C6 film (a) and the same film after 24 hours (b). Also shown is the topography for the 80:20 EHPT2C6:$PC_{71}BM$ films (c). All image scan sizes are 10 µm × 10 µm.

To further investigate how blend ratio impacts device performance the hole and electron mobilities where measured for the optimized blend films (Table 2). Table 2 shows that optimized blends of C6PT2C6 and EHPT2C6 yield hole mobilities of 1.9×10^{-5} and 2.2×10^{-6} cm^2/Vs, electron mobilities of 1.3×10^{-4} and 1.5×10^{-3} cm^2/Vs, and an electron to hole mobility ratio (μ_e/μ_h) of 6.8 and 677 respectively. We attribute the large difference in charge mobilities to the low donor and high PCBM content in the optimized 10:90 EHPT2C6:$PC_{71}BM$ device. It is possible that this imbalance in charge mobilities is a contributing factor in the lower FF and V_{OC} observed in the optimized EHPT2C6:$PC_{71}BM$ device. Previous works have also shown that an imbalance in hole and electron mobilities may enhance charge recombination thereby limiting the fill factor[61–65] and V_{OC}.[66,67] In summary, substituting the linear alkyl chains on C6PT2C6 with ethyl-hexyl groups to form EHPT2C6 leads to micron scale phase segregation at high donor:acceptor ratios thereby inducing device optimization at a low donor:acceptor ratio where performance is limited by an imbalance charge carrier mobility.

Table 2. Summary of mobilities for optimized blends

	Hole Mobility*	**Electron Mobility***	**μ_e/μ_h**
C6PT1C6	1.7E-06	1.7E-06	1.0
C6PT2C6	1.9E-05	1.3E-04	6.8
C6PT3C6	5.6E-07	5.4E-04	970
EHPT2C6	2.2E-06	1.5E-03	677
C6PT2	6.60E-06	5.8E-05	8.8

*All mobility values are in units of cm^2/Vs.

2.5 Impact of Removal of Linear Alkyl Chain at the End Units

Comparing C6PT2C6 and C6PT2 highlights the impact of removing linear alkyl chains on the terminal thiophenes. Table 1 shows that the C6PT2:$PC_{71}BM$ device optimizes at a 20:80 blend ratio and an annealing temperature of 80 °C which produces a V_{OC} of 0.87 V, J_{SC} of 4.33 mA/cm^2, FF of 0.30, and PCE of 1.11%. Relative to compound C6PT2C6, the optimized C6PT2 device has a nearly equivalent V_{OC} but a lower J_{SC}, and FF which leads to a reduced PCE. Figure 2.4k-o shows the blend film morphology of C6PT2:$PC_{71}BM$ films. Blend films of C6PT2:$PC_{71}BM$ exhibit micron scale phase segregation at high donor:acceptor ratios and device optimization at a low donor:acceptor ratio. A previous work showed that annealing pristine films of C6PT2 induces large plate like structures[58] and an increase in molecular ordering.[68] In comparison, blend films of C6PT2C6:$PC_{71}BM$ do no exhibit micron scale phase segregation in annealed films (Figure 2.4e). This result suggests that the removal of the linear alkyl chains on C6PT2C6 to form C6PT2 leads to a greater susceptibility for molecular ordering upon annealing.

Blend hole and electron mobility for the optimized C6PT2 films was measured at 1.9×10^{-6} and 5.8×10^{-5} cm^2/Vs resulting in μ_e/μ_h of 8.8 (Table 2). Interestingly, the optimized C6PT2C6 films yielded a similar μ_e/μ_h of 6.8. However, the hole and electron mobility in the optimized C6PT2C6 films are an order of magnitude greater than in the optimized C6PT2 films. In summary, removal of the linear alkyl chains on C6PT2C6 to form C6PT2 results in micron scale phase segregation at high donor:acceptor ratios thereby inducing device optimization at a low donor:acceptor ratio where performance is limited by poor charge mobility.

2.6 Impact of Conjugation Length

As previously discussed, replacement of linear alkyl chains on compound C6PT2C6 with ethyl-hexyl groups or removal of terminal thiophene alkyl chains leads to micron scale phase segregation at high donor:acceptor blend ratios. For this reason, compound C6PT2C6 was used to study the impact of conjugation length by varying the number of thiophene units along the conjugated backbone. Table 1 shows that the optimized 80 ^{0}C annealed 60:40 C6PT1C6:$PC_{71}BM$ device yields a V_{OC} of 1.00 V, J_{SC} of 3.64 mA/cm^2, FF of 0.35, and PCE of 1.25 %. In comparison, the optimized 80 ^{0}C annealed 20:80 C6PT3C6:$PC_{71}BM$ device yields a V_{OC} of 0.9 V, J_{SC} of 5.76 mA/cm^2, FF of 0.32, and PCE of 1.67 %. To investigate the differences in performance we first probed the surface morphology. Figure 2.4 shows the surface topography for the C6PT1C6, C6PT2C6, and C6PT3C6. All blend films are quite smooth with RMS roughness values between 1 - 5 nm. This result indicates that surface morphology is unable to explain the difference in device performance.

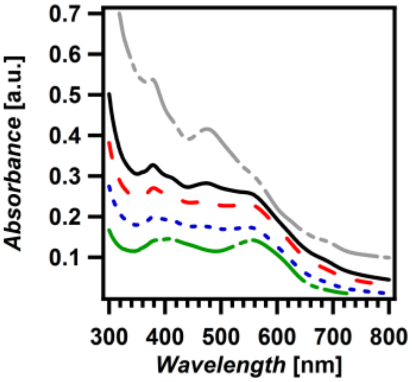

Figure 2.6. As-cast absorptions of C6PT3C6 with donor:PC$_{71}$BM blend ratios of 0:100 (double dotted dashed grey line), 20:80 (solid black line), 40:60 (dashed red line), 60:40 (dotted blue line), and 80:20 (dotted-dashed green line).

One of the main differences between compound C6PT1C6, C6PT2C6, and C6PT3C6 is the solubility which was previously measured at 228, 11, and 1.5 mg/mL respectively.[58] This result shows that solubility significantly drops when the conjugated backbone is increased. The low solubility of compound C6PT3C6 has a significant impact on the blend film absorption spectrum as shown in Figure 2.6. Figure 2.6 shows that the overall C6PT3C6:PC$_{71}$BM blend film absorption spectrums decreases with increasing donor:acceptor ratio. The decrease in absorption is attributed to the poor solubility of C6PT3C6 which precipitates at high donor:acceptor ratios thereby limiting the film thickness and overall absorption. As a consequence of the poor solubility, C6PT3C6 optimized at a low donor:acceptor blend ratio of 20:80 where the film thickness and overall absorption is greater.

The optimized 20:80 C6PT3C6:PC$_{71}$BM films yielded blend hole and electron mobility values of 5.6×10^{-7} and 5.5×10^{-4} cm^2/Vs respectively and a μ_e/μ_h of 970 (Table 2). The imbalance in charge mobilities is likely a contributing factor in the lower J_{SC}, FF, and PCE observed in the optimized C6PT3C6:PC$_{71}$BM device. In summary, extending the conjugation length of compound C6PT2C6 by two thiophene units significantly reduces the solubility thereby preventing the formation of thick films at high donor:acceptor ratios. The poor solubility induces C6PT3C6:$PC_{71}BM$ devices to optimize at a low donor:acceptor ratio where device performance is limited by poor exciton harvesting and charge mobility imbalanced.

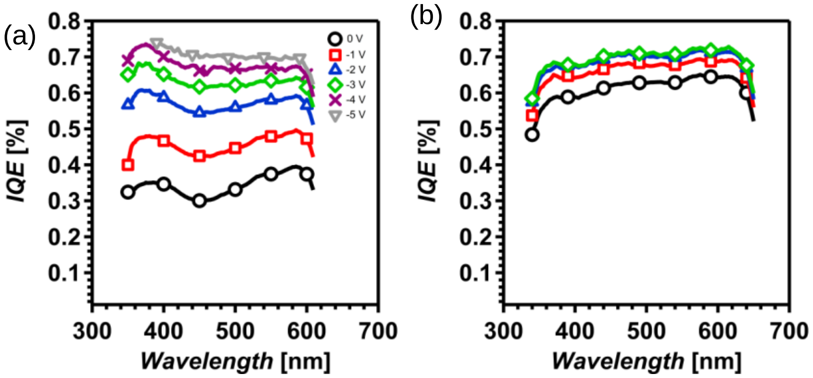

Figure 2.7. Bias dependent internal quantum efficiency of (a) 80 °C annealed 60:40 C6PT1C6:$PC_{71}BM$ and (b) 120 °C annealed 60:40 C6PT2C6:$PC_{71}BM$ blend. Internal quantum efficiency measured under zero, -1 V (black circle), -2 V (red square), -3V (blue upward triangle), -4V (purple ×), and -5V bias (grey downward triangle).

In contrast to C6PT3C6, compounds C6PT1C6 and C6PT2C6 have a greater solubility and optimized at a 60:40 donor:acceptor ratio in devices. As a result, compounds C6PT1C6 and C6PT2C6 serve as a good model system to investigate the impact of conjugation length on device performance when solubility is not a limiting factor. Figure 2.3 and Table 1 show that the optimized C6PT1C6 device has a greater V_{OC} but lower J_{SC} and FF relative to the optimized C6PT2C6 device. The greater V_{OC} can be explained by the lower lying HOMO level of C6PT1C6 at 5.63 V in comparison to the HOMO level of C6PT2C6 at 5.16 V. Relative to compound C6PT1C6, C6PT2C6 has two extra thiophene units. It is possible that the two additional electron donating thiophene units raise the HOMO level of C6PT2C6 thereby reducing the V_{OC} in C6PT2C6:$PC_{71}BM$ devices.

When the conjugation length of C6PT2C6 is decreased by two thiophene units to make C6PT1C6, the resulting J_{SC} of the optimized devices drops from 7.91 to 3.64 mA/cm^2. To investigate the differences in current generation between the optimized C6PT1C6 and C6PT2C6 devices, the EQE spectra (Figure 2.3b) were divided by the total active layer absorption to yield the internal quantum efficiency (IQE) spectra as shown in Figure 2.7. Figure 2.7a shows that the IQE of the optimized C6PT1C6 device increases from 30% to 70% when going from the short circuit condition to a -4 V applied reversed bias. In comparison, the IQE of the optimized C6PT2C6 device increases from 60% to 70% when going from short circuit conditions to a -2 V bias. At a strong reverse bias, the IQE of the optimized C6PT1C6 device increases by roughly 40% in comparison to only 10% for the optimized C6PT2C6 device. This result indicates that the charge collection efficiency is weaker in the optimized C6PT1C6:$PC_{71}BM$ device relative to the optimized C6PT2C6$PC_{71}BM$ device. Previous works have shown that charge collection efficiency and field dependent generation can be enhanced by applying a reverse bias.[63,69,70]

To further probe charge collection efficiency, the blend hole and electron mobilities were measured for the optimized C6PT1C6 and C6PT2C6 devices. Table 2 shows that the optimized C6PT1C6 and C6PT2C6 devices have hole mobilities of 1.7×10^{-6} cm^2/Vs and 1.9×10^{-5} cm^2/Vs respectively in addition to electron mobilities of 1.7×10^{-6} cm^2/Vs and 1.3×10^{-4} cm^2/Vs respectively. The optimized C6PT2C6 device has an overall greater electron and hole mobility than the optimized C6PT1C6 device. Previous works have also shown that a greater charge carrier mobility can enhance charge collection efficiency.[62–64,71]

In order to probe the charge collection in the donor phase, the optimized C6PT1C6 and C6PT2C6 devices where measured with photoconducting atomic force microscopy (pcAFM) as shown in Figure 2.8. Figure 2.8a shows that the optimized C6PT1C6 device lacks current contrast in the pcAFM image and has a peak current of about 8 pA. In comparison, Figure 2.8b shows that the optimized C6PT2C6 device yields 200 - 600 nm conductive domains with photocurrents up to 21 pA. Since a high work function gold tip was used, the brighter coloured domains represent hole collection from the donor phase.[72–75] This result indicates that the optimized C6PT2C6 devices has a greater charge collection efficiency from the donor phase than the optimized C6PT1C6 device. In summary, IQE and pcAFM measurements indicate that reducing the conjugation length of C6PT2C6 is to form C6PT1C6 leads to a drop in the charge collection efficiency which may explain its weaker device performance. In the following sections we further investigate this result using electron mobility, photoluminescence, and x-ray diffraction measurements.

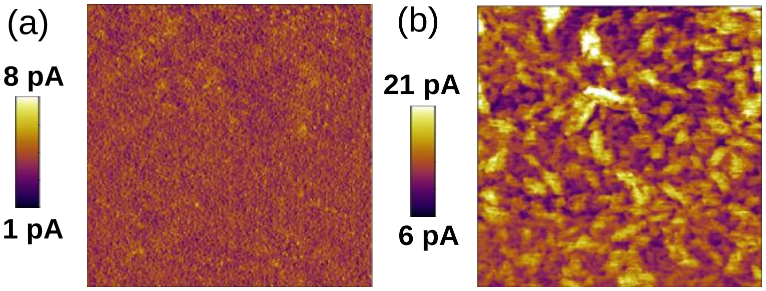

Figure 2.8. Photoconductive AFM images under white light and zero bias for the 80 °C 60:40 C6PT1C6:PC$_{71}$BM blend (a) and the 120 °C 60:40 C6PT2C6:PC71BM blend (b). All scan sizes are 2 µm × 2 µm.

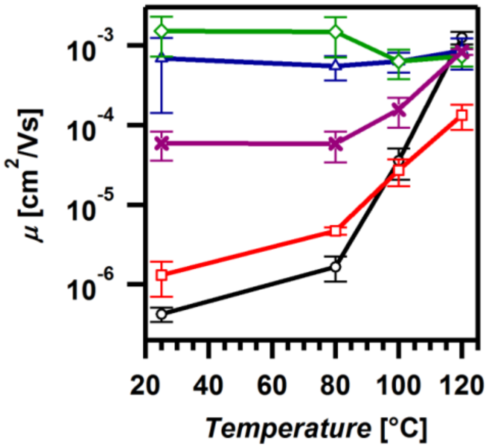

Figure 2.9. Electron mobility of 60:40 C6PT1C6:PC$_{71}$BM (black circles), 60:40 C6PT2C6:PC$_{71}$BM (red squares), 20:80 C6PT3C6:PC$_{71}$BM (blue triangles), 10:90 EHPT2C6:PC$_{71}$BM (green diamond) and 20:80 C6PT2:PC$_{71}$BM (purple ×) blend films as a function of annealing temperature. Films where annealed for 10 minutes at a given temperature.

2.7 Relationship between Annealing and Electron Mobility

Table 2 shows that the optimized C6PT2C6:PC$_{71}$BM device yields an electron mobility which is nearly two orders of magnitude greater than the optimized C6PT2C6:PC$_{71}$BM device. To investigate this result we measured the electron mobility of the optimized devices as a function of annealing temperature as shown in Figure 2.9. Figure 2.9 shows that the blend film electron mobility for the optimized C6PT1C6:PC$_{71}$BM and C6PT2C6:PC$_{71}$BM devices increases from 10^{-4} to 10^{-6} cm^2/Vs when going from as cast to 120 ^{0}C annealing. This result shows that annealing significantly enhances the electron mobility. Since C6PT1C6:PC$_{71}$BM optimizes at 80 ^{0}C annealing, the electron mobility remains around 10^{-6} cm^2/Vs. In comparison, C6PT2C6:PC$_{71}$BM optimizes at 120 ^{0}C which results in an electron mobility of around 10^{-4} cm^2/Vs. The enhanced electron mobility is likely to aid in charge collection from the acceptor phase and may explain why the optimized C6PT2C6 device yielded a greater short circuit current and fill factor relative to the optimized C6PT1C6 device. In the next section we investigate the driving for device optimization at a specific temperature.

2.8 Relationship between Annealing and Exciton Harvesting

Figure 2.9 showed that the C6PT2C6:PC$_{71}$BM device optimized at an elevated annealing temperature which enabled it to have a greater electron mobility than the optimized C6PT1C6:PC$_{71}$BM device. To further probe the driving for device optimization at a specific temperature the blend film photoluminescence was measured as a function of annealing temperature. Figure 2.10 shows the integrated steady state spectra normalized by the absorption at the excitation wavelength for the 60:40 C6PT1C6:PC$_{71}$BM and 60:40 C6PT2C6:PC$_{71}$BM blend films. The photoluminescence in the 60:40 C6PT1C6:PC$_{71}$BM blend film is shown to dramatically increase upon annealing at subsequent higher temperatures. In contrast, the 60:40 C6PT2C6:PC$_{71}$BM blend film only slightly increases upon annealing. An increase in photoluminescence indicates a weaker exciton harvesting efficiency. We observe that the exciton harvesting efficiency significantly drops when C6PT1C6:PC$_{71}$BM blend films are annealed at elevated temperatures. This result suggests that the C6PT1C6:PC$_{71}$BM blend films optimize at a lower annealing temperature in order to prevent exciton harvesting losses. In comparison, C6PT2C6:PC$_{71}$BM blend films to not exhibit a significant loss in exciton harvesting upon annealing which may explain why it is able to optimize at an elevated annealing temperature. In next section we investigate how chemical structure impacts the optimized annealing temperature.

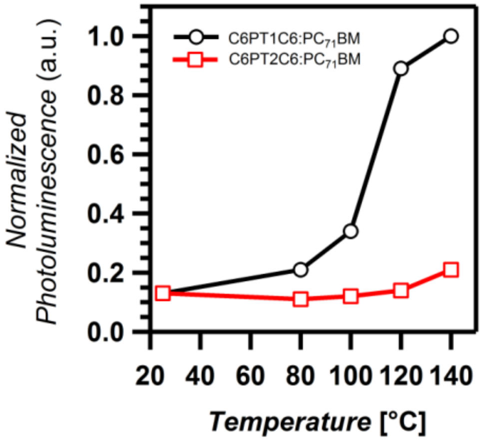

Figure 2.10. Photoluminescence as a function of annealing temperature for 60:40 C6PT1C6:$PC_{71}BM$ (black circles) and 60:40 C6PT2C6:$PC_{71}BM$ (red squares) blend films. Integrated photoluminescence was normalized by the absorption of the of each blend film at the 457 nm excitation wavelength.

2.9 Relationship between Conjugation Length and Molecular Ordering

Relative to C6PT1C6:$PC_{71}BM$ blend films, C6PT1C6:$PC_{71}BM$ blend films exhibit a significant increase in photoluminescence upon annealing at elevated temperatures (Figure 2.10). It is possible that the molecular ordering is greater in C6PT1C6:$PC_{71}BM$ blend films which induce phase segregation thereby reducing exciton harvesting and increasing photoluminescence. To further investigate the relationship between annealing temperature and molecular ordering, the thin film X-Ray diffraction (XRD) was measured for C6PT1C6:$PC_{71}BM$ and C6PT2C6:$PC_{71}BM$ blend films as a function of annealing temperatures (Figure 2.11).

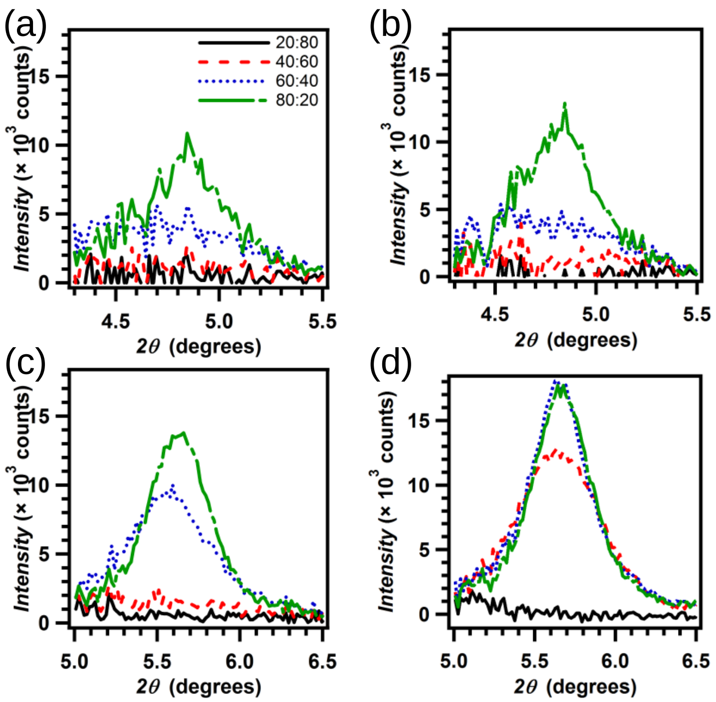

Figure 2.11. (a,c) As-cast and (b,d) 80 ºC annealed XRD patterns of C6PT1C6 (a-b) abd C6PT2C6 (c-d) with donor:PC$_{71}$BM blend ratios of 20:80 (solid black line), 40:60 (dashed red line), 60:40 (dotted blue line), and 80:20 (dotted-dashed green line).

Figure 2.11 shows that the C6PT2C6:PC$_{71}$BM blend films XRD intensities do not significantly increase when as-cast (Figure 2.11a) films are annealed to 80 ^{0}C (Figure 2.11b). In comparison, C6PT1C6:PC$_{71}$BM blend films exhibit a significant increase in XRD intensities when as-cast (Figure 2.11c) blends are annealed to 80 ^{0}C (Figure 2.11d). This result suggests that C6PT1C6 has a greater affinity for molecular ordering than C6PT2C6. In a previous work the atomic force microscopy (AFM) was used to probe the topography of as-cast and 100 ^{0}C annealed pristine C6PT1C6 and C6PT2C6 films.[58] Both materials exhibited plate like structures in thin films. Relative to C6PT2C6, annealing C6PT1C6 films resulted in a significantly greater increase in the size of the plate like structures. These results suggest that C6PT1C6 has a greater affinity for molecular ordering which induces significant phase segregation in blend films when annealed. An increase in order with decreasing conjugation length is similar to the findings of Liu et al.[76] In summary, increasing the conjugation length of C6PT1C6 by two thiophene units to form C6PT2C6 reduces molecular ordering and phase segregation thereby allowing for device optimization at higher annealing temperatures where electron mobility is enhanced and likely contributes to the greater short circuit current and fill factor observed in the optimized C6PT2C6:$PC_{71}BM$ devices.

2.10 Conclusions

The solar cell performance of a series of DPP small molecules blended with $PC_{71}BM$ was investigated as a function of chemical structure, the type of solubilizing group, conjugation length, and processing condition. We show that simple chemical modification such as increasing molecular bulkiness and removal of linear alkyl chains can destabilize blend film morphology at high donor:acceptor ratios thereby inducing device optimization at low donor:acceptor blend ratios where device performance is limited by poor exciton harvesting and charge mobility imbalance. We also show that the conjugation length can be used to fine tune the energy level, solubility, and molecular ordering of a compound. Over-extending the conjugation length significantly reduces the solubility thereby preventing the formation of thick films. In contrast, decreasing the conjugation length past a critical limit enhances molecular ordering which may prevent device optimization at an elevated annealing temperature due to large phase segregation. We find that device optimization at higher blend ratios and elevated annealing temperatures can enhance charge collection in the donor and acceptor phase. In this class of materials, the optimal performance arises when using linear alkyl chain solubilizing groups along with an intermittent conjugation length**.**

2.11 Experimental

The synthesis for the five donor materials has been previously reported.[58] Glass substrates coated with 150 nm of Indium tin oxide (ITO, Thin Film Devices) were sonicated for 15 minutes in acetone and isopropanol respectively. The ITO substrates were then baked in an oven overnight and treated with UV/ozone (UVO Cleaner 42, Jelight Co., Inc.) for one hour. PEDOT:PSS (Baytron 4083) was spin casted at 2,500 rpm for 60 seconds and subsequently annealed at 140 ºC for 15 minutes to yield a thickness of 55 nm. The films were briefly vacuumed while transferring though the small transfer chamber into the nitrogen glove box. Each DPP donor was blended with $PC_{71}BM$ (Nano-C, USA) with an overall concentration of 2% (wt/vol) in anhydrous chloroform (Sigma-Aldrich) at donor:acceptor ratios of 10:90, 20:80, 30:70, 40:60, 50:50, 60:40, 70:30, and 80:20. All blend solutions were heated overnight at 60 ºC with a stir rate of 300 rpm. In order to obtain high quality films without the presence of comets or foggy halos the hot (60 ºC) solution was passed through a 0.45 µm poly(tetrafluoroethylene) (PTFE) filter directly onto the ITO/PEDOT:PSS substrate prior to spin casting. All films were spin casted at 2,500 rpm for 15 seconds. PEDOT:PSS and active layer thicknesses were measured with an Ambios XP-100 Stylus profilometer.

After scratching off part of the active layer for the bottom (anode) contact, 110 nm of aluminium was evaporated onto the substrates starting slightly below 1 Å/s and increased to 2 Å/s once 20 nm of aluminium (Al) was deposited under a pressure of 1×10^{-7} Torr at room temperature. A shadow mask was used for the Al deposition and resulted in a device area of 19 mm^2. Each condition was tested with 15 devices. Device efficiencies were measured with a 150 Watt Newport-Oriel AM 1.5G light source calibrated to 100 mW/cm^2 with a National Renewable Energy Laboratory certified silicon diode fitted with a KG1 optical filter. External quantum efficiencies were measured with a Xe lamp, monochromator, optical chopper, and lock-in amplifier. To study the effects of annealing, films were annealed at 80 ºC for 10 minutes and then quenched by placing on the glove box metal surface. To study higher annealing temperatures the same film was annealed at a higher temperature for 10 minutes.

The UV-Vis absorption spectra of blend films were measured with a Beckman Coulter DU 800 Spectrometer. Tapping mode AFM images were measured in ambient on an Innova Scanning Probe Microscope (Veeco) using silicon-nitride probes (Budget Sensors) with a spring constant of ~3 N/m and a resonant frequency of 75 KHz. Photoconducting images were measured on an Asylum Research MFP-3D microscope sitting atop of an inverted optical microscopy (Olympus, IX71). To prevent exposure to air, nitrogen was flowed through a fluid cell containing the device while the current was recorded by internal preamplifier (Asylum Research ORCA head model). Gold-coated silicon probes (Budget Sensors) with a spring constant of 0.2 nN/m and a resonant frequency of 13 kHz were used. A white light source was focused on the sample with an inverted optical microscope (Olympus) resulting in an illumination spot size approximately 160 μm in diameter. The Gold-coated silicon probe was subsequently position at the center of the illumination spot. All images were scanned under short circuit conditions.

Thin-film XRD spectra were measured on device architectures of ITO/PEDOT:PSS/Blend with a X'Pert Phillips Material Research Diffractometer. Samples were scanned at 45kV and 40 mA with a scanning rate of 0.004 degree per second, and Cu K_α radiation (wavelength $\lambda = 1.5405$ Å). In the 2θ-ω scan configurations each film was scanned from 4 to 30 2θ.

The diode hole mobility for pristine and optimized blend films were measured by fabricating a hole only device with a ITO/PEDOT:PSS/Blend or pristine/MoOx/Au device structure. The MoOx and Au layer had thickness of 10 and 60 nm. Electron mobility was measured by fabricating devices with a Glass/Al/Blend or pristine/Al geometry. Current density as a function of voltage was measured on a Keithly 4200 in a Nitrogen atmosphere. To extract mobility values the current density-voltage curved were fitted to the Mott Gurney relationship (space charge limited current).[77]

Internal quantum efficiency was determined by dividing the EQE by the active layer absorption. The total absorption was first measured on a Perkin Elmer Lambda 750 using an integrating sphere with the same device structure used in solar cells. A transfer matrix model[78] was then used to model parasitic absorbance from the electrodes. To calculate the active layer absorption, the modeled parasitic absorption was subtracted from the measured total absorption.

Steady-state fluorescence experiments at room temperature were performed using a Fluorolog Jobin Yvon Spex equipped with a Xenon lamp excitation source. All samples were excited at 457 nm and collected in the front face orientation.

2.12 Reference

(1) Günes, S.; Neugebauer, H.; Sariciftci, N. S. *Chem. Rev.* **2007**, *107*, 1324–1338.
(2) Bundgaard, E.; Krebs, F. C. *Sol. Energy Mater. Sol. Cells* **2007**, *91*, 954–985.
(3) Brabec, C. J. *Sol. Energy Mater. Sol. Cells* **2004**, *83*, 273–292.
(4) Murphy, A. R.; Fréchet, J. M. J. *Chem. Rev.* **2007**, *107*, 1066–1096.
(5) Chu, T.-Y.; Lu, J.; Beaupré, S.; Zhang, Y.; Pouliot, J.-R.; Wakim, S.; Zhou, J.; Leclerc, M.; Li, Z.; Ding, J.; Tao, Y. *J. Am. Chem. Soc.* **2011**, *133*, 4250–4253.
(6) He, Z.; Zhong, C.; Huang, X.; Wong, W.; Wu, H.; Chen, L.; Su, S.; Cao, Y. *Adv. Mater.* **2011**, *23*, 4636–4643.
(7) Dou, L.; You, J.; Yang, J.; Chen, C.-C.; He, Y.; Murase, S.; Moriarty, T.; Emery, K.; Li, G.; Yang, Y. *Nat. Photonics* **2012**, *6*, 180–185.
(8) Mishra, A.; Bäuerle, P. *Angew. Chem. Int. Ed.* **2012**, *51*, 2020–2067.
(9) Li, Z.; He, G.; Wan, X.; Liu, Y.; Zhou, J.; Long, G.; Zuo, Y.; Zhang, M.; Chen, Y. *Adv. Energy Mater.* **2012**, *2*, 74–77.
(10) Zhou, J.; Wan, X.; Liu, Y.; Zuo, Y.; Li, Z.; He, G.; Long, G.; Ni, W.; Li, C.; Su, X.; Chen, Y. *J. Am. Chem. Soc.* **2012**, *134*, 16345–16351.
(11) Green, M. A.; Emery, K.; Hishikawa, Y.; Warta, W.; Dunlop, E. D. *Prog. Photovolt. Res. Appl.* **2012**, *20*, 12–20.
(12) Love, J. A.; Proctor, C. M.; Liu, J.; Takacs, C. J.; Sharenko, A.; van der Poll, T. S.; Heeger, A. J.; Bazan, G. C.; Nguyen, T.-Q. *Adv. Funct. Mater.* **2013**, *23*, 5019–5026.
(13) Coffin, R. C.; Peet, J.; Rogers, J.; Bazan, G. C. *Nat Chem* **2009**, *1*, 657–661.
(14) Kim, Y.; Cook, S.; Kirkpatrick, J.; Nelson, J.; Durrant, J. R.; Bradley, D. D. C.; Giles, M.; Heeney, M.; Hamilton, R.; McCulloch, I. *J. Phys. Chem. C* **2007**, *111*, 8137–8141.
(15) Lloyd, M. T.; Anthony, J. E.; Malliaras, G. G. *Mater. Today* **2007**, *10*, 34–41.
(16) Walker, B.; Tamayo, A. B.; Dang, X.-D.; Zalar, P.; Seo, J. H.; Garcia, A.; Tantiwiwat, M.; Nguyen, T.-Q. *Adv. Funct. Mater.* **2009**, *19*, 3063–3069.
(17) Roncali, J. *Acc. Chem. Res.* **2009**, *42*, 1719–1730.
(18) Wei, G.; Wang, S.; Renshaw, K.; Thompson, M. E.; Forrest, S. R. *ACS Nano* **2010**, *4*, 1927–1934.
(19) Yin, B.; Yang, L.; Liu, Y.; Chen, Y.; Qi, Q.; Zhang, F.; Yin, S. *Appl. Phys. Lett.* **2010**, *97*, 023303.
(20) Liu, Y.; Wan, X.; Wang, F.; Zhou, J.; Long, G.; Tian, J.; Chen, Y. *Adv. Mater.* **2011**.
(21) Walker, B.; Kim, C.; Nguyen, T.-Q. *Chem. Mater.* **2011**, *23*, 470–482.
(22) Mikroyannidis, J. A.; Tsagkournos, D. V.; Sharma, S. S.; Vijay, Y. K.; Sharma, G. D. *J Mater Chem* **2011**, *21*.
(23) Wei, G.; Wang, S.; Sun, K.; Thompson, M. E.; Forrest, S. R. *Adv. Energy Mater.* **2011**, *1*, 184–187.
(24) Ko, H. M.; Choi, H.; Paek, S.; Kim, K.; Song, K.; Lee, J. K.; Ko, J. *J. Mater. Chem.* **2011**, *21*, 7248–7253.

(25) Welch, G. C.; Perez, L. A.; Hoven, C. V.; Zhang, Y.; Dang, X.-D.; Sharenko, A.; Toney, M. F.; Kramer, E. J.; Nguyen, T.-Q.; Bazan, G. C. *J. Mater. Chem.* **2011**, *21*, 12700–12709.

(26) Liu, Y.; Wan, X.; Wang, F.; Zhou, J.; Long, G.; Tian, J.; You, J.; Yang, Y.; Chen, Y. *Adv. Energy Mater.* **2011**, *1*, 771–775.

(27) Sun, Y.; Welch, G. C.; Leong, W. L.; Takacs, C. J.; Bazan, G. C.; Heeger, A. J. *Nat. Mater.* **2012**, *11*, 44–48.

(28) Van der Poll, T. S.; Love, J. A.; Nguyen, T.-Q.; Bazan, G. C. *Adv. Mater.* **2012**, *24*, 3646–3649.

(29) Tamayo, A. B.; Tantiwiwat, M.; Walker, B.; Nguyen, T.-Q. *J. Phys. Chem. C* **2008**, *112*, 15543–15552.

(30) Tantiwiwat, M.; Tamayo, A.; Luu, N.; Dang, X.-D.; Nguyen, T.-Q. *J. Phys. Chem. C* **2008**, *112*, 17402–17407.

(31) Huo, L.; Hou, J.; Chen, H.-Y.; Zhang, S.; Jiang, Y.; Chen, T. L.; Yang, Y. *Macromolecules* **2009**, *42*, 6564–6571.

(32) Zou, Y.; Gendron, D.; Neagu-Plesu, R.; Leclerc, M. *Macromolecules* **2009**, *42*, 6361–6365.

(33) Jo, J.; Gendron, D.; Najari, A.; Moon, J. S.; Cho, S.; Leclerc, M.; Heeger, A. J. *Appl. Phys. Lett.* **2010**, *97*, 203303.

(34) Bijleveld, J. C.; Gevaerts, V. S.; Di Nuzzo, D.; Turbiez, M.; Mathijssen, S. G. J.; de Leeuw, D. M.; Wienk, M. M.; Janssen, R. A. J. *Adv. Mater.* **2010**, *22*, E242–E246.

(35) Kanimozhi, C.; Balraju, P.; Sharma, G. D.; Patil, S. *J. Phys. Chem. B* **2010**, *114*, 3095–3103.

(36) Badrou Aïch, R.; Zou, Y.; Leclerc, M.; Tao, Y. *Org. Electron.* **2010**, *11*, 1053–1058.

(37) Zhang, G.; Xu, H.; Liu, K.; Li, Y.; Yang, L.; Yang, M. *Synth. Met.* **2010**, *160*, 1945–1952.

(38) Woo, C. H.; Beaujuge, P. M.; Holcombe, T. W.; Lee, O. P.; Fréchet, J. M. J. *J. Am. Chem. Soc.* **2010**, *132*, 15547–15549.

(39) Hendriks, K. H.; Heintges, G. H. L.; Gevaerts, V. S.; Wienk, M. M.; Janssen, R. A. J. *Angew. Chem. Int. Ed.* **2013**, *52*, 8341–8344.

(40) Ripaud, E.; Demeter, D.; Rousseau, T.; Boucard-Cétol, E.; Allain, M.; Po, R.; Leriche, P.; Roncali, J. *Dyes Pigments* **2012**, *95*, 126–133.

(41) Liu, J.; Walker, B.; Tamayo, A.; Zhang, Y.; Nguyen, T.-Q. *Adv. Funct. Mater.* **2013**, *23*, 47–56.

(42) Langhals, H.; Demmig, S.; Potrawa, T. *J. Für Prakt. Chem.* **1991**, *333*, 733–748.

(43) Mizuguchi, J. *J. Phys. Chem. A* **2000**, *104*, 1817–1821.

(44) Tamayo, A. B.; Walker, B.; Nguyen*, T.-Q. *J. Phys. Chem. C* **2008**, *112*, 11545–11551.

(45) Lunák Jr., S.; Vynuchal, J.; Hrdina, R. *J. Mol. Struct.* **2009**, *919*, 239–245.

(46) Tamayo, A.; Kent, T.; Tantitiwat, M.; Dante, M. A.; Rogers, J.; Nguyen, T.-Q. *Energy Environ. Sci.* **2009**, *2*, 1180.

(47) Tamayo, A. B.; Dang, X.-D.; Walker, B.; Seo, J.; Kent, T.; Nguyen, T.-Q. *Appl. Phys. Lett.* **2009**, *94*, 103301.

(48) Weiter, M.; Salyk, O.; Bednár, P.; Vala, M.; Navrátil, J.; Zmeskal, O.; Vynuchal, J.; Lunák Jr., S. *Mater. Sci. Eng. B* **2009**, *165*, 148–152.

(49) Karsten, B. P.; Bijleveld, J. C.; Janssen, R. A. J. *Macromol. Rapid Commun.* **2010**, *31*, 1554–1559.

(50) Sonar, P.; Ng, G.-M.; Lin, T. T.; Dodabalapur, A.; Chen, Z.-K. *J. Mater. Chem.* **2010**, *20*, 3626.

(51) Kylberg, W.; Sonar, P.; Heier, J.; Tisserant, J.-N.; Müller, C.; Nüesch, F.; Chen, Z.-K.; Dodabalapur, A.; Yoon, S.; Hany, R. *Energy Environ. Sci.* **2011**, *4*, 3617.

(52) Loser, S.; Bruns, C. J.; Miyauchi, H.; Ortiz, R. P.; Facchetti, A.; Stupp, S. I.; Marks, T. J. *J. Am. Chem. Soc.* **2011**, *133*, 8142–8145.

(53) Boudreault, P.-L. T.; Hennek, J. W.; Loser, S.; Ortiz, R. P.; Eckstein, B. J.; Facchetti, A.; Marks, T. J. *Chem. Mater.* **2012**, *24*, 2929–2942.

(54) Lee, J. W.; Choi, Y. S.; Jo, W. H. *Org. Electron.* **2012**, *13*, 3060–3066.

(55) Liu, J.; Walker, B.; Tamayo, A.; Zhang, Y.; Nguyen, T.-Q. *Adv. Funct. Mater.* **2013**, *23*, 2–2.

(56) Shin, W.; Yasuda, T.; Watanabe, G.; Yang, Y. S.; Adachi, C. *Chem. Mater.* **2013**, *25*, 2549–2556.

(57) Lee, O. P.; Yiu, A. T.; Beaujuge, P. M.; Woo, C. H.; Holcombe, T. W.; Millstone, J. E.; Douglas, J. D.; Chen, M. S.; Fréchet, J. M. J. *Adv. Mater.* **2011**, *23*, 5359–5363.

(58) Kim, C.; Liu, J.; Lin, J.; Tamayo, A. B.; Walker, B.; Wu, G.; Nguyen, T.-Q. *Chem Mater* **2012**, *24*, 1699–1709.

(59) Tisserant, J.-N.; Hany, R.; Partel, S.; Bona, G.-L.; Mezzenga, R.; Heier, J. *Soft Matter* **2012**, *8*, 5804–5810.

(60) Nilsson, S.; Bernasik, A.; Budkowski, A.; Moons, E. *Macromolecules* **2007**, *40*, 8291–8301.

(61) Blom, P. W. M.; Mihailetchi, V. D.; Koster, L. J. A.; Markov, D. E. *Adv. Mater.* **2007**, *19*, 1551–1566.

(62) Tress, W.; Petrich, A.; Hummert, M.; Hein, M.; Leo, K.; Riede, M. *Appl. Phys. Lett.* **2011**, *98*, 063301.

(63) Albrecht, S.; Schindler, W.; Kurpiers, J.; Kniepert, J.; Blakesley, J. C.; Dumsch, I.; Allard, S.; Fostiropoulos, K.; Scherf, U.; Neher, D. *J. Phys. Chem. Lett.* **2012**, *3*, 640–645.

(64) Proctor, C. M.; Kim, C.; Neher, D.; Nguyen, T.-Q. *Adv. Funct. Mater.* **2013**, *23*, 3584–3594.

(65) Tress, W.; Merten, A.; Furno, M.; Hein, M.; Leo, K.; Riede, M. *Adv. Energy Mater.* **2013**, *3*, 631–638.

(66) Blakesley, J. C.; Neher, D. *Phys. Rev. B* **2011**, *84*, 075210.

(67) Credgington, D.; Durrant, J. R. *J. Phys. Chem. Lett.* **2012**, *3*, 1465–1478.

(68) Mikhnenko, O. V.; Lin, J.; Shu, Y.; Anthony, J. E.; Blom, P. W. M.; Nguyen, T.-Q.; Loi, M. A. *Phys. Chem. Chem. Phys.* **2012**, *14*, 14196–14201.

(69) Albrecht, S.; Janietz, S.; Schindler, W.; Frisch, J.; Kurpiers, J.; Kniepert, J.; Inal, S.; Pingel, P.; Fostiropoulos, K.; Koch, N.; Neher, D. *J. Am. Chem. Soc.* **2012**, *134*, 14932–14944.

(70) Credgington, D.; Jamieson, F. C.; Walker, B.; Nguyen, T.-Q.; Durrant, J. R. *Adv. Mater.* **2012**, *24*, 2135–2141.

(71) Cowan, S. R.; Street, R. A.; Cho, S.; Heeger, A. J. *Phys. Rev. B* **2011**, *83*, 035205.

(72) Coffey, D. C.; Reid, O. G.; Rodovsky, D. B.; Bartholomew, G. P.; Ginger, D. S. *Nano Lett.* **2007**, *7*, 738–744.

(73) Dang, X.-D.; Tamayo, A. B.; Seo, J.; Hoven, C. V.; Walker, B.; Nguyen, T.-Q. *Adv. Funct. Mater.* **2010**, *20*, 3314–3321.

(74) Hoven, C. V.; Dang, X.-D.; Coffin, R. C.; Peet, J.; Nguyen, T.-Q.; Bazan, G. C. *Adv. Mater.* **2010**, *22*, E63–E66.

(75) Guide, M.; Dang, X.-D.; Nguyen, T.-Q. *Adv. Mater.* **2011**, *23*, 2313–2319.

(76) Liu, F.; Gu, Y.; Wang, C.; Zhao, W.; Chen, D.; Briseno, A. L.; Russell, T. P. *Adv. Mater.* **2012**, *24*, 3947–3951.

(77) Lampert, M. A.; Mark, P. *Current injection in solids*; Academic Press, 1970.

(78) Burkhard, G. F.; Hoke, E. T.; McGehee, M. D. *Adv. Mater.* **2010**, *22*, 3293–3297.

Chapter 3. Systematic study of exciton diffusion length in organic semiconductors by six experimental methods

3.1 Introduction

Several methods have been used to measure exciton diffusion length; however, it is unclear which methods are more reliable for a given situation. Reported techniques to measure exciton diffusion length include photoluminescence (PL) surface quenching,[1–11] time-resolved PL bulk quenching modeled with a Monte Carlo simulation,[12,13] exciton-exciton annihilation,[7,14–17] modeling of solar cell photocurrent spectrum,[9,18–28] time-resolved microwave conductance,[29–31] spectrally resolved PL quenching,[32–35] and Förster resonance energy transfer theory.[32,33,36] Currently, there is little known on how the value of the measured exciton diffusion length of the same material can vary depending on the technique employed. Consequently, it is difficult to draw conclusions regarding the structure-property relationships across previous studies.

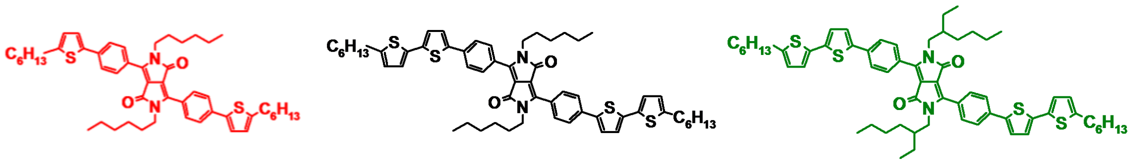

A

B

C

Figure 3.1. Chemical structures for compounds A, B, and C.

In this work, a thorough investigation has been performed to study the dependence of exciton diffusion length on chemical structure using six experimental techniques. We have utilized phenyl substituted diketopyrrolopyrrole (DPP) small molecules (Figure 3.1) as our model system. The chemical structure has been systematically modified in regards to conjugation length and functional groups. We show that decreasing the conjugation length increases molecular ordering, which is correlated with an enhancement of exciton diffusion length.

3.2 Background

In general, a diffusion length is defined as the root mean squared displacement of a particle from its initial position during time τ[37]:

$$L_D = \sqrt{\frac{\sum dL_i^2}{N}} = \sqrt{2ZD\tau}, \tag{1}$$

where dL_i is the displacement of a particle i from its original position and N is the total number of excitons. In the case of one-, two-, or three- dimensional diffusion, Z is equal to 1, 2, or 3, respectively.[37] However, in context of exciton diffusion a $\sqrt{2}$ factor is often omitted in Equation (1) and the values of L_D are often reported for the one-dimensional case:

$$L_D = \sqrt{D\tau}. \tag{2}$$

To be consistent with literature, we use Equation (2) in this work to define the exciton diffusion length.

3.3 Steady-state and Time-resolved Photoluminescence Surface Quenching

Steady-state PL surface quenching (SS-SQ) and time-resolved PL surface quenching (TR-SQ) are two techniques which have been often employed to measure exciton diffusion length.[1–11] In surface quenching techniques, bi-layers are prepared of an organic semiconductor and an exciton quenching layer. Samples are excited with a laser and PL intensity or PL decay time is detected. Then the PL of bi-layers is compared with thin films that do not have the quenching layer. The PL of bi-layers appears to be much weaker with shorter decay time if the thickness of organic semiconductor is of the order of the exciton diffusion length. By modelling PL quenching efficiency one extracts the exciton diffusion length and diffusion coefficient. Surface quenching techniques are advantageous because the exciton diffusion length is measured directly.

Due to a large number of assumptions and requirements with surface quenching techniques, it is difficult to accurately use these methods in practice. Thin film morphology must be consistent across the thickness range of typically 5 - 50 nm. This is likely not the case for crystalline and semi crystalline materials. As discussed in Section 3.9, spectroscopic ellipsometry measurements on films of A, B, and C of varying thicknesses showed that all films are predominantly isotropic. Where therefore expect the morphology of films A, B, and C to be consistent across the thicknesses explored in this work. Surface quenching techniques also require a sharp interface between the organic semiconductor and exciton quencher layers. The surface roughness of both layers must be less than 1 nm on the area of 100 μm^2. And finally, the excitons quenching efficiency must be known at interfaces with exciton quenching layer, vacuum, and with substrate (usually quartz).

A common challenge when employing the SS-SQ and TR-SQ techniques is finding a quencher that has a high quenching efficiency and the ability to form a sharp bilayer interface with the organic semiconductor. In this study, the choice of quencher was chosen by measuring the TR PL on bilayers films consisting of a thin (~ 5 nm) layer of compound B with TiO_2,[5] [6,6]-Phenyl C61 butyric acid (PCBA) modified TiO_2, N719 ruthenium dye modified TiO$_2$,[5] poly(benzimidazobenzophenanthroline ladder) (BBL),[38–41] or evaporated C$_{60}$ (Figure 3.2). Of the quenchers tested, evaporated C$_{60}$ quenched the PL of compound B the greatest. As a result, the SS-SQ and TR-SQ techniques were performed using a 4 nm evaporated C$_{60}$ layer to serve as the quencher. It should be noted that we cannot rule out the possibility of C$_{60}$ diffusion into the organic semiconductor layer. Inter-diffusion would enhance the quenching efficiency and lead to an overestimation of the exciton diffusion length.

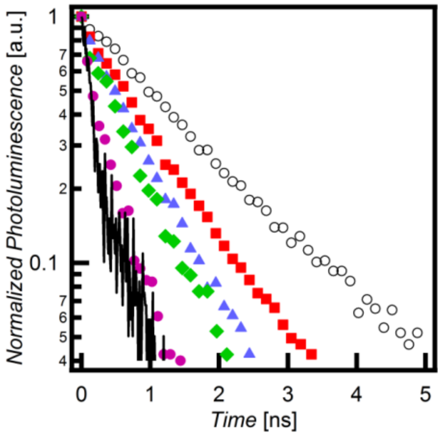

Figure 3.2. Time resolved PL of a thin (~ 5 nm) layer of B with a quenching layer of TiO$_2$ (red square), PCBA modified TiO$_2$ (blue triangle), N719 modified TiO$_2$ (green diamond), BBL (purple circle), or C$_{60}$ (black line). Time resolved PL was also measured on a thin (~ 5 nm) layer of B without a quencher (open circle) for reference.

In regards to the fabrication procedure, microscope slides (Corning Inc.) with 1 mm thicknesses were cut into 40 × 40 mm squares. The surface root mean squared (RMS) roughness was measured at 1 nm with atomic force microscopy. All glass slides were manually scrubbed with unscented liquid dish soap (Ivory) and sonicated (Fisher Scientific) in a series of deionized water, acetone, and isopropanol (VWR International) for 15 minutes each. Slides were then dried under nitrogen stream and stored overnight in a 90 °C laboratory oven. All organic semiconductor materials were synthesized in-house as previously reported.[42] All solutions and film preparation were done in a nitrogen filled glove box. Solutions were prepared at 14 mg/mL with anhydrous chloroform (Sigma Aldrich). Solutions were left to stir overnight at 60 °C.

Solutions were spun onto the cleaned microscope slides with a deposition volume of 100 μL, spin rate of 1,500 rpm, and a spin time of 60 seconds. The film thickness was varied by subsequently diluting the stock solution followed by spin casting. This procedure was repeated in order to obtain concentrations ranging from 14 mg/mL to 1 mg/mL. We used shadow mask to evaporate C_{60} on only half of the substrate. The samples were transferred into an evaporation chamber inside a glovebox, which was subsequently evacuated to 10^{-7} torr (Angstrom Engineering). Approximately 4 nm of C_{60} (Fisher Scientific) was thermally evaporated onto the samples at a rate of 0.1 Å per second.

To protect the films from ambient conditions the samples were encapsulated inside the nitrogen glovebox. A Teflon tweezer was used to scrape the previously deposited materials off of the glass in a band ~2 - 4 mm of from the edges of the glass, providing a bare glass perimeter around the center of the sample to which a two-part epoxy (Kimball Midwest) was then applied. A second 40 × 40 mm bare glass slide was placed on top of the epoxy and left to cure for two hours. Scraping off the organic layer with a Teflon tweezer strengthens the encapsulation thereby preventing delamination and oxygen diffusion into the encapsulated films. After the epoxy cured, the samples were removed from the glovebox for measurements. The finalized films had a film structure of glass/organic semiconductor/nitrogen/glass. The procedure above was repeated for 10 different thicknesses of the organic semiconductor with and without a quenching layer.

Steady-state PL measurements were performed using an Ar^+-laser (Spectraphysics Beamlok 2060) tuned to 457 nm wavelength. The excitation laser beam was incident normal to the glass substrate used for deposition of the organic layers. PL was collected normal from glass substrate used for encapsulation on the opposite side of the sample. An interference long wavelength-pass filter (Omega Filters) was used to block the excitation light. The PL was focused on the entrance slit of a monochromator (Acton SP-500) by a system of lenses. The spectra were recorded using spectroscopic charge-coupled device (CCD) camera (Princeton Instruments PIXIS:400). PL life-time measurements were performed using Time-Correlated Single Photon Counting (TCSPC) technique.[43] Approximately 200 femtosecond (fs) excitation pulses with wavelength 400 nm were generated by doubling the fundamental frequency of fs Ti:Sapphire laser (Coherent Mira 900) pulses in a commercial optical harmonic generator (Inrad). The laser repetition rate was reduced to 2 MHz by a home-made acousto-optical pulse picker in order to avoid saturation of the chromophore. TCSPC system is equipped with an ultrafast microchannel plate photomultiplier tube detector (Hamamatsu R3809U-51) and electronics board (Becker & Hickl SPC-630) and has instrument response time about 60-65 picoseconds. Triggering signal for the TCSPC board was generated by sending a small fraction of the laser beam onto a fast (400 MHz bandwidth) Si photodiode (Thorlabs Inc.). The pulsed laser beam was aligned collinearly with the CW laser beam and the same optical system, laser blocking filter, and monochromator were used for time-resolved and steady-state PL measurements. The mean excitation power for the steady-state and time-resolved PL measurements were measured at 1.6 and 1.1 W/cm^2, respectively. When applying the SS-SQ technique it is assumed that the absorption from the quenching layer is negligible. For this reason is preferable to use very thin layers of C_{60} or TiO_2.

Upon completion of PL measurements all films were pried open with a razor blade. Exposed films were then characterized with spectroscopic ellipsometry (J.A. Woollam Co., Inc.) to yield the film thickness and optical constants of all the layers (see Section 3.9). The exposed films were also characterized with tapping mode atomic force microscopy (Innova) to yield the RMS roughness. All films in this study have RMS roughness values around 1 nm. Thicknesses were also measured with a profilometer (Abios XP-100) which showed good agreement with thicknesses obtained from ellipsometry.

Figure 3.3 shows the steady-state PL spectrum for bilayers consisting of a 4 nm evaporated C_{60} layer on top of a film of A (Figure 3.3a), B (Figure 3.3b), and C (Figure 3.3c) of varying thicknesses. For thin films (~ 11 nm) the integrated steady-state PL for bilayers with a C_{60} quenching layer is significantly less than that of the control film without C_{60}. In contrast, for thick films (~ 65 – 85 nm) the integrated steady-state PL for bilayers with and without a C_{60} quenching layer are nearly equivalent. PL spectra were used to calculate the relative quenching efficiencies Q:

$$Q = 1 - \frac{\int PL_{quencher}\, d\lambda}{\int PL_{pristine}\, d\lambda} \tag{3}$$

where $\int PL_{quencher} d\lambda$ and $\int PL_{pristine} d\lambda$ are the integrated PL for the bilayers films with quencher and the pristine films without quencher respectively. The PL decay was normalized to the value at t = 0 prior to the integration.

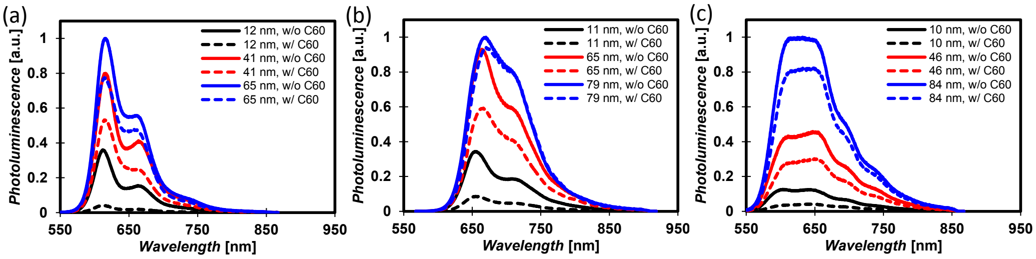

Figure 3.3. Steady state PL for (a) A, (b) B, and (c) C films with (dotted lines) and without (solid lines) a C_{60} (4 nm) quenching layer. All spectra were normalized by the maximum value in the thickest control (no C_{60}) film.

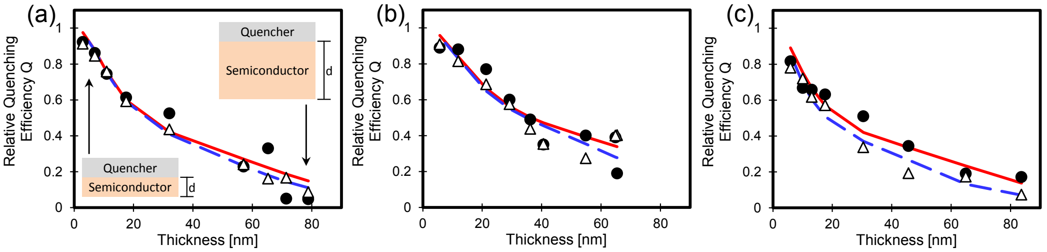

Figure 3.4. Relative quenching efficiency obtained from steady-state (filled circles) and time-resolved (open triangles) PL quenching measurements on bilayer films of (a) A, (b) B, and (c) C with a 4 nm C_{60} layer. A transfer matrix model was used to simulate the relative quenching efficiency for the steady-state (solid red line) and time-resolved (dashed blue line) measurements.

Figure 3.4 shows the relative quenching efficiency (filled circles) as a function of film thickness for bilayers of A (Figure 3.4a), B (Figure 3.4b), and C (Figure 3.4c) with C_{60} (4 nm). For thin films, the majority of generated excitons reach the quenching interface which results in a quenching efficiency that approaches unity. In contrast, only a small fraction of the generated excitons reach the quenching interface in thick films which yields a low quenching efficiency.

Table 3.1. Exciton lifetime for compounds A, B, and C measured in different laboratories.

Technique	A	B	C
SS-SQ & TR-SQ	1540 ± 20	2150 ± 60	2010 ± 20
EEA	1450 ± 100	1370 ± 20	1620 ± 20
BQ-MC & BQ-SV	1810 ± 60	2240 ± 40	1394 ± 10

[*] All lifetimes in picoseconds

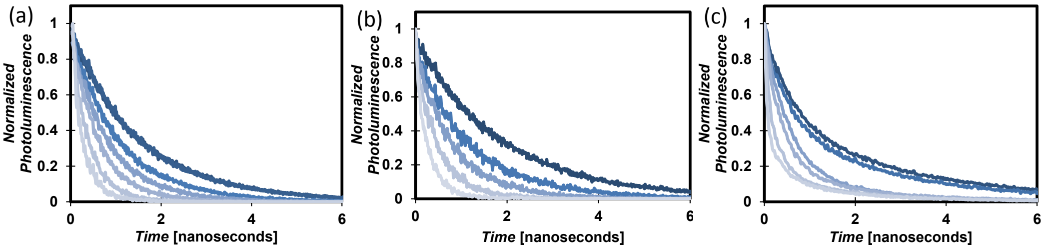

Figure 3.5. Time-resolved PL for bilayers of (a) A, (b) B, and (c) C with a C_{60} (4nm) quenching layer for decreasing thickness (dark to lighter curves). All decay curves were normalized by the value at time zero.

An alternative to using steady-state PL as in the SS-SQ technique is to measure with time-resolved PL as in the TR-SQ technique. Figure 3.5 shows the time-resolved PL for bilayers of A (Figure 3.5a), B (Figure 3.5b), and C (Figure 3.5c) with C_{60} (4 nm). It is important to note that the SS-SQ and TR-SQ techniques can be performed on the same set of fabricated bilayer films as was done in this work. The PL decay curves in Figure 3.5 show that the decay rate is accelerated as the film thickness is decreased. Fitted lifetimes for the pristine films measured in UCSB, St Andrews, and Groningen are summarized in Table 3.1.

The PL decay curves are normalized at the peak and integrated to determine the quenching efficiency:

$$Q = 1 - \frac{\int PL_{quencher}\, dt}{\int PL_{pristine}\, dt}, \tag{4}$$

where $\int PL_{quencher} dt$ and $\int PL_{pristine} dt$ are the integrated PL for the bilayer films with and without quencher. Figure 3.4 shows the relative quenching efficiency (open triangles) as a function of organic semiconductor thickness for bilayers of A (Figure 3.4a), B (Figure 3.4b), and C (Figure 3.4c) with 4 nm C_{60}. As expected, the quenching efficiency is nearly unity for thin films and approaches zero for thick films. In general, we see good agreement in quenching efficiencies between the SS-SQ and TR-SQ techniques. However, the TR-SQ technique is preferred since time-resolved measurements are less sensitive to the orientation of excitation and collection in comparison to steady-state measurements. To describe the generation, diffusion, and extinction of excitons, we use the following model:

$$\frac{\partial n(x,t)}{\partial t} = D\frac{\partial^2 n(x,t)}{\partial x^2} - \frac{n(x,t)}{\tau} + G(x,t), \tag{5}$$

where $n(x,t)$ is the exciton density at point x and time t, D is the exciton diffusion constant, τ is the exciton lifetime, d is the thickness of the active layer, and $G(x,t)$ is the exciton generation rate. Experimentally the laser is turned on only for a short period, of the order of a 200 picoseconds, while the diffusion process happens in a time scale of the order of nanoseconds and PL happens in even longer time scales, so we can write $G(x,t) = g(x)\delta(t - t_0)$ where δ is a delta-type function. We use the transfer matrix approach[44] to calculate $g(x)$.

Equation (5) must be supplemented with appropriate initial and boundary conditions. We assume that initially there are no excitons in the system, and therefore set $n(x,0) = 0$. When there is no quencher in the system we impose no-flux boundary conditions at both interfaces, i.e., $D\frac{\partial n(0,t)}{\partial x} = 0$ and $D\frac{\partial n(d,t)}{\partial x} = 0$. When a quencher is present on the interface located at $x = d$, we impose $D\frac{\partial n(0,t)}{\partial x} = 0$, and $n(d,t) = 0$. This last condition takes into account the charge transfer effect between the active layer and the quencher. In certain cases it has been shown[5] that energy transfer effect between the active layer and the quencher plays an important role, in which case Equation (5) is modified to

$$\frac{\partial n(x,t)}{\partial t} = D\frac{\partial^2 n(x,t)}{\partial x^2} - \frac{n(x,t)}{\tau} - k_F n(x,t) + G(x,t) \tag{6}$$

where $k_F = \frac{C_A \pi R_0^6}{\tau 6(d-x)^3}$ is the Förster energy transfer term with the energy acceptor molecular density $C_A \sim 1.4/\text{nm}^3$ for C60.[5]

Although Equations (5) and (6) can be solved explicitly in simple cases,[26] this is no longer possible when the Förster term is present. We therefore solve the equations numerically using finite differences. We have considered both equilibrium and time-integrated measurements of PL. For the equilibrium case, we simply set the time derivative equal to zero in Equations (5) and (6), which recovers the equations used for steady-state PL measurements.[26] For the time-integrated case, integrating in time over (0, ∞) in Equations (5) and (6) produces

$$D\frac{d^2 n(x)}{dx^2} - \frac{n(x)}{\tau} + G(x) = n(x,\infty) - n(x,0) = 0 \tag{7}$$

with boundary conditions $-D\frac{dn(x=0)}{dx} = 0$ and $D\frac{dn(x=d)}{dx} = 0$, and

$$\frac{d^2 n(x)}{dx^2} - \frac{n(x)}{\tau} + k_F n(x) + G(x) = 0 \tag{8}$$

with boundary conditions $-D\frac{dn(x=0)}{dx} = 0$ and $n(x=d) = 0$. Here $n(x) = \int_0^\infty n(x,t)dt$ and $G(x) = \int_0^\infty G(x,t)dt$. Note that steady-state Equations (7) and (8) are equivalent to time-dependent Equations (7) and (8). Therefore, instead of solving Equations (7) and (8), we solve Equations (7) and (8). In Equations (7) and (8), the exciton density is computed by time integration. Experimentally, the number of excitons is counted at each time step and then summed up over all times to produce the exciton density for comparison with Equations (7) and (8), instead of Equations (7) and (8). In this way, we can ensure the equivalence between the time-dependent study and the steady-state study. Using $L_D = \sqrt{D\tau}$, we rewrite Equations (7) and (8) as

$$L_D^2 \frac{d^2n(x)}{dx^2} - n(x) + G(x)\tau = 0 \tag{9}$$

And

$$L_D^2 \frac{d^2n(x)}{dx^2} - n(x) - \frac{C_A \pi R_0^6}{6(d-x)^3} n(x) + G(x)\tau = 0 \tag{10}$$

respectively.

The PL is then measured by $PL(d) = \int_0^d n(x)\varepsilon(x)dx$, where $\varepsilon(x)$ is the light extraction efficiency and is assumed to be a constant here. Denote PL of quenching and nonquenching cases by $PL_q(d)$ and $PL_n(d)$, respectively. The diffusion length L_D is then obtained by solving the following least-squares approximation:

$$\min_{L_D} \frac{1}{N} \sum_{i=1}^{N} \left(\frac{PL_q(d_i)}{PL_n(d_i)} - R(d_i) \right)^2 , \tag{11}$$

where N is the number of samples, and $R(d)$ is the ratio between PL of quenching and nonquenching cases measured in experiments. We solve the optimization problem (11) using Newton's method with a linesearch technique.[45] We use second order finite differences to solve Equations (7) and (8) with grid size $h = 0.1$ nm. Note that a rescaling of the generation term $G(x)$ in Equation (7) by a constant results in a rescaling of $n(x)$ by the same factor. This factor cancels out in the ratio of PL in Equation 9, which explains why the lifetime τ does not appear in Equation (9).

Surface quenching techniques are advantageous because the exciton diffusion length is directly measured. As discussed later, most other techniques first fit for the diffusion coefficient which is then used to determine the diffusion length. However, knowledge is the diffusion coefficient is also useful for the study of exciton dynamics. The diffusion coefficient can be determined from surface quenching techniques if the exciton lifetime, τ, of the pristine PL decay is measured. For the time-integrated case, the information of PL can be used to determine the exciton lifetime τ. We first integrate out x over (0, d) in Equation 5 with boundary conditions for the nonquenching case and get

$$\frac{dn(t)}{dt} = -\frac{n(t)}{\tau} + G(t), \tag{12}$$

where $n(t) = \int_0^d n(x,t)dx$ with initial condition $n(t=0) = 0$, and $G(t) = \int_0^d G(x,t)dx$ which is still a delta-type function. If $0 \le t < t_0$, then $n(t) = 0$. When $t > t_0, \frac{dn(t)}{dt} = -\frac{n(t)}{\tau}$ with solution $n(t) = n(t_0)e^{-\frac{t-t_0}{\tau}}$, whose decay rate is $-\frac{1}{\tau}$. The diffusion constant is then computed by $D = \frac{L_D^2}{\tau}$.

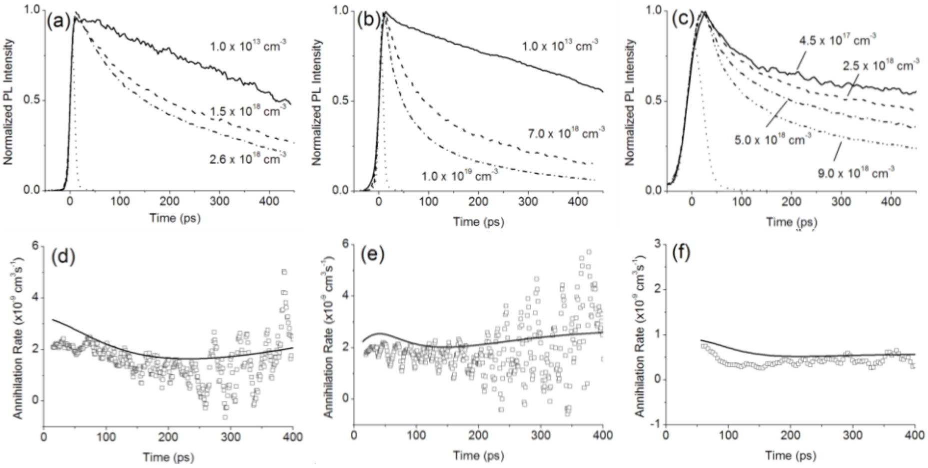

Figure 3.6 Photoluminescence decays at different excitation densities and time dependence of the annihilation rate measured in films of A (a,d), B (b,e) and C (c,f). Dotted lines on the left panel are the instrument response functions (IRF) for the decays shown. Solid lines on the right panel are the annihilation rates obtained from the deconvoluted fits to the PL decays. Apparent oscillations of annihilation rate at early time are a result of smoothing which was applied to PL kinetics before their differentiation.

3.4 Exciton-Exciton Annihilation

Measurements of exciton diffusion can be done by studying exciton-exciton annihilation (EEA). At high enough excitation densities a pair of excitons can interact with each other and annihilate within their lifetime. This process leads to a loss of excitons at a rate which depends on the excitation intensity and the diffusivity of the excitons. The EEA technique is advantageous because a secondary quencher material is not needed which greatly simplifies fabrication and modeling. The EEA technique assumes efficient exciton-exciton annihilation. This technique also approximates the annihilation radius from the density as discussed later.

The sample fabrication procedure involved first making solutions in chloroform and stirring them overnight at 50°C. Films were then spin-coated on fused silica substrates which had previously been cleaned via ultra-sonication with acetone and isopropanol for 15 minutes each followed by drying with a N_2 gun. A 1 mL syringe was used with a 0.1 μm PTFE filter to spin-coat the films. Spin-coating was done in the nitrogen glovebox using spin speeds of 1500 – 2000 rpm for duration of 60 seconds typically. No heat treatment was performed on these films and measurements performed on the same day the films were spin-coated. Film samples were transferred to the sample chamber and sealed within the glovebox.

Exciton-exciton annihilation measurements were performed using 100 fs laser pulses at a repetition rate of 5 kHz for excitation and a Hamamatsu C6860 synchroscan streak camera for detection. Samples were kept in the nitrogen atmosphere during measurements. The energy of the laser pulses was controlled with neutral density filters. The excitation spot was measured with a LaserCam 3D beam profiler and found to be an ellipse with the major and minor diameters of 290 μm and 215 μm. Measurements using different excitation wavelengths (400 nm and 570 nm) gave very similar annihilation rates. PL decays at low excitation density were measured using 100 fs pulses at 400 nm with the 80 MHz repetition rate. Figure 3.6 shows the intensity-dependence of time-resolved fluorescence of compound A, B, and C.

Film thicknesses were estimated using ellipsometry measurements. Spectroscopic ellipsometry measurements were performed in air over a wavelength region 190 - 1700 nm with a J. A. Woollam Co. Inc. M-2000DI ellipsometer. Normal incidence was used for transmission measurements whereas for reflection measurements the incidence angle was varied between 15° and 45° to the normal. To model the optical constants *n* (refractive index) and *κ* (extinction coefficient) and the thickness *d*, an isotropic optical model was assumed. The optical constants were first modeled in the transparent region above 750 nm where $\kappa = 0$ and was fitted using the Cauchy Equation. The data in the transparent region was then fitted to solely in terms of the refractive index and the thickness to give a unique solution. To obtain the optical constants for the full spectral range, the film thickness was fixed and *n* and *κ* were selected as fitting parameters. Backside reflections were supressed by applying scotch tape to the back of substrates.

In order to extract quantitative parameters from the measured fluorescence decays (Figure 3.6), the following analysis is used. In the absence of exciton-exciton annihilation the exciton density N_1 which is proportional to the time-resolved PL intensity can be described by a rate Equation

$$\frac{dN_1}{dt} = -kN_1 \tag{13}$$

where k is a linear decay rate. When annihilation is present, the exciton density N_2 is described by

$$\frac{dN_2}{dt} = -kN_2 - \gamma N_2^{\ 2} \tag{14}$$

where γ is the annihilation rate. By combining Equation 13 and Equation 14 we get

$$\gamma = \frac{1}{N_2}\left\{\frac{dN_1/dt}{N_1} - \frac{dN_2/dt}{N_2}\right\} \tag{15}$$

This approach to data analysis is similar to the one described by Gulbinas et al[46] except that we use the fluorescence decay at a very low excitation density as a reference. Figure 3.6d-f shows γ calculated using Equation 15 which was averaged over several decays with different excitation densities. The PL decay at low intensity was fitted with a bi-exponential decay function to reduce the noise and smoothing was applied to differentiation of the PL decays at high intensities. We also used deconvoluted fits to a 3-exponential decay function to calculate γ. The deconvoluted fits give more accurate representation of the fast decays at high intensity and provide more precise scaling of the PL intensity with exciton density, therefore we consider γ values from the deconvoluted fits more accurate. We observe a decrease of the γ value from its initial value in the first 100 ps in all three materials. Time-dependent γ can be observed due to several causes. One possible cause is very slow exciton diffusion, in that case exciton-exciton annihilation could only occur by direct Förster energy transfer onto an excited chromophore which is called static annihilation.[47] Another possible cause is exciton diffusion being restricted to one dimension. In a simplified picture, time-dependence in both static annihilation and restricted diffusion can be explained by fast annihilation of the nearest distance excitons and much slower annihilation of excitons which are further apart. In both cases, it would show $\gamma(t) = \gamma_0/\sqrt{t}$ dependence.[7,15,17,46,47] We can discount both these processes because the time dependence in Figure 3.6 is much weaker than $\gamma_0/\sqrt{t}$ dependence. We explain it by time dependence of exciton diffusion which in disordered materials is expected to slow down with time because the spectral overlap between fluorescence and absorption reduces as excitons progressively populate lower energy sites until a thermal equilibrium is reached. On a time scale $t > 100$ ps the time-independent annihilation rate is observed. A similar behaviour has been observed in earlier studies of singlet[7,15,17,46–49] or triplet exciton[50,51] diffusion in organic semiconductors. In order to estimate the diffusion coefficient D in thermal equilibrium we use γ values at $t > 100$ ps and the Smoluchowski Equation

$$\gamma(t) = 4\pi R_a D\left(1 + \frac{R_a}{\sqrt{2\pi D t}}\right) \tag{16}$$

where R_a is the annihilation radius. The time-dependent term is negligible after 5 ps. Equation (16) is strictly valid only for isotropic exciton diffusion and isotropic exciton-exciton interactions. We find that films A, B, and C are predominantly isotropic (see Section 3.9). In semi-crystalline materials both can be anisotropic, however, in case of preferentially one-dimensional diffusion and interaction the annihilation rate has a similar expression to Equation (16) but D in this case is an effective diffusion coefficient.[16] We assume that dissociation of higher energy excitons into electron-hole pairs is negligible because we do not see any additional fluorescence quenching by generated charges and also because measurements using different excitation wavelengths (400 nm and 570 nm) gave very similar annihilation rates (charge generation yield would be higher at shorter excitation wavelength). The annihilation radius is difficult to determine experimentally. For our calculation of the diffusion coefficients we used the average intermolecular spacing as the R_a value assuming that molecules are positioned in a simple cubic lattice. The results are shown in Table 3.2 including a one-dimensional diffusion length which is calculated using $L_D = \sqrt{D\tau}$ where τ is the fluorescence lifetime which in case of non-exponential decay is taken as the weighted average of time constants and pre-exponential factors obtained from the bi-exponential fit.

Table 3.2. Material properties of pristine films of compounds A, B and C with experimentally measured values of fluorescence lifetimes τ and annihilation rates γ and calculated values of the diffusion coefficients D and one-dimensional exciton diffusion lengths L_{1D}.

Material	ρ [gcm^{-3}]	Ra [nm]	γ [$\times 10^{-9}$ cm^{3}s^{-1}]	D [$\times 10^{-3}$ cm^{2}s^{-1}]	τ [ps]	L_{1D} [nm]
A	1.175	1.0	1.9 ± 0.6	1.5 ± 0.4	1450 ± 100	14.5 ± 2.2
B	1.221	1.1	2.1 ± 0.6	1.5 ± 0.4	1370 ± 20	14.5 ± 2.2
C	1.234	1.1	0.6 ± 0.2	0.4 ± 0.1	1620 ± 20	8.4 ± 1.3

Relative to other techniques, the EEA method yielded a greater exciton diffusion coefficient for compounds A and B but a similar value for compound C. As shown in Figure 3, molecular ordering in films of compounds A and B is greater than in films of compound C. This observation suggests that the efficiency of the exciton-exciton annihilation is higher in more ordered materials. This can be explained by the fact that excitons diffuse from amorphous to crystalline regions where they have lower energy. Exciton-exciton annihilation is therefore more likely to occur in crystalline regions where exciton diffusion is enhanced. In other bulk quenching techniques – such as BQ-MC and BQ-SV – exciton quenching is probed in both amorphous and crystalline region which may explain the lower diffusion coefficients relative to EEA. From this, it is expected that amorphous compounds such as compound C would yield similar diffusion coefficients for EEA and other bulk quenching techniques. Indeed, EEA and other bulk quenching methods yielded a similar diffusion coefficient around 0.4 × 10^{-3} cm^2/s for compound C.

3.5 Time Resolved Photoluminescence Bulk Quenching Analyzed with Monte Carlo Simulation Software

The challenge when employing the SS-SQ and TR-SQ techniques is the non-trivial fabrication of bilayer films which have a sharp interface and a high quenching efficiency. An alternative technique which does not require bilayer films is time-resolved PL bulk quenching modeled with a Monte Carlo simulation (BQ-MC). Film fabrication for the BQ-MC technique is relatively simple as it involves spin coating blend solutions of the organic semiconductor with increasingly greater concentrations of PCBM. The BQ-MC technique can be performed with as little as eight films. BQ-MC probes the micromorphology of the blend to make sure that PCBM mixes homogeneously with the organic semiconductor. As will be shown later, PCBM may tend to cluster at higher concentrations. BQ-MC is described in detail in [Mikhnenko Enegy & Env. Sci.] and the simulation is available for free at http://mikhnenko.com/eDiffusion.[13]

In regards to film fabrication, all solutions were stirred and heated overnight at 60 °C. Films were prepared by spin casting at 700 rpm for 60 seconds onto 3 cm × 3 cm (Corning) substrates in a glove box. Blend solutions were prepared by subsequent additions of the 1 mg/mL PCBM to the 5 mg/mL organic semiconductor solution. To prevent photodegradation, all films were encapsulated in an equivalent manner as discussed in the SS-SQ and TR-SQ section above.

PL measurements were performed by exciting samples at 380 nm with frequency doubled 100 fs laser pulses from a Ti-sapphire laser. Time-resolved PL was measured with a Hamamatsu streak camera. Measured decay curves were normalized by the value at time zero and fitted to a single exponential decay. Fitted decay curves were integrated in order to calculate the quenching efficiency Q:

$$Q = 1 - \frac{\int PL_{blend}\, dt}{\int PL_{pristine}\, dt} \tag{17}$$

where $\int PL_{blend}dt$ and $\int PL_{pristine}dt$ are the integrated time-resolved PL for the blend and pristine organic semiconductor films respectively. The PL decays were normalized to the value at t=0 prior to the integration. Figure 3.7 shows the time-resolved PL for A (Figure 3.7a), B (Figure 3.7b), and C (Figure 3.7c) blended with varying concentrations of PCBM. The PL decay rate increases for greater PCBM volume fractions. Using Equation 15, the relative quenching efficiency was calculated for blend films as shown in Figure 3.8. To determine the exciton lifetime, the PL decay curves for the pristine films were fitted to a single exponential decay. Pristine films lifetimes are summarized in Table 3.1.

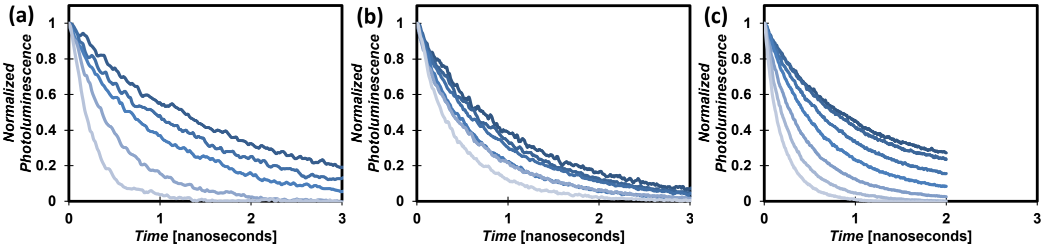

Figure 3.7. Time-resolved PL for blend films of (a) A, (b) B, and (c) C with a C_{60} (4 nm) quenching layer for decreasing thickness (dark to lighter curves). All decay curves were normalized by the value at time zero.

Analysis with the BQ-MC technique involves inputting the pristine film lifetime and experimentally measured quenching efficiencies into a Monte Carlos simulation[13] which fits for the diffusion coefficient. In Figure 3.8, the experimentally measured relative quenching efficiencies (open circles) are fitted (red line) with the Monte Carlo simulation. At high PCBM volume fractions the experimentally measured relative quenching efficiencies for A, B, and C begin to taper off from the simulated curve. This has been observed in other systems[12,13] and is likely due to clustering of PCBM molecules at higher concentrations which reduces the effective quenching volume and therefore the total quenching efficiency. This effect can also arise when the lifetime of excitons in the films approaches the instrument response function (IRF) which would artificially extend the measured lifetime thereby reducing the quenching efficiency.

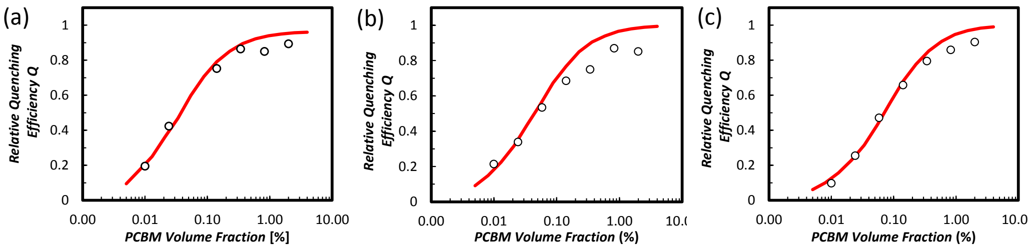

Figure 3.8. Time-resolved PL quenching on blend films. Relative quenching efficiency as a function of PCBM volume fraction for (a) A, (b) B, and (c) C blends. Measured data (black dots) were simulated (red line) with a Monte Carlo program.

3.6 Time-Resolved Photoluminescence Bulk Quenching Analysed with Stern-Volmer Equation

For materials that exhibit mono-exponential decay, the Stern-Volmer analysis can be applied instead of Monte Carlo simulation. The advantage of the BQ-SV technique is that modeling software is not needed since the diffusion coefficient determined by a simple fit to the Stern-Volmer Equation. The BQ-SV technique assumes single exponential decay and a 1 nm center to center distance for the exciton and organic semiconductor.

In the BQ-SV technique, the measured PL decay from pristine and blend films are fitted to a single exponential to obtain the lifetime for the pristine and blend films. The fitted lifetimes are then used to plot inverse lifetime versus PCBM concentration which is then fitted with the Stern-Volmer Equation:[52]

$$\frac{1}{\tau} = \frac{1}{\tau_f} + 4\pi r D c, \tag{18}$$

where τ_f is the lifetime of the pristine film, τ is the lifetime of the blend film, r is the sum of the exciton and PCBM radii, D is the diffusion coefficient, and c is the concentration of PCBM. The r value is the center to center distance between the exciton and PCBM which is approximated at 1 nm. The exciton diffusion length is obtained by inputting the fitted diffusion coefficient and the pristine film lifetime into Equation 18.

Knupfer et al. showed that the gap exciton extension or exciton size scales linearly with the molecular size for π-conjugated molecules.[53] In general, the exciton size was found to be roughly 0.5 nm smaller than the molecular size. For compounds A, B, and C the conjugated backbone is roughly 2-2.7 nm. Following the trends observed by Knupfer et al., we expect an exciton size of 1.5-1.7 nm and a radius of 0.75- 0.88 nm. Given that the PCBM radius is roughly 0.5 nm, the center to center distance, r, between the exciton and PCBM is roughly 1.25-1.33nm. It should be noted a r between 1.25-1.33 nm is an upper limit since it is the center to center distance when the conjugated backbone is normal to the PCBM sphere. A lower r is expected when the conjugated backbone and PCBM are face-on. We therefore believe that 1 nm is a reasonable approximation for r.

In Figure 3.9, the inverse lifetimes for A (black circles), B (red squares), and C (blue triangle) blend films are plotted against PCBM concentration and subsequently fitted for the diffusion coefficient using Equation 16 in the linear regime. Figure 3.9 shows that the

Stern-Volmer Equation fits well at the low PCBM concentration but deviates at PCBM concentrations above 60 × 10^{17} m^{-3}. The observed deviations are likely due to the inability to form a homogenous distribution of PCBM molecules at higher concentrations. The diffusion coefficient and exciton diffusion length obtained with the BQ-SV technique is summarized in Table 3.5 and Figure 3.15.

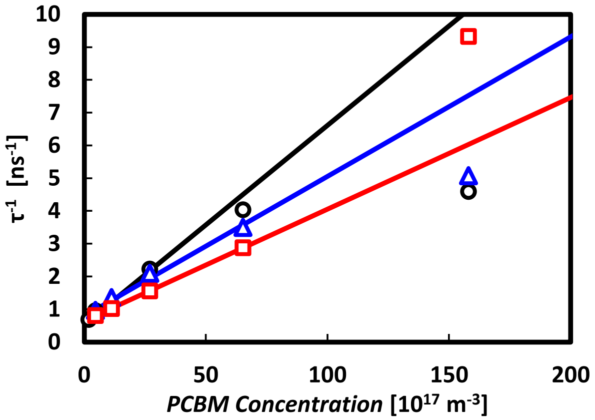

Figure 3.9. Time-resolved PL quenching on blend films. Inverse lifetime as a function of PCBM concentration for A (black circles), B (red squares), and C (blue triangles) blends. Measured data (markers) were fitted (lines) Stern-Volmer Equation.

The BQ-SV technique is useful when access to simulation software is not possible. It should be noted here that this technique is only valid for monoexponential decay. In contrast, the BQ-MC technique can be performed with first, second, or third order exponential decay which makes the BQ-MC technique applicable to a larger set of materials.

3.7 Exciton Diffusion Length From FRET Theory

Exciton diffusion in π-conjugated polymers occurs via a hopping mechanism mediated by Förster resonant energy transfer (FRET). The exciton diffusion coefficient can thus be calculated from the spectral overlap of absorption and emission of the chromophores. In this technique the largest deviation arises from the approximation of the intermolecular distance as will be discussed later.

According to the Einstein-Smoluchowski theory of random walks, the diffusion coefficient in a 3D system can be expressed as[32]

$$D = \frac{R^2}{6\tau_{hop}} \tag{19}$$

where R is the inter-chromophore distance, and τ_{hop} is the exciton hopping time. From FRET theory

$$\tau_{hop} = \tau\left(\frac{R}{R_0}\right)^6 \tag{20}$$

where τ is the fluorescence lifetime in film and R_0 is the Förster radius which was calculated from the extinction coefficient and PL spectra shown in Figure 3.10. For our calculations, the closest intermolecular distance estimated from Kim et al[42] is taken as the inter-chromophore distance R.

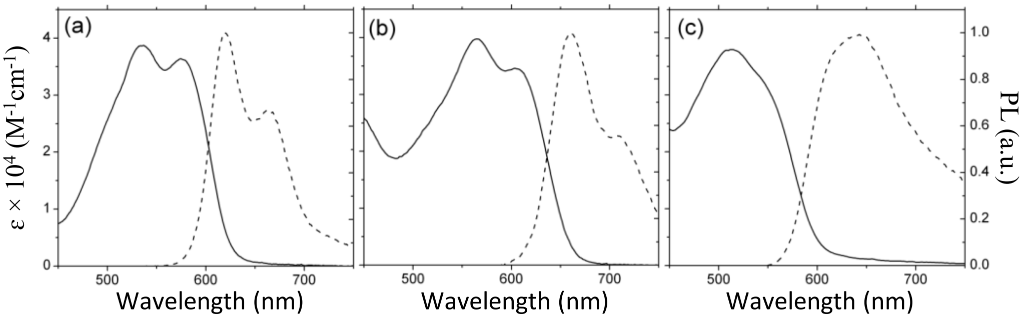

Figure 3.10. Molar extinction coefficient obtained using spectral ellipsometry and normalized PL spectra of films spin-coated on fused silica substrates for compounds (a) A, (b) B and (c) C.

The Förster radius R_0 is calculated from the spectral overlap using:

$$R_0{}^6 = \frac{9000(\ln 10)k^2 Q_Y}{128\pi^5 N_A n^4} \int_0^\infty F(\lambda)\varepsilon(\lambda)\lambda^4 d\lambda, \tag{21}$$

where k^2 is the relative orientation of dipoles (k^2 = 0.476 assuming rigid and randomly oriented dipoles), Q_y is the PLQY in film, n is the average refractive index of the medium in the wavelength range at which spectral overlap is significant, $F(\lambda)$ is the corrected fluorescence intensity of the film with area normalized to unity and $\varepsilon(\lambda)$ is the molar extinction coefficient in film that was obtained using spectral ellipsometry as described below. It should be noted that a number of works have incorrectly used a k^2 = 2/3. A k^2 = 2/3 is derived from energy transfer that occurs after the donor and acceptor molecules go through randomized rotation diffusion.[52] This is unlikely the case for solid state films which have rigid and randomly oriented dipoles. For rigid and randomly oriented dipoles a k^2 = 0.476 is more appropriate.[54] Molar extinction coefficient (in $M^{-1}cm^{-1}$) is given by

$$\varepsilon = \frac{A}{cl}, \tag{22}$$

where A is the absorbance, l is the optical path length and c is the molar chromophore concentration, which is

$$c = 1000\frac{\rho}{M_c}, \tag{23}$$

where ρ is the density of the single crystal obtained previously[42] and M_c is the molecular weight of a chromophore. Absorbance is related to the absorption coefficient α via $A = \alpha l \log_{10} e$ whereby the absorption coefficient is related to the optical constant κ (imaginary part of the refractive index) via $\alpha = \frac{4\pi\kappa}{\lambda}$.

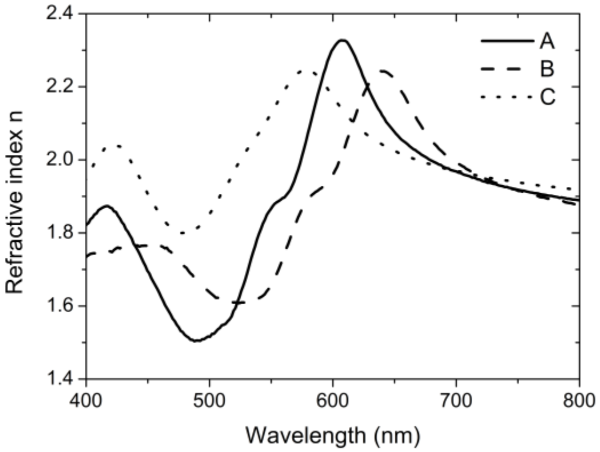

Figure 3.11. Refractive indices in the visible region obtained from ellipsometry

These molar extinction coefficients obtained agree well with published values for these materials in solution.[42] To calculate the diffusion coefficients, an intermolecular distance *R* is assumed. Here, we used the shortest intermolecular distances obtained from x-ray diffraction studies[42] of single crystals to calculate the upper limit of the diffusion coefficient. The lower limit of the diffusion coefficient is estimated by using the average intermolecular distances assuming they are positioned in a simple cubic lattice. This gives a range of values of the diffusion coefficients from a single crystal approximation to an average intermolecular spacing. Table 3.3 below shows the main values used to calculate the upper and lower limits of diffusion coefficient using these FRET calculations. The film PLQY were all measured in air and the decay lifetimes were measured under nitrogen. Film PLQY's were typically measured not long after performing annihilation measurements and were exposed to air for less than a few minutes before running the PLQY measurement.

Ellipsometry measurements (see Section 3.9) were performed on these films which allowed the refractive indices to be obtained by modelling of the optical constants as shown in Figure 3.11.

Table 3.3. Calculating upper and lower limits of diffusion coefficients using FRET

Material	PLQY	τ [ns]	Refractive index, n	R_0 [nm]	R [nm]		D [$\times 10^{-3}$ cm^{2}s^{-1}]		
					Min.	Max.	Min.	Max.	Avg.
A	0.48	1.45	2.32	2.80	0.74	1.04	0.48	2.6	1.53
B	0.14	1.37	2.23	2.35	0.71	1.09	0.15	1.1	0.64
C	0.28	1.62	2.23	2.32	0.91	1.11	0.11	0.33	0.22

3.8 Measurement of Anisotropy and Relative Crystallinity with X-ray Diffraction

Using a Rigaku Smartlab High-Resolution X-ray Diffractometer, the scattering for the out of plane direction was probed by performing a θ-2θ scan from 2-30^0 with 1.5418 Å CuKα radiation at 40 kV operating voltage and 44 mA operating current. Figure 3.12 shows the out of plane scattering for films of A, B, and C. Films of A and B exhibited a scattering peak at q_z 1.3 and 1.1 nm^{-1} respectively. Using X-ray diffraction from single crystals, the scattering peaks at q_z values of 1.3 and 1.1 nm^{-1} for films A and B are indexed as the (100) plane. No scattering was detected in films of C (dashed green line in Figure 3.12). In order to quantitatively compare A and B the measured scattering intensity must be corrected for crystallites texturing, thickness, reflection structure factor and multiplicity, unit cell volume, and the Lorenz-Polarization factor.

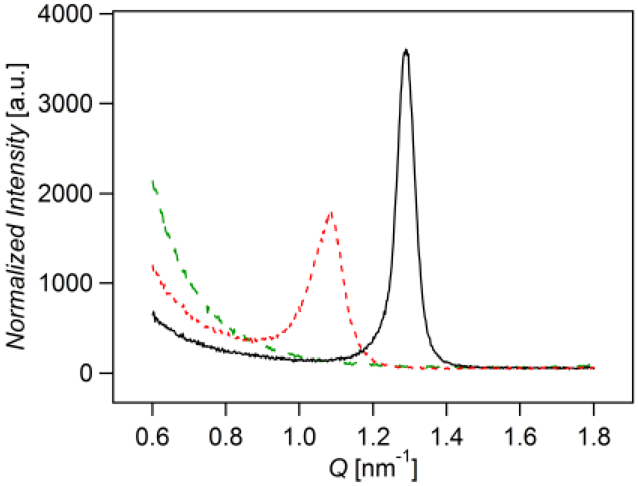

Figure 3.12. Out of plane X-ray diffraction scattering of films A (solid black line), B (dashed red line), and C (dashed green line).

To probe crystallite texturing in films of A and B a pole figure was created by measuring the scattering intensity form the (100) plane of A and B as a function of Chi (the polar angle).This was done by fixing q_z at 1.3 (1.1) nm^{-1} and scanning from Chi values of -5^0 to 90^0 (Figure 3.13). Figure 3.13 shows that films of A and B exhibit a strong peak intensity at Chi = 0˚. This result indicates that crystallites in films of A and B are preferentially oriented with the (100) plane parallel to the substrate and textured in the out of plane direction.

Table 3.4. Normalization Parameters for X-Ray Diffraction

	A	B	C
Thickness (nm)	106	113	83
Structure Factor	140.91	172.19	209.91
Multiplicity	2	2	2
Unit Cell Volume (Å^3)	2229.9	2563.6	5431.8

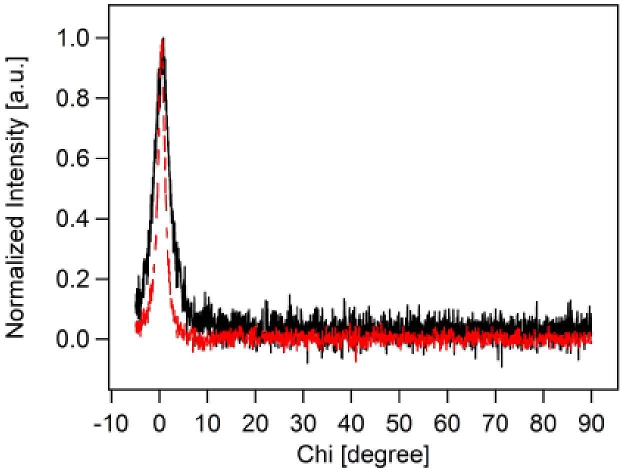

Figure 3.13. Pole figure for films of A (black line) and B (red dashed line). The scattering intensity was collected at 4.8 and 5.6 2θ for films of A and B respectively which corresponds to the diffraction from the (100) plane.

Since the crystallites in films A and B are predominantly textured in the out of plane direction, it is possible to determine the relative crystallinity of films A and B with proper normalization of the out of plane scattering observed in Figure 3.12. Figure 3 shows the out of plane scattering for films A and B which has been normalized by the thickness, structure factor, multiplicity, unit cell volume, and the Lorenz-Polarization factor (Table 3.4).[55] The structure factor, multiplicity and unit cell volume were obtained from the single crystal structures.[42] The integrated scattering intensity from A is roughly 1.6 times greater than B. This result indicates that films of A have a greater volume of crystalline material relative to films of B. In summary, we find that the relative crystallinity follows A > B > C. It is important to note that X-ray diffraction experiments do not tell what percentage of film volume is crystalline as compared to amorphous volume.

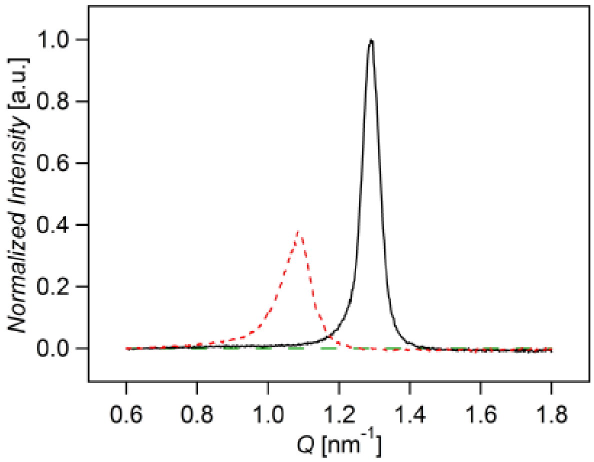

Figure 3.14. X-ray diffraction for films of A (solid black line), B (dotted red line), and C (dashed green line). Scattering intensity was normalized by film thickness, structure factor, multiplicity, unit cell volume, and the Lorenz-Polarization.

3.9 Measuring Anisotropy in Bulk Film with Spectroscopic Ellipsometry

Anisotropy can impact the directionality and efficiency of exciton diffusion. It can also result in a difference in exciton diffusion length for techniques which measure exciton diffusion length normal to the substrate in comparison to techniques which measure exciton diffusion in 3D. For this reason, it is important to investigate the degree of anisotropy in films of A, B, and C. Figure 3.11 showed that crystallites in films A and B are highly textured out of plane and therefore anisotropic. While our x-ray diffraction measurements confirm the presence of anisotropy, it does not quantify degree of anisotropy since the volume fraction of amorphous and crystalline regions is not known. It would be ideal to probe the bulk film anisotropy. A number of studies have shown that spectroscopic ellipsometry is a useful technique to measure bulk film anisotropy since both amorphous and crystalline regions are probed.[56–58] Spectroscopic ellipsometry can be used to model the magnitude of absorption for both the in and out of plane directions. For a highly anisotropic film, molecules and their transition dipoles are preferentially oriented in a specific direction. This preferential orientation induces a difference in absorption for the in and out of plane directions which is correlated to the degree of anisotropy.

It is useful to first discuss the expected in and out of plane absorption of our films if they were highly crystalline and anisotropic. Figure 3.13 showed that crystallites in films of A and B are preferentially oriented with the (100) plane parallel to the substrate. When the (100) plane is parallel to the substrate, molecules of A and B have their conjugated backbone nearly parallel to the substrate as determined form the single crystal structures.[42] Density function theory calculations showed that the transition dipole lies along the conjugated backbone for molecules A, B, and C. It is therefore expected that a highly anisotropic film of A or B would strongly absorb electrical fields which are also parallel to the substrate. Since the electrical field is perpendicular to the direction of the propagation vector, we would expect a strong absorption for light incident perpendicular to the substrate. The magnitude of absorption can be quantified by modeling the extinction coefficient, *k*, or the imaginary component of the dialectic constant, *e2*. By convention, a subscript is added to identify the direction of the electrical field that gives rise to the absorption. Previous works have denoted absorption from electrical fields parallel to the substrate as $e2_{in\text{-}plane}$, $e2_x$, or $e2_{ordinary}$.[56–58] Likewise, absorption from electrical field perpendicular to the substrate has been referred to as $e2_{out\text{-}plane}$, $e2_z$, or $e2_{extraordinary}$. If films of A(B) are highly anisotropic, then we would expect the magnitude of $e2_{in\text{-}plane}$ to be significantly greater than that of $e2_{out\text{-}plane}$.

To probe anisotropy, films of A, B, and C where prepared at three different thicknesses spanning 20 - 100 nm by varying the concentration. All films where spin casted from chloroform at 2000 rpm for 60 seconds. Spectroscopic ellipsometry was measured on films of A, B, and C as described in Section 3.9. Additionally, the thickness and RMS roughness where measured with profilometer and atomic force microscopy in order to reduce the number of fit parameters in optical modeling. Multiple quartz substrates where initially modeled with a Cauchy model to determine the substrate optical constants. Optical constants for A, B, and C were fit with a B-Spline model[59] and the anisotropy type set to Biaxial. Kramers-Kronig Mode, Difference Mode, and force *e2* positive was turned on for fitting. Fit parameters included the in and out of plane dielectric constant along with the anisotropy parameter dZ_A. Fitting was done with individual samples along with multi-sample analysis. Similar results were obtained for individual and multi-sample analysis. Figure 3.15 shows *e2* obtained from the multisampling fits of films A, B, and C. For all three compounds, $e2_{in\text{-}plane}$ is only slightly greater than $e2_{out\text{-}plane}$. As discussed above, we would expect $e2_{in\text{-}plane}$ to be significantly greater than $e2_{out\text{-}plane}$ if films of A and B were highly anisotropic. The similar magnitudes of $e2_{in\text{-}plane}$ and $e2_{out\text{-}plane}$ suggest that the majority of molecules in films of A, B, and C have isotropic orientation. Interestingly, our x-ray diffraction studies showed that there exist crystallites in films of A and B with anisotropic orientation. It is likely that the volume fraction of anisotropic crystal is small due to the fact that all films where prepared from a low boiling point solvent and a relatively high spin speed, which would promote the formation of isotropic films.

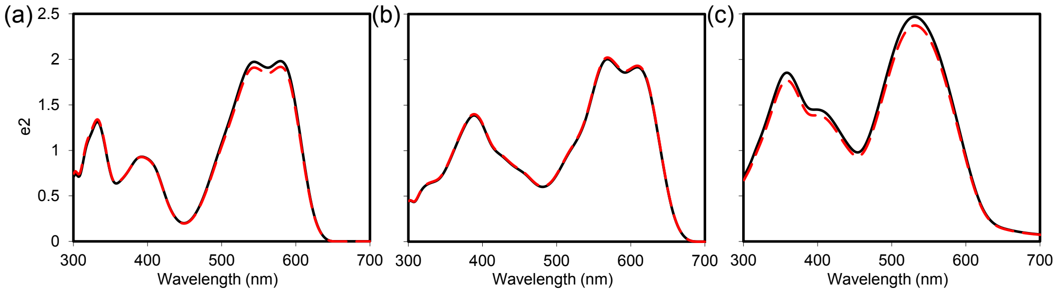

Figure 3.15. Modeled $e2_{in\text{-}plane}$ (black line) and $e2_{out\text{-}plane}$ (dashed red line) for films of (a) A, (b) B, and (c) C.

3.10 Discussion

Table 3.5 summarizes the sample preparation, measurement, and analysis in the techniques employed in this work. In regards to sample preparation, surface quenching techniques are the most time consuming due to high demands for the sample quality. An efficient exciton quencher is required that can form a stable and sharp interface with the organic semiconductor, which is non-trivial as discussed in the Supplementary Information. Relatively large number of samples is required (10-20) with variable thickness of organic semiconductor in the range of typically 5-50 nm. In addition a precise thickness measurement is necessary using atomic force microscopy and/or spectroscopic ellipsometry. Surface quenching techniques also assume consistent morphologies across thick and thin films. This is likely not the case for semi-crystalline materials. Samples for the bulk quenching techniques – such as BQ-MC and BQ-SV – are relatively simple to prepare since the aforementioned requirements for the film thickness, surface roughness, and interface effects do not apply. However, a good quenching agent must be available, which would homogeneously mix with the organic semiconductor. Fortunately, [6,6]-phenyl-C_{61}-butyric acid methyl ester (PCBM) can be used as such an agent in most of the cases. The bulk quenching techniques require a smaller number of samples, typically only 8 spin-coated films. These methods account for clustering of the quenchers and cannot be used if the miscibility with the quenching agent is poor. And finally, the EEA and FRET theory techniques have the simplest fabrication procedures since all measurements are done on a pristine film.

Table 3.5. Sample preparation, measurement, and data analysis for various techniques to measure exciton diffusion length.

Technique	Abbrev	Sample Preparation	Measurement	Data Analysis	Best For
Steady-state surface quenching	SS-SQ	• 10 pristine films with varying organic semiconductor thickness • 10 bilayer films with a quenching layer and varying organic semiconductor thickness.	•Steady-state PL spectrum as a function of thickness •Thickness •Optical constants	• Calculate quenching efficiency • Model optical constants, electrical field, generation rate, and exciton density • Fit for exciton diffusion length	•Amorphous smooth films. Good quenching interface is required
Time-resolved surface quenching	TR-SQ	• Equivalent to SS-SQ	•Time-resolved PL decay as a function of thickness. •Thickness •Optical constants	• Equivalent to SS-SQ	•Equivalent to SS-SQ
Exciton-exciton annihilation	EEA	• 3-5 pristine films	•Time-resolved PL at different excitation densities •Film density •Thickness	• PL decay fitting with an analytical model	•Amorphous materials
Bulk quenching with Monte Carlo modeling	BQ-MC	• 8-10 blend films with varying concentrations of quencher.	•Time-resolved PL decay •Film density	• Calculate quenching efficiency • Use model PL Monte Carlo simulation to	•Moderately crystalline or amorphous materials
Bulk quenching with Stern-Volmer modeling	BQ-SV	• Equivalent to BQ-SV	•Equivalent to BQ-SV	• Calculate quenching efficiency • Use analytical model to fit the data	•Equivalent to BQ-SV
FRET theory		• 3-5 pristine films	•Steady-state absorption and PL spectrum •PL quantum yield •Film Density •Thickness •Index of refraction	• Estimate distance between molecules • Calculate Förster Radius and diffusion coefficient	•Materials with very small quantities available

When it comes to the experimental measurements, the steady-state techniques – such as SS-SQ – are the most challenging because they require careful estimation of the amount of light absorbed and emitted.[5] Therefore, the time-resolved techniques – such as TR-SQ, BQ-MC, BQ-SV, and EEA – are preferred over the steady-state measurements. However, the time-resolved techniques usually require expensive equipment, such as ultra-fast pulsed lasers and sophisticated detectors. Thickness measurements with very high precision must be conducted for surface quenching methods that is time and resource consuming. The EEA technique requires high intensities of the pulsed lasers and good photostability of a material under study.

Table 3.6 and Figure 3.16 summarize the measurements of the exciton diffusion coefficient and exciton diffusion length. Very good agreement between different techniques is obtained in the compound C, whereas in compounds A and B the technique based on exciton-exciton annihilation gives a higher exciton diffusion coefficient than the techniques based on the bulk quenching and surface quenching.

Table 3.6 Exciton diffusion lengths for compounds A, B, and C measured with different techniques.

Technique	Diffusion Coefficient × 10^{-3} (cm^2s^{-1})			Exciton Diffusion Length (nm)		
	A	B	C	A	B	C
SS-SQ	1.13 ± 0.1	0.4 ± 0.07	0.36 ± 0.04	13.2 ± 0.1	9.32 ± 0.3	8.49 ± 0.16
TR-SQ	1.06 ± 0.18	0.6 ± 0.1	0.27 ± 0.03	12.7 ± 1.1	9.3 ± 0.3	7.22 ± 0.36
EEA	1.5 ± 0.4	1.5 ± 0.4	0.4 ± 0.1	14.5 ± 2.2	14.5 ± 2.2	8.4 ± 1.3
BQ-MC	0.94 ± 0.27	0.39 ± 0.13	0.4 ± 0.06	12.9 ± 1.9	9.2 ± 1.5	7.4 ± 0.6
BQ-SV	0.9 ± 0.14	0.27 ± 0.02	0.34 ± 0.02	11.4 ± 1.8	7.79 ± 0.04	6.9 ± 0.3
FRET Theory	1.53 ± 0.97	0.64 ± 0.45	0.22 ± 0.12	13.8 ± 4.7	8.5 ± 3.6	5.8 ± 1.2

The data analysis procedure for the different techniques studied here range from advanced modeling and simulation to relatively simple fitting to an equation. The data modeling for the surface quenching techniques can be either simple or extensive, depending on the materials. The most complex situation occurs in the bi-layer method if the organic semiconductor and the exciton quencher have both significantly different refractive indexes and strong Förster coupling (see Section 3.7). Otherwise, the exciton diffusion can be modeled with a simple analytical formula.[4] The data of the EEA technique can be modeled using an analytical model; however, the annihilation radius has to be determined using additional experiments.[7] Modeling for the bulk quenching techniques – such as BQ-MC – is not straightforward in general. However, a free software package is available for use [http://mikhnenko.com/eDiffusion]. If the bulk quenching data shows mono-exponential PL decay then analysis can be readily performed by fitting to the Stern-Volmer Equation as in the BQ-SV method. Finally, FRET theory provides a relatively easy way to estimate the exciton diffusion coefficient since no fitting or modeling software is needed. However, this technique requires knowledge of a number of parameters which are often difficult to measure experimentally such as the average dipole orientation, intermolecular distance, and index of refraction (see Section 3.7). In general, this is an indirect method and it must be used with caution.

In this series of compounds we find that the diffusion coefficient is significantly increased by decreasing the conjugation length and slightly enhanced by decreasing the molecular bulkiness of solubilizing groups. Compound A has the shortest conjugation length and shows the largest diffusion coefficient around 1×10^{-3} cm^2/s with exciton diffusion length of 13 nm. In comparison, compounds B and C yield similar diffusion coefficients around 0.4×10^{-3} cm^2/s and an exciton diffusion length of 9 and 8 nm, respectively. When comparing B and C within the same technique a general trend shows that the exciton diffusion coefficient and length for B is either equal or slightly greater than that of C. The variance in diffusion coefficients between compounds A, B, and C can be due to different degrees of molecular ordering in the thin films. Previous works have shown that a greater degree of molecular ordering can enhance the exciton diffusion coefficient.[2,33,60,61]

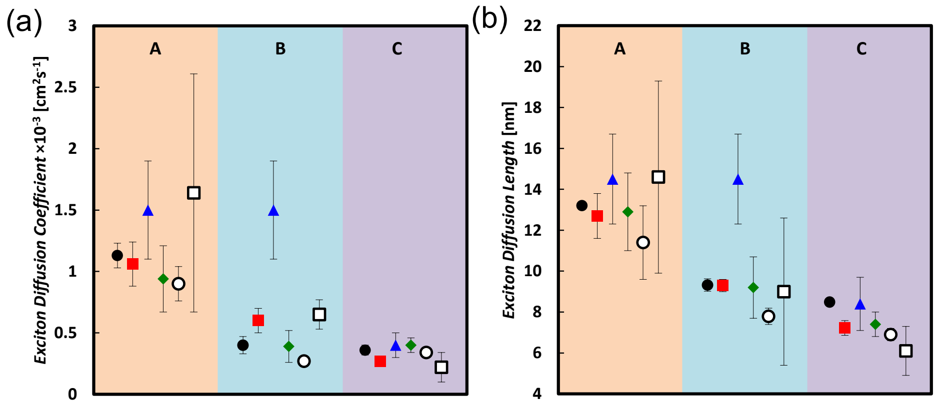

Figure 3.16. Diffusion coefficients (a) and Exciton diffusion lengths (b) for compounds A, B, and C measured with SS-SQ (black circle), TR-SQ (red square), EEA (blue triangle), BQ-MC (green diamond), BQ-SV (open circle), and FRET Theory (open square).

Figure 3.14 shows the normalized X-rays scattering intensity *versus* scattering vector Q for thin films of compounds A, B, and C. The normalization accounts for film thickness, structure factor, multiplicity, unit cell volume, and the Lorenz-Polarization factor (See Section 3.10). We also took into account the orientation of the crystallites by measuring the angular distribution of the scattered (Table 3.4). Integration of peaks areas in Figure 3.14 shows that the relative crystallinity of A is roughly 1.6 times greater than B. Compound C does not show any scattering. Therefore the relative crystallinity follows A > B > C, which is similar to the trend we observe in the diffusion coefficients. In this way we find that the diffusion coefficient correlates with the relative crystallinity.

In regards to the measurement of exciton diffusion length it is important to consider the degree of anisotropy in films. For instance, anthracene single crystals show L_D = 36, 60, and 100 nm in the c, a, and b crystalline directions respectively.[62] In our analysis of the angular distribution of the scattered intensity (Figure 3.13) we found that crystallites in films of A and B are textured out of plane and therefore anisotropic. While our x-ray diffraction measurements confirm the presence of anisotropy, it does not quantify degree of anisotropy since the volume fraction of amorphous and crystalline regions is not known.

To probe anisotropy in both crystalline and amorphous regions we utilized spectroscopic ellipsometry. Spectroscopic ellipsometry can be used to model the magnitude of absorption for in and out of plane direction which is correlated to the average dipole orientation of molecules in film. We find that there is no detectable anisotropy in films A, B, and C (See Section 3.9). This result suggests that the volume fraction of crystallites in films of A and B is small relative to the volume fraction of the amorphous phase.

A predominantly isotropic medium in films of A, B, and C is further supported by the following observations. The exciton diffusion length in the direction out of plane is probed by the surface quenching techniques. We found that the obtained value is very similar to the exciton diffusion length probed in three dimensions using the bulk quenching techniques. Moreover, all three materials make homogeneous mixture with PCBM molecules for PCBM concentrations of 10^{17} - 10^{18} cm^{-3} (Figure 3.8). This concentration range corresponds to the average distance between PCBM molecules of 10-20 nm. Thus the crystallites (if present) must be smaller than this distance that corresponds to the length-scale of exciton diffusion. Therefore materials A, B, and C can be considered isotropic on the scale of exciton diffusion length.

The correlation between relative crystallinity of the films with exciton diffusion length can be rationalized using the consideration that the Förster energy transfer facilitates singlet exciton diffusion in organic semiconductors. The efficiency of the FRET is rapidly decreasing with the distance between the chromophores. Therefore materials with shorter intermolecular distances are expected to have higher exciton diffusion coefficient, for similar Förster radii. Although it is difficult to estimate the intermolecular distance in mostly amorphous materials, it is likely that materials with higher affinity to form crystallites pack more densely on average. Indeed, our champion material A exhibits the highest affinity to form crystallites resulting in the largest diffusion coefficient in the series. While materials B and C show weaker affinity to form crystallites and thus lower diffusion coefficient.

From a practical stance, it is useful to investigate how the measured exciton diffusion length of a single material varies depending on the measurement technique employed. Consistent result across different techniques is achieved in the amorphous material C. In contrast, the EEA technique gives greater diffusion coefficients for compounds A and B which is attributed to exciton migration to crystalline regions where exciton-exciton collision and annihilation is enhanced. This result shows that caution should be taken when comparing exciton diffusion lengths of semi-crystalline materials measured by different techniques.

In this work we have covered six techniques to measure the exciton diffusion length. We find that certain techniques are more appropriate given the material properties along with the instrumentation and analysis software available. We find that the BQ-MC technique to be ideal for the measurement of exciton diffusion length for a broad range of materials due to its facile sample fabrication along with its minimal assumptions in modeling. However, BQ-MC does require an organic semiconductor which is miscible with PCBM, instrumentation for time-resolved spectroscopy, and simulation software. When the organic semiconductor exhibits mono-exponential decay the BQ-SV technique can be used which does not require simulation software. The EEA and FRET Theory techniques are better suited for organic semiconductors, which have poor miscibility with PCBM and are highly crystalline, since the measurements are performed on pristine films. The EEA technique is also advantageous in situations when an efficient quencher is not available. In general, surface quenching techniques such as SS-SQ and TR-SQ are the most demanding in regards to sample fabrication, measurement, and analysis. However, surface quenching techniques directly measure exciton diffusion length and can be accurately employed when the organic semiconductor and the exciton quencher are able to form a sharp and efficient quenching interface.

3.11 Conclusion

In summary, we have compared and contrasted six techniques to measure exciton diffusion length. Very good agreement between different techniques is obtained in amorphous films, whereas in semi-crystalline films the technique based on exciton-exciton annihilation gives a higher exciton diffusion coefficient and subsequently larger diffusion length than the techniques based exciton quenching. All the approaches are useful and the combined results give insight into structure-property relations for exciton diffusion. Different techniques have different advantages and disadvantages, and we discussed key differences in fabrication, measurement, and analysis. Consistent results are obtained with surface and with bulk quenching techniques, which indicates that diffusion in the direction perpendicular to the plane of the film and 3D diffusion in the bulk are not different, and hence isotropic. We find that bulk quenching techniques are convenient for systematic studies of exciton diffusion length since the sample preparation procedure is quite simple and fast and the analysis can be done using an open source Monte-Carlo software or fitting to the Stern-Volmer Equation. We investigated the dependence of exciton diffusion length on systematic chemical modifications. It is shown that decreasing the conjugation length of compound B to form compound A results in an enhancement in the exciton diffusion coefficient from 0.4×10^{-3} cm^2s^{-1} to 1×10^{-3} cm^2s^{-1} and exciton diffusion length from 9 nm to 13 nm. We attribute this to an increase in relative molecular ordering upon decreasing the conjugation length. It is also shown that decreasing the molecular bulkiness by replacement of the ethyl-hexyl groups by the linear alkyl chains has little effect on the resulting exciton diffusion parameters.

3.12 Reference

(1) Terao, Y.; Sasabe, H.; Adachi, C. *Appl. Phys. Lett.* **2007**, *90*, 103515–103515 – 3.

(2) Rim, S.-B.; Fink, R. F.; Schöneboom, J. C.; Erk, P.; Peumans, P. *Appl. Phys. Lett.* **2007**, *91*, 173504–173504 – 3.

(3) Markov, D. E.; Tanase, C.; Blom, P. W. M.; Wildeman, J. *Phys. Rev. B* **2005**, *72*, 045217.

(4) Markov, D. E.; Amsterdam, E.; Blom, P. W. M.; Sieval, A. B.; Hummelen, J. C. *J. Phys. Chem. A* **2005**, *109*, 5266–5274.

(5) Scully, S. R.; McGehee, M. D. *J. Appl. Phys.* **2006**, *100*, 034907.

(6) Goh, C.; Scully, S. R.; McGehee, M. D. *J. Appl. Phys.* **2007**, *101*, 114503.

(7) Shaw, P. E.; Ruseckas, A.; Samuel, I. D. W. *Adv. Mater.* **2008**, *20*, 3516–3520.

(8) Wu, Y.; Zhou, Y. C.; Wu, H. R.; Zhan, Y. Q.; Zhou, J.; Zhang, S. T.; Zhao, J. M.; Wang, Z. J.; Ding, X. M.; Hou, X. Y. *Appl. Phys. Lett.* **2005**, *87*, 044104–044104 – 3.

(9) Theander, M.; Yartsev, A.; Zigmantas, D.; Sundström, V.; Mammo, W.;

Andersson, M. R.; Inganäs, O. *Phys. Rev. B* **2000**, *61*, 12957.

(10) Zhou, Y. C.; Wu, Y.; Ma, L. L.; Zhou, J.; Ding, X. M.; Hou, X. Y. *J. Appl. Phys.* **2006**, *100*, 023712–023712 – 5.

(11) Mikhnenko, O. V.; Cordella, F.; Sieval, A. B.; Hummelen, J. C.; Blom, P. W. M.; Loi, M. A. *J. Phys. Chem. B* **2008**, *112*, 11601–11604.

(12) Mikhnenko, O. V.; Lin, J.; Shu, Y.; Anthony, J. E.; Blom, P. W. M.; Nguyen, T.-Q.; Loi, M. A. *Phys. Chem. Chem. Phys.* **2012**, *14*, 14196–14201.

(13) Mikhnenko, O. V.; Azimi, H.; Scharber, M.; Morana, M.; Blom, P. W. M.; Loi, M. A. *Energy Environ. Sci.* **2012**, *5*, 6960–6965.

(14) Cook, S.; Furube, A.; Katoh, R.; Han, L. *Chem. Phys. Lett.* **2009**, *478*, 33–36.

(15) Lewis, A. J.; Ruseckas, A.; Gaudin, O. P. M.; Webster, G. R.; Burn, P. L.; Samuel, I. D. W. *Org. Electron.* **2006**, *7*, 452–456.

(16) Masri, Z.; Ruseckas, A.; Emelianova, E. V.; Wang, L.; Bansal, A. K.; Matheson, A.; Lemke, H. T.; Nielsen, M. M.; Nguyen, H.; Coulembier, O.; Dubois, P.; Beljonne, D.; Samuel, I. D. W. *Adv. Energy Mater.* **2013**, *3*, 1445–1453.

(17) Shaw, P. E.; Ruseckas, A.; Peet, J.; Bazan, G. C.; Samuel, I. D. W. *Adv. Funct. Mater.* **2010**, *20*, 155–161.

(18) Qin, D.; Gu, P.; Dhar, R. S.; Razavipour, S. G.; Ban, D. *Phys. Status Solidi A* **2011**, *208*, 1967–1971.

(19) Stübinger, T.; Brütting, W. *J. Appl. Phys.* **2001**, *90*, 3632–3641.

(20) Yang, C. L.; Tang, Z. K.; Ge, W. K.; Wang, J. N.; Zhang, Z. L.; Jian, X. Y. *Appl. Phys. Lett.* **2003**, *83*, 1737–1739.

(21) Halls, J. J. M.; Pichler, K.; Friend, R. H.; Moratti, S. C.; Holmes, A. B. *Appl. Phys. Lett.* **1996**, *68*, 3120–3122.

(22) Ghosh, A. K.; Feng, T. *J. Appl. Phys.* **1978**, *49*, 5982–5989.

(23) Wagner, J.; Fritz, T.; Böttcher, H. *Phys. Status Solidi A* **1993**, *136*, 423–432.

(24) Bulović, V.; Forrest, S. R. *Chem. Phys. Lett.* **1995**, *238*, 88–92.

(25) Pettersson, L. A. A.; Roman, L. S.; Inganäs, O. *J. Appl. Phys.* **1999**, *86*, 487.

(26) Peumans, P.; Yakimov, A.; Forrest, S. R. *J. Appl. Phys.* **2003**, *93*, 3693.

(27) Rim, S.-B.; Peumans, P. *J. Appl. Phys.* **2008**, *103*, 124515–124515 – 5.

(28) Huijser, A.; Savenije, T. J.; Shalav, A.; Siebbeles, L. D. A. *J. Appl. Phys.* **2008**, *104*, 034505–034505 – 10.

(29) Fravventura, M. C.; Hwang, J.; Suijkerbuijk, J. W. A.; Erk, P.; Siebbeles, L. D. A.; Savenije, T. J. *J. Phys. Chem. Lett.* **2012**, *3*, 2367–2373.

(30) Savenije, T. J.; Siebbeles, L. D. In *Laser Science*; OSA Technical Digest (CD); Optical Society of America, 2010; p. LWC5.

(31) Kroeze, J. E.; Savenije, T. J.; Vermeulen, M. J. W.; Warman, J. M. *J. Phys. Chem. B* **2003**, *107*, 7696–7705.

(32) Lunt, R. R.; Giebink, N. C.; Belak, A. A.; Benziger, J. B.; Forrest, S. R. *J. Appl. Phys.* **2009**, *105*, 053711.

(33) Lunt, R. R.; Benziger, J. B.; Forrest, S. R. *Adv. Mater.* **2010**, *22*, 1233–1236.

(34) Bergemann, K. J.; Forrest, S. R. *Appl. Phys. Lett.* **2011**, *99*, 243303–243303 – 3.

(35) Rand, B. P.; Cheyns, D.; Vasseur, K.; Giebink, N. C.; Mothy, S.; Yi, Y.; Coropceanu, V.; Beljonne, D.; Cornil, J.; Brédas, J.-L.; Genoe, J. *Adv. Funct. Mater.* **2012**, *22*, 2987–2995.

(36) Mullenbach, T. K.; McGarry, K. A.; Luhman, W. A.; Douglas, C. J.; Holmes, R. J.

Adv. Mater. **2013**, *25*, 3689–3693.
(37) Pope, M.; Swenberg, C. E. *Electronic processes in organic crystals and polymers*; Oxford University Press, 1999.
(38) Jenekhe, S. A.; Yi, S. *Appl. Phys. Lett.* **2000**, *77*, 2635–2637.
(39) Manoj, A. .; Narayan, K. . *Opt. Mater.* **2003**, *21*, 417–420.
(40) Alam, M. M.; Jenekhe, S. A. *Chem Mater* **2004**, *16*, 4647–4656.
(41) Lipomi, D. J.; Chiechi, R. C.; Reus, W. F.; Whitesides, G. M.; Lipomi, D. J.; Chiechi, R. C.; Reus, W. F.; Whitesides, G. M. *Adv. Funct. Mater. Adv. Funct. Mater.* **2008**, *18, 18*, 3469, 3469–3477, 3477.
(42) Kim, C.; Liu, J.; Lin, J.; Tamayo, A. B.; Walker, B.; Wu, G.; Nguyen, T.-Q. *Chem Mater* **2012**, *24*, 1699–1709.
(43) Becker, W. *Advanced Time-Correlated Single Photon Counting Techniques*; 2005th ed.; Springer, 2005.
(44) Burkhard, G. F.; Hoke, E. T.; McGehee, M. D. *Adv. Mater.* **2010**, *22*, 3293–3297.
(45) Nocedal, J.; Wright, S. *Numerical Optimization*; 2nd ed.; Springer, 2006.
(46) Gulbinas, V.; Minevičiūtė, I.; Hertel, D.; Wellander, R.; Yartsev, A.; Sundström, V. *J. Chem. Phys.* **2007**, *127*, 144907–144907 – 8.
(47) Stevens, M. A.; Silva, C.; Russell, D. M.; Friend, R. H. *Phys. Rev. B* **2001**, *63*, 165213.
(48) Ruseckas, A.; Theander, M.; Valkunas, L.; Andersson, M. R.; Inganäs, O.; Sundström, V. *J. Lumin.* **1998**, *76–77*, 474–477.
(49) Ruseckas, A.; Ribierre, J. C.; Shaw, P. E.; Staton, S. V.; Burn, P. L.; Samuel, I. D. W. *Appl. Phys. Lett.* **2009**, *95*, 183305–183305 – 3.
(50) Ribierre, J. C.; Ruseckas, A.; Knights, K.; Staton, S. V.; Cumpstey, N.; Burn, P. L.; Samuel, I. D. W. *Phys. Rev. Lett.* **2008**, *100*, 017402.
(51) Namdas, E. B.; Ruseckas, A.; Samuel, I. D. W.; Lo, S.-C.; Burn, P. L. *Appl. Phys. Lett.* **2005**, *86*, 091104–091104 – 3.
(52) Lakowicz, J. R. *Principles of Fluorescence Spectroscopy*; Springer, 2006.
(53) Knupfer, M.; Fink, J.; Zojer, E.; Leising, G.; Fichou, D. *Chem. Phys. Lett.* **2000**, *318*, 585–589.
(54) Steinberg, I. Z. *Annu. Rev. Biochem.* **1971**, *40*, 83–114.
(55) Warren, B. E. *X-Ray Diffraction*; Courier Dover Publications, 1990.
(56) Heinemeyer, U.; Hinderhofer, A.; Alonso, M. I.; Ossó, J. O.; Garriga, M.; Kytka, M.; Gerlach, A.; Schreiber, F. *Phys. Status Solidi A* **2008**, *205*, 927–930.
(57) DeLongchamp, D. M.; Kline, R. J.; Fischer, D. A.; Richter, L. J.; Toney, M. F. *Adv. Mater.* **2011**, *23*, 319–337.
(58) Schünemann, C.; Wynands, D.; Eichhorn, K.-J.; Stamm, M.; Leo, K.; Riede, M. *J. Phys. Chem. C* **2013**, *117*, 11600–11609.
(59) Johs, B.; Hale, J. S. *Phys. Status Solidi A* **2008**, *205*, 715–719.
(60) Siebbeles, L. D. A.; Huijser, A.; Savenije, T. J. *J. Mater. Chem.* **2009**, *19*, 6067–6072.
(61) Wei, G.; Lunt, R. R.; Sun, K.; Wang, S.; Thompson, M. E.; Forrest, S. R. *Nano Lett.* **2010**, *10*, 3555–3559.
(62) Powell, R. C.; Soos, Z. G. *J. Lumin.* **1975**, *11*, 1–45.

Chapter 4. Temperature Dependence of Exciton Diffusion in a Small Molecule Organic Semiconductor Processed With and Without Additive

4.1 Introduction

Exciton diffusion plays a vital role in organic liaht emitting diodes and solar cells. In light emitting diodes a short diffusion length is desired in order to prevent exciton diffusion to non-radiative quenching sites. In contrast, a long diffusion length is needed in organic solar cells so that excitons can diffuse to the donor-acceptor interface where charges are separated leading to the generation of photocurrent. For this reason, understanding the mechanism of exciton diffusion and factors determining the diffusion length is necessary for further advancements in organic optoelectronics applications. Performance of many bulk heterojunction organic solar cells can be greatly increased upon annealing[1–6] of the active layer or when processed with high boiling point additives. [7–19] [9]

This enhancement in the device performance is associated with more favorable morphology of donor-acceptor blends, which is characterized by a greater percolation network and a higher degree of crystallinity of donor material as compared to as-cast films.[10–13,18,20] Additives slow down the solvent evaporation rate providing more time for molecular ordering during the casting process. It is expected that the exciton diffusion length is longer in crystalline domains as compared to amorphous material.[21–26] However, a previous work found that the exciton diffusion length decreases from 9 to 3 nm upon annealing in a thin film of small molecule diketopyrrolopyrrole (DPP).[27]

Interestingly, the power conversion efficiency of a solar cell based on the blend of this small molecule with [6,6]-phenyl C_{61} butyric acid methyl ester (PCBM) shows an increase upon annealing.[28] This counterintuitive result shows that further study is needed in order to understand how processing conditions impact the exciton diffusion length.

Here we investigate exciton diffusion in a small molecule compound $DTS(FBTTh_2)_2$ (see inset in Figure 4.1) that shows striking contrast in solar cell performance depending on processing conditions.[29] Surprisingly, $DTS(FBTTh_2)_2$ exhibits a decrease in the exciton diffusion length upon thermal treatment or processing with DIO. To understand the underlying physical processes that limit exciton diffusion in treated films, we study the temperature dependence of exciton diffusion in this material. We find that processing with DIO leads to the emergence of additional exciton traps that are responsible to shorter diffusion length.

4.2 Room Temperature Exciton Diffusion Length

In this work the exciton diffusion length was determined by simulating the photoluminescence (PL) decay of blend films with a Monte Carlo software.[25,27,30] The inset in Figure 4.1 shows that PL decay time becomes shorter for blends with higher PCBM concentration due to diffusion-limited exciton quenching at the PCBM-$DTS(FBTTh_2)_2$ interface. This method involves PL decay measurements on organic semiconductor blend films with an exciton quencher such as PCBM. Fitted decay curves are integrated in order to calculate the quenching efficiency Q:

$$Q = 1 - \frac{\int PL_{blend}\, dt}{\int PL_{pristine}\, dt} \tag{1}$$

where $\int PL_{blend}dt$ and $\int PL_{pristine}dt$ are the integrated time-resolved PL for the blend and pristine organic semiconductor films respectively. The PL decays are normalized to the value t = 0 prior to integration. The Monte Carlo simulation is then used to fit for the exciton diffusion length necessary to reproduce the experimentally measured quenching efficiency obtained at a specific PCBM volume fraction.

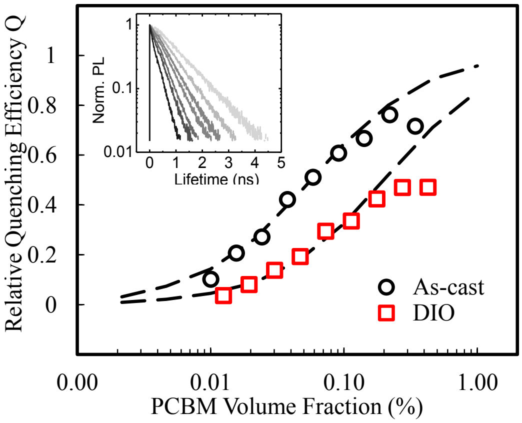

Figure 4.1. Time-resolved PL quenching of as-cast (circle markers) and DIO-processed (square markers) blend films. Measured data (markers) were simulated (dashed lines) with a Monte Carlo program. The inset shows the normalized photoluminescence decay curves of as-cast $DTS(FBTTh_2)_2$:PCBM blend films with PCBM concentrations ranging from 0 (light grey) to 0.76 wt % (black).

The Monte Carlo simulation assumes an intimate mixture of the organic semiconductor and the exciton quencher. Figure 4.1 shows the measured relative quenching efficiency of as-cast (circle markers) and DIO-processed (square markers) films of $DTS(FBTTh_2)_2$ with PCBM volume fractions ranging from 0 to 0.2%. The dashed lines were modeled using the Monte Carlo simulation. The Monte Carlo simulation curve accurately describes the experimentally measured quenching efficiencies for PCBM volume fractions ranging from 0.01 to 0.2%. This result confirms that PCBM molecules are homogenously distributed in $DTS(FBTTh_2)_2$ films at PCBM volume fractions up to 0.2%. At PCBM volume fractions above 0.2%, the experimentally measured relative quenching efficiency deviates from the Monte Carlo simulation curve for as-cast and DIO-processed films. This has been observed in pervious works and is attributed to the formation of PCBM clusters at high PCBM concentrations which reduce the surface quenching volume and therefore the relative quenching efficiency.[25,27,30] In order to ensure a homogenous mixture, PCBM volume fractions of 0.024 and 0.073 % were used for as-cast and DIO-processed films, respectively, to study the temperature dependence of exciton diffusion length.

The dynamics of excitons in such blends can be easily modeled using Stern-Volmer analysis[31] because these thin films exhibit monoexponential PL decays and PCBM forms homogenous blends with DTS(FBTTh$_2$)$_2$ in the concentration range relevant for exciton diffusion. In Stern-Volmer analysis, the inverse lifetimes of the blend films are plotted against the quencher concentration and then fitted with the following equation:[27,31,32]

$$\frac{1}{\tau} = \frac{1}{\tau_f} + 4\pi r D c, \tag{2}$$

where τ_f is the lifetime of the pristine DTS(FBTTh$_2$)$_2$ film, τ is the lifetime of the blend film, r is the sum of the exciton and PCBM radii that can be approximated as 1 nm, c is the concentration of PCBM, and D is the diffusion coefficient, which is the only fitting parameter. Figure 4.2 shows the experimental data for the as-cast and DIO-processed films, as well as the corresponding fitting with Equation 3. As-cast and DIO-processed films yield diffusion coefficients of $(4.6 \pm 0.2) \times 10^{-4}$ and $(3.1 \pm 0.2) \times 10^{-4}$ cm^2/s, respectively. Using the relationship $L_D = \sqrt{D\tau}$ and the values of PL decay time in PCMB-free films of 1 and 0.8 ns, we extract the one-dimensional exciton diffusion length of (6.8 ± 0.4) nm and (4.9 ± 0.3) nm, respectively. Interestingly, the exciton diffusion length of the DIO-processed DTS(FBTTh$_2$)$_2$ is shorter than for the case of as-cast material. This result is unexpected, because the solar cells processed with DIO generally show higher performance than as-cast materials suggesting longer exciton diffusion in DIO treated devices.[10,12,18,20] In addition, it has been shown that DIO additive leads to enhanced crystallinity, which is often associated with longer exciton diffusion length.[21–24,26]

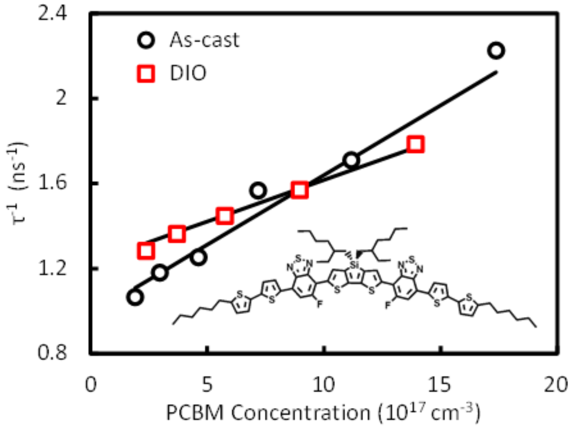

Figure 4.2. Stern-Volmer Plot for as-cast (black circles) and DIO-processed (red squares) DTS(FBTTh$_2$)$_2$:PCBM blends. Measurements (markers) were fitted with the Stern-Volmer equation (lines).

4.3 Room Temperature Exciton Trap Density

To understand the difference in exciton diffusion length for as-cast and DIO-processed DTS(FBTTh$_2$)$_2$ films we determine the number of excitonic traps, which are present in pristine films even prior addition of PCBM. Stern-Volmer analysis can be used to extract the excitonic trap density c_0 following the procedure described in Ref. 32.

$$c_0 = \frac{1}{4\pi r D}\left(\frac{1}{\tau_f} - \frac{1}{\tau_0}\right), \tag{3}$$

where τ_f is the PL decay time of pristine film, and τ_0=1.5 ns is the PL decay time of DTS(FBTTh$_2$)$_2$ in a dilute solution. Using this analysis we measure a trap density of 3.8×10^{17} cm^{-3} and 1.5×10^{18} cm^{-3} for as-cast and DIO-processed films, respectively. The excitonic trap density in DIO-processed films is nearly four times greater than in as-cast films. Thus, the reduction of the exciton diffusion length in DIO-processed samples may be due to the increase in the excitonic trap density, as compared to the as-cast films.

4.4 Morphology

Figure 4.3 shows the surface topography for as-cast and DIO-processed DTS(FBTTh$_2$)$_2$ films. Processing with DIO leads to an increase in the roughness and fiber like structures. It is likely that the presence of a high boiling point additive reduces the drying speed thereby extending the film formation process and enhancing molecular ordering.

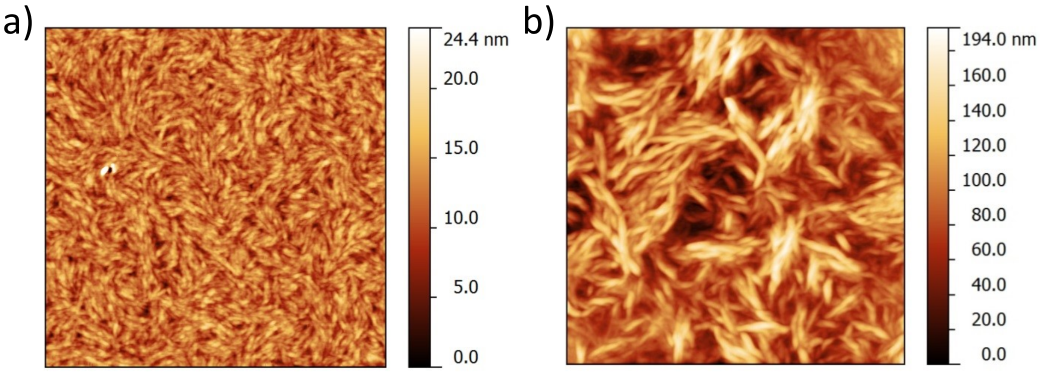

Figure 4.3. Surface topography for a) as-cast and b) DIO-processed DTS(FBTTh$_2$)$_2$ films. Scan sizes are 10 × 10 μm.

The emergence of the grain boundaries is evident from atomic force microscopy (Figure 4.3) showing that processing with DIO leads to the formation of multicrystalline fiber-like structures. It is possible that the grain boundaries between ordered and amorphous regions serve as exciton quenching sites thereby increasing the excitonic trap density and reducing the exciton diffusion length in DIO-processed films.[23] To determine how DIO-processing impacts molecular ordering we used thin film x-ray diffraction.

4.5 X-ray diffraction

Figure 4.4 shows the thin film X-ray diffraction of as-cast and DIO-processed DTS(FBTTh$_2$)$_2$ films. Processing with DIO yields a slight increase in diffraction intensity. In addition, multicrystallinity of annealed and DIO-processed DTS(FBTTh$_2$)$_2$ films is observed with transmission electron microscopy.[33] We performed Stern-Volmer analysis on thermally annealed films and found that exciton diffusion length is also decreased down to (2.8 ± 0.2) nm with exciton trap density of 7.26×10^{18} cm^{-3}, indicating that increased trap density in multicrystalline films is not related to possible residuals of DIO molecules in the film.

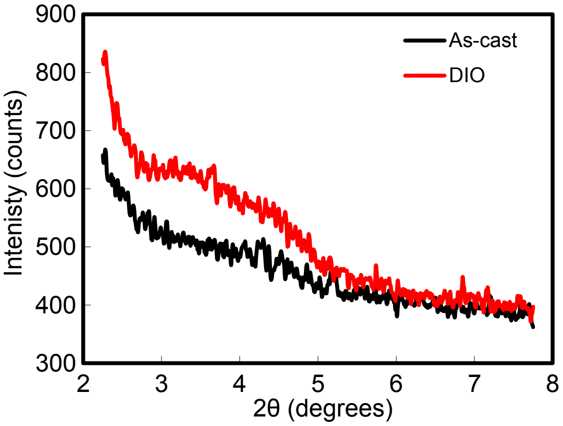

Figure 4.4. Thin film X-ray diffraction for pristine as-cast (black line) and DIO-processed (red line) DTS(FBTTh$_2$)$_2$ films.

4.6 Temperature Dependent Exciton Diffusion Length

To further investigate the exciton trapping in as-cast and DIO-processed material we performed a temperature dependent study. Figure 4.5 shows the steady state photoluminescence of pristine as-cast and DIO-processed film of DTS(FBTTh$_2$)$_2$ at 293, 150, and 10 K. The PL spectra for pristine as-cast and DIO-processed films were normalized at the high energy peak at 780 nm. At room temperature both processing conditions exhibit broad and featureless absorption (see inset Figure 4.5a) and photoluminescence spectra (see Figure 4.5). Upon cooling down to 150 K and below, the PL spectra show two distinct peaks at 780 and 850 nm. The PL decay dynamics were therefore measured at both the high and low energy emission peaks.

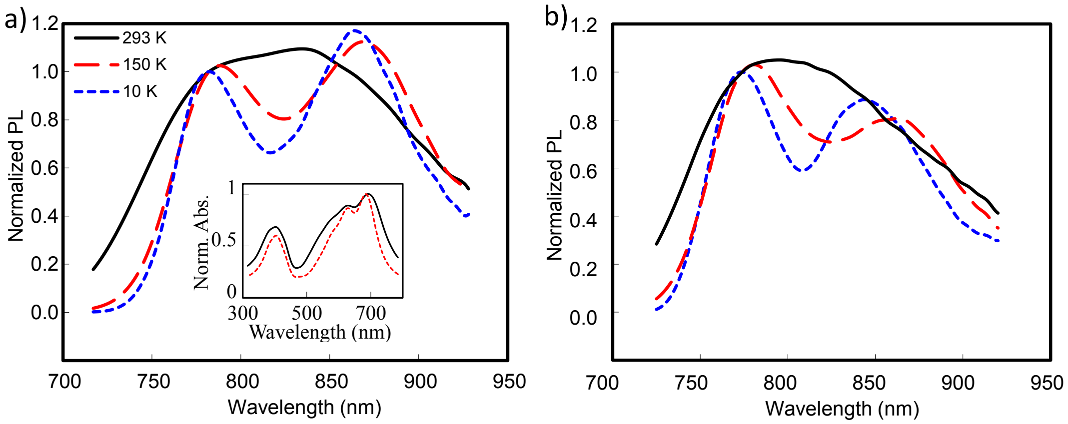

Figure 4.5. Normalized PL of a) as-cast films and b) film processed with 0.4% DIO at 293 K (solid black line), 150 K (dashed red line), and 10 K (dotted blue line). Inset in (a) shows the chemical structure of DTS(FBTTh$_2$)$_2$. Inset in (a) shows the normalized absorption of an as-cast (black line) and DIO-processed (dashed red line) film.

The PL decays were found to be mono-exponential at all conditions, with an exception of high energy emission peak of the as-cast films, which at temperatures below 120 K exhibits a small increase of PL intensity at times right after excitation for the time interval of ~200 ps (Figure 4.6). The nature of this rise-time is not entirely understood, however, we find that the temperature dependence of exciton diffusion parameters is the same for the high and the low energy peaks (Figure 4.7). The following analysis is in regards to the lower energy peak around 850 nm for both processing conditions.

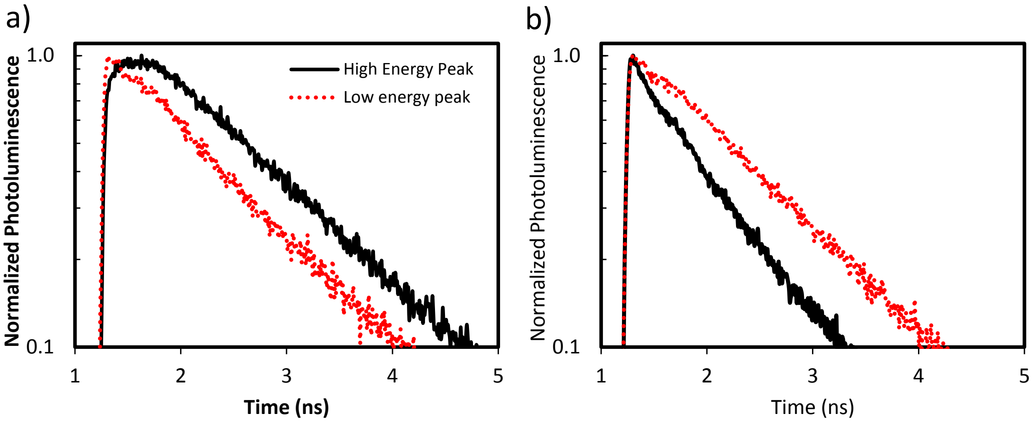

Figure 4.6. Photoluminescence decay for a) as-cast and b) DIO-processed films at the high (black line) and low (red dots) energy peak emission.

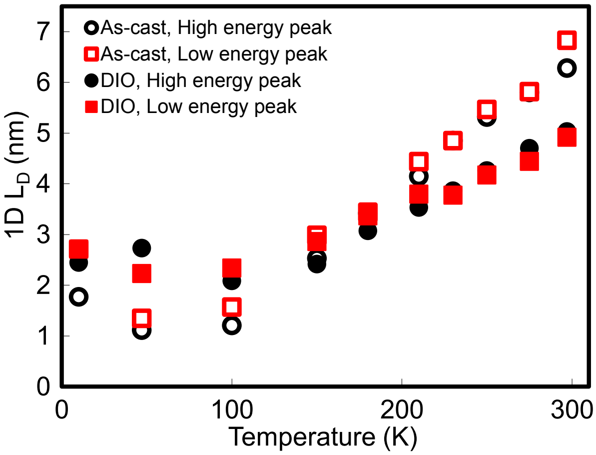

Figure 4.7. Exciton diffusion length for as-cast (open markers) and DIO-processed films (filled markers) derived from the high (circle markers) and low (square markers) energy peaks.

The temperature dependent exciton diffusion parameters are extracted by modeling of PL decays of DTS(FBTTh$_2$)$_2$ films blended with PCBM using a Monte Carlo simulation, which is described elsewhere.[25,27,30,34] We concentrate on blends with PCBM concentrations of 0.054 wt% and 0.162 wt% for as-cast and DIO-processed materials, respectively. These blends exhibit a fair degree of quenching around 50% at room temperature and form intimate mixtures with PCBM (Figure 4.2).

Figure 4.8 shows the temperature dependence of exciton diffusion coefficient and diffusion length for as-cast and DIO-processed films. Two temperature regimes can be identified based on these data. In the temperature range of 120 – 300 K, exciton diffusion parameters are increasing with temperature, while they are nearly constant below 120 K. Very similar behavior was observed for exciton diffusion in conjugated polymers,[35–48] suggesting that solution processed small molecules are similar to conjugated polymers, when it comes to exciton diffusion. In high temperature regime above 120 K the exciton diffusion is thermally activated, while at cryogenic temperatures excitons undergo downhill migration within the density of excitonic states (DOS) toward lower energies.

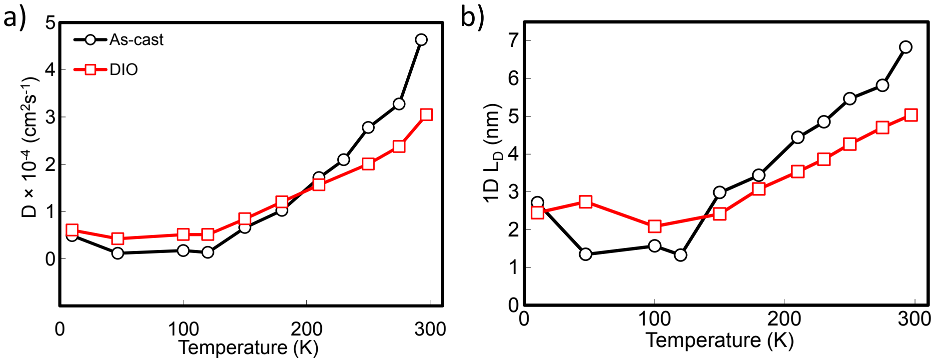

Figure 4.8. Temperature dependence of (a) diffusion coefficient D, and (b) exciton diffusion length 1D L_D for as-cast (black circles) and DIO-processed (red squares) DTS(FBTTh$_2$)$_2$:PCBM blends.

When compared to the polymer poly[2-methyl-5-(3′,7′-dimethyloctyloxy)-p-phenylenevinylene] (MDMO-PPV),[37] the small molecule compound DTS(FBTTh$_2$)$_2$ shows similar diffusion coefficient around (3 – 4) × 10^{-4} cm^2/s at room temperature. In contrast, in the low temperature regime the value of diffusion coefficient of

$DTS(FBTTh_2)_2$ is one order of magnitude less than in the polymer. In this temperature regime the excitons are only able to hop toward lower energy sites, and therefore the effectiveness of diffusion is directly related to the width of the DOS. Relative to polymers, small molecules are often more ordered and do not suffer from polydispersity, therefore their density of excitonic states is narrower than in polymers. Eisenmenger et al. showed that similar $DTS(FBTTh_2)_2$ isomers yield a lower energetic disorder than P3HT:PCBM films.[49] Consequently the exciton diffusion coefficient is significantly Suppressed at low temperatures in $DTS(FBTTh_2)_2$, as compared to MDMO-PPV.[37] Following the same reasoning we can estimate that the excitonic DOS of DIO-processed films is wider than the as-cast materials, since the DIO samples show larger diffusion coefficient than the as-cast films in the low temperature regime. Wider density of excitonic states of the DIO-processed films can be rationalized by the coexistence of crystalline and amorphous regions, which are expected to have somewhat different DOS.[50]

Figure 4.9 presents the pairs of exciton diffusion length and coefficients measured at different temperatures on a log-log scale. The curves are modeled using the Monte Carlo simulation by setting the exciton lifetime to the value of PL decay time of $DTS(FBTTh_2)_2$ in solution at room temperature (1.5 ns). In this modeling the density of exciton quenchers was varied in the range from 0 to 2×10^{18} cm^{-3}. If the quenchers are absent, then the modeling results in a straight line with slope of 0.5 in accordance with the relationship $L_D = \sqrt{D\tau}$. When quenchers are introduced, the modeled curves deviate from this relationship due to the diffusion-limited quenching. The slopes for the measured data are 0.45 ± 0.01 (as-cast) and 0.40 ± 0.1 (DIO), which correspond to the modeled curves with trap densities of 5 × 10^{17} and 1.5 × 10^{18} cm^{-3}, respectively. These trap densities are in a good agreement with the trap densities obtained from the Stern-Volmer analysis.

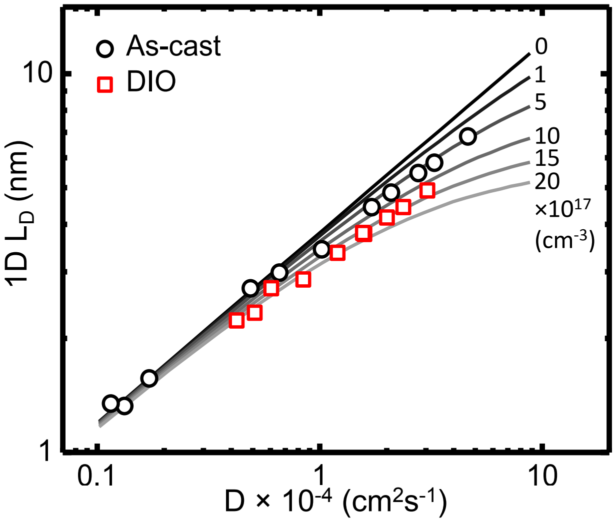

Figure 4.9. Experimentally measured exciton diffusion coefficients and diffusion lengths for as-cast (circle markers) and DIO-processed (square markers) films. The solid lines where generated from a Monte Carlo program which simulates the exciton diffusion length with a given exciton lifetime and trap density. Exciton lifetime of 1.5 ns measured in dilute solution was used as an input parameter to the simulation. The trap density increases from 0 (light grey) to 2 × 10^{18} cm^{-3} (black).

In most of the organic systems, including DTS(FBTTh$_2$)$_2$, exciton lifetime is increased upon cooling due to reduction of the non-radiative decay rate and reduction of the diffusion-limited quenching at exciton traps. Although the modeling in Figure 4.9 neglects the changes in the non-radiative decay rate, it describes the measured data well by arriving at the trap densities that where independently determined from the Stern-Volmer analysis. This suggests that the diffusion-limited quenching at excitonic traps has larger impact on the exciton lifetime than the non-radiative decay for films processed at both conditions.

4.7 Conclusions

In conclusion, exciton diffusion length in thin films of films of DTS(FBTTh$_2$)$_2$ strongly depends on the processing conditions. Amorphous as-cast films show the longest diffusion length of (6.8 ± 0.4) nm, while the diffusion length is reduced to (4.9 ± 0.3) nm and (2.8 ± 0.2) nm in thin films with induced crystallinity by processing with DIO and post-deposition annealing, respectively. We associate such dramatic decrease by emergence of excitonic traps with density of the order of 1.2×10^{18} cm^{-3}. The exciton quenching defects are likely located at grain boundaries of the polycrystalline films. These findings are supported with temperature dependent measurements of exciton diffusion parameters. The temperature dependent data can be modeled using Monte Carlo simulation using a fixed density of excitonic traps and PL decays obtained at room temperature, which suggests that the diffusion limited quenching at the defects has a major influence on the exciton lifetime. As in the case of conjugated polymers, the exciton diffusion in the studied small molecular system shows two temperature regimes. At temperatures of 120 - 300 K the diffusion coefficient and length are monotonically decreasing with cooling, while it is nearly constant at lower temperatures. However, we found that the low temperature exciton diffusion coefficient is one order of magnitude lower in DTS(FBTTh$_2$)$_2$ as compared to a polymeric system.

4.8 Experimental

Compound DTS(FBTTh$_2$)$_2$ was synthesized as previous reported.[29] DIO was purchased from Aldrich. PCBM was acquired from Nano-C. The films were spin-coated onto quartz substrates from chloroform solution with and without addition of 0.4% (by volume) DIO. All solutions where stirred overnight at 50 °C prior casting. The film thickness was controlled using a profilometer to make sure that all samples are at least 100 nm thick. To prevent photodegradation, all films were encapsulated in the glovebox with two-part epoxy and second quartz substrate. Encapsulated films were placed in a He-flow cryostat for PL measurements. Time-resolved PL measurements were performed by time-correlated single photon counter when exciting samples at 387 nm with frequency doubled 100 fs Ti-sapphire laser. The UV-Vis absorption spectra of films were measured with a Beckman Coulter DU 800 Spectrometer. Thin-film XRD spectra were measured on device architectures of Quartz/film with a X'Pert Phillips Material Research Diffractometer. Samples were scanned at 45kV and 40 mA with a scanning rate of 0.004 degree per second, and Cu Kα radiation (wavelength λ = 1.5405 Å). In the 2θ-ω scan configurations each film was scanned from 4 to 30 2θ.

4.9 Reference

(1) Reyes-Reyes, M.; Kim, K.; Carroll, D. L. *Appl. Phys. Lett.* **2005**, *87*, 083506.
(2) Yang, X.; Loos, J.; Veenstra, S. C.; Verhees, W. J. H.; Wienk, M. M.; Kroon, J. M.; Michels, M. A. J.; Janssen, R. A. J. *Nano Lett.* **2005**, *5*, 579–583.
(3) Kim, K.; Liu, J.; Carroll, D. L. *Appl. Phys. Lett.* **2006**, *88*, 181911.
(4) Mihailetchi, V. D.; Xie, H. X.; de Boer, B.; Koster, L. J. A.; Blom, P. W. M. *Adv. Funct. Mater.* **2006**, *16*, 699–708.
(5) Vanlaeke, P.; Vanhoyland, G.; Aernouts, T.; Cheyns, D.; Deibel, C.; Manca, J.; Heremans, P.; Poortmans, J. *Thin Solid Films* **2006**, *511–512*, 358–361.
(6) Walker, B.; Tamayo, A. B.; Dang, X.-D.; Zalar, P.; Seo, J. H.; Garcia, A.; Tantiwiwat, M.; Nguyen, T.-Q. *Adv. Funct. Mater.* **2009**, *19*, 3063–3069.
(7) Peet, J.; Brocker, E.; Xu, Y.; Bazan, G. C. *Adv. Mater.* **2008**, *20*, 1882–1885.
(8) Moulé, A. J.; Meerholz, K. *Adv. Funct. Mater.* **2009**, *19*, 3028–3036.
(9) Hoven, C. V.; Dang, X.-D.; Coffin, R. C.; Peet, J.; Nguyen, T.-Q.; Bazan, G. C. *Adv. Mater.* **2010**, *22*, E63–E66.
(10) Jeong, S.; Woo, S.-H.; Lyu, H.-K.; Han, Y. S. *Sol. Energy Mater. Sol. Cells* **2011**, *95*, 1908–1914.
(11) Pivrikas, A.; Neugebauer, H.; Sariciftci, N. S. *Sol. Energy* **2011**, *85*, 1226–1237.

(12) Rogers, J. T.; Schmidt, K.; Toney, M. F.; Kramer, E. J.; Bazan, G. C. *Adv. Mater.* **2011**, *23*, 2284–2288.
(13) Sun, Y.; Cui, C.; Wang, H.; Li, Y. *Adv. Energy Mater.* **2011**, *1*, 1058–1061.
(14) Albrecht, S.; Schindler, W.; Kurpiers, J.; Kniepert, J.; Blakesley, J. C.; Dumsch, I.; Allard, S.; Fostiropoulos, K.; Scherf, U.; Neher, D. *J. Phys. Chem. Lett.* **2012**, *3*, 640–645.
(15) Liu, J.; Han, Y. *Polym. Bull.* **2012**, *68*, 2145–2174.
(16) Park, J. K.; Kim, C.; Walker, B.; Nguyen, T.-Q.; Seo, J. H. *RSC Adv.* **2012**, *2*, 2232–2234.
(17) Ferdous, S.; Liu, F.; Wang, D.; Russell, T. P. *Adv. Energy Mater.* **2014**, *4*, 1–10.
(18) Liao, H.-C.; Ho, C.-C.; Chang, C.-Y.; Jao, M.-H.; Darling, S. B.; Su, W.-F. *Mater. Today* **2013**, *16*, 326–336.
(19) Schmidt, K.; Tassone, C. J.; Niskala, J. R.; Yiu, A. T.; Lee, O. P.; Weiss, T. M.; Wang, C.; Fréchet, J. M. J.; Beaujuge, P. M.; Toney, M. F. *Adv. Mater.* **2014**, *26*, 300–305.
(20) Peet, J.; Soci, C.; Coffin, R. C.; Nguyen, T. Q.; Mikhailovsky, A.; Moses, D.; Bazan, G. C. *Appl. Phys. Lett.* **2006**, *89*, 252105.
(21) Rim, S.-B.; Fink, R. F.; Schöneboom, J. C.; Erk, P.; Peumans, P. *Appl. Phys. Lett.* **2007**, *91*, 173504–173504 – 3.
(22) Siebbeles, L. D. A.; Huijser, A.; Savenije, T. J. *J. Mater. Chem.* **2009**, *19*, 6067–6072.
(23) Lunt, R. R.; Benziger, J. B.; Forrest, S. R. *Adv. Mater.* **2010**, *22*, 1233–1236.
(24) Wei, G.; Lunt, R. R.; Sun, K.; Wang, S.; Thompson, M. E.; Forrest, S. R. *Nano Lett.* **2010**, *10*, 3555–3559.
(25) Lin, J. D. A.; Mikhnenko, O. V.; Chen, J.; Masri, Z.; Ruseckas, A.; Mikhailovsky, A.; Raab, R. P.; Liu, J.; Blom, P. W. M.; Loi, M. A.; García-Cervera, C. J.; Samuel, I. D. W.; Nguyen, T.-Q. *Mater. Horiz.* **2014**, *1*, 280–285.
(26) Sim, M.; Shin, J.; Shim, C.; Kim, M.; Jo, S. B.; Kim, J.-H.; Cho, K. *J. Phys. Chem. C* **2014**, *118*, 760–766.
(27) Mikhnenko, O. V.; Lin, J.; Shu, Y.; Anthony, J. E.; Blom, P. W. M.; Nguyen, T.-Q.; Loi, M. A. *Phys. Chem. Chem. Phys.* **2012**, *14*, 14196–14201.
(28) Lin, J. D. A.; Liu, J.; Kim, C.; Tamayo, A. B.; Proctor, C. M.; Nguyen, T.-Q. T. *RSC Adv.* **2014**, *4*, 14101–14108.
(29) Van der Poll, T. S.; Love, J. A.; Nguyen, T.-Q.; Bazan, G. C. *Adv. Mater.* **2012**, *24*, 3646–3649.
(30) Mikhnenko, O. V.; Azimi, H.; Scharber, M.; Morana, M.; Blom, P. W. M.; Loi, M. A. *Energy Environ. Sci.* **2012**, *5*, 6960–6965.
(31) Lakowicz, J. R. *Principles of Fluorescence Spectroscopy*; 3rd ed.; Springer, 2006.
(32) Mikhnenko, O. V.; Kuik, M.; Lin, J.; van der Kaap, N.; Nguyen, T.-Q.; Blom, P. W. M. *Adv. Mater.* **2013**, 1–6.
(33) Love, J. A.; Proctor, C. M.; Liu, J.; Takacs, C. J.; Sharenko, A.; van der Poll, T. S.; Heeger, A. J.; Bazan, G. C.; Nguyen, T.-Q. *Adv. Funct. Mater.* **2013**, *23*, 5019–5026.
(34) Raisys, S.; Kazlauskas, K.; Daskeviciene, M.; Malinauskas, T.; Getautis, V.; Jursenas, S. *J. Mater. Chem. C* **2014**, *2*, 4792–4798.

(35) Bjorklund, T. G.; Lim, S.-H.; Bardeen, C. J. *J. Phys. Chem. B* **2001**, *105*, 11970–11977.
(36) Wells, N. P.; Boudouris, B. W.; Hillmyer, M. A.; Blank, D. A. *J. Phys. Chem. C* **2007**, *111*, 15404–15414.
(37) Mikhnenko, O. V.; Cordella, F.; Sieval, A. B.; Hummelen, J. C.; Blom, P. W. M.; Loi, M. A. *J. Phys. Chem. B* **2008**, *112*, 11601–11604.
(38) Athanasopoulos, S.; Emelianova, E. V.; Walker, A. B.; Beljonne, D. *Phys. Rev. B* **2009**, *80*, 195209.
(39) Dias, F. B.; Kamtekar, K. T.; Cazati, T.; Williams, G.; Bryce, M. R.; Monkman, A. P. *ChemPhysChem* **2009**, *10*, 2096–2104.
(40) Zhang, X.; Li, Z.; Lu, G. *Phys. Rev. B* **2011**, *84*, 235208.
(41) Schüppel, R.; Dienel, T.; Leo, K.; Hoffmann, M. *J. Lumin.* **2004**, *110*, 309–314.
(42) Madigan, C.; Bulovic, V. *Phys. Rev. Lett.* **2006**, *96*, 046404–4.
(43) Mirzov, O.; Scheblykin, I. G. *Phys. Chem. Chem. Phys.* **2006**, *8*, 5569–5576.
(44) Athanasopoulos, S.; Hoffmann, S. T.; Bässler, H.; Köhler, A.; Beljonne, D. *J. Phys. Chem. Lett.* **2013**, *4*, 1694–1700.
(45) Anni, M.; Caruso, M. E.; Lattante, S.; Cingolani, R. *J. Chem. Phys.* **2006**, *124*, 134707.
(46) Herz, L. M.; Silva, C.; Grimsdale, A. C.; Müllen, K.; Phillips, R. T. *Phys. Rev. B* **2004**, *70*, 165207.
(47) Rothberg, L. J.; Yan, M.; Papadimitrakopoulos, F.; Galvin, M. E.; Kwock, E. W.; Miller, T. M. *Synth. Met.* **1996**, *80*, 41–58.
(48) Li, Z.; Zhang, X.; Lu, G. *J. Phys. Condens. Matter* **2014**, *26*, 185006.
(49) Eisenmenger, N. D.; Su, G. M.; Welch, G. C.; Takacs, C. J.; Bazan, G. C.; Kramer, E. J.; Chabinyc, M. L. *Chem. Mater.* **2013**, *25*, 1688–1698.
(50) Noriega, R.; Rivnay, J.; Vandewal, K.; Koch, F. P. V.; Stingelin, N.; Smith, P.; Toney, M. F.; Salleo, A. *Nat. Mater.* **2013**, *12*, 1038–1044.

Chapter 5. Exciton Diffusion Length in Small Molecules Used in High Performance Organic Solar Cells

5.1 Introduction

In recent years there has been an increasingly greater interest to utilize solution-processed small molecules in organic photovoltaic (OPV) devices. A number of works have also shown that efficiencies between 4 − 7% can be achieved in small molecule bulk heterojunction (BHJ) OPV devices.[1–8] Solution processibility in small molecules is relevant to industry as is would eases the scale up process. Small molecules also offer the advantage of studying how slight chemical modifications impact fundamental processes in OPV devices, which is significantly more challenging to do with polymers. One important fundamental processing in organic solar cells is the diffusion of columbic charged pairs or excitons to the donor-acceptor quenching interface. A greater exciton diffusion length is desirable as it increases the probability of excitons reaching a quenching interface whereby charge separation and generation may occur. In the current body of literature the exciton diffusion length has been measured in a number of small molecules.[9–27] In the majority of these studies the small molecules are thermally evaporated thereby yielding highly ordered and crystalline films.[27–31] Most of these studies also measure the exciton diffusion length in 1D and in the direction perpendicular to the substrate. The measurement of the exciton diffusion length in this configuration is relevant to bilayers OPV devices. However, in solution-processed small molecule BHJ OPV devices, excitons must diffuse in three dimensions to reach a quenching interface.

Furthermore, solution-processed films are predominantly amorphous relative to thermally evaporated films. It is therefore necessary to measured exciton diffusion in 3D and in a predominantly amorphous medium in order to better understand exciton diffusion in solution-processed BHJ OPV devices.

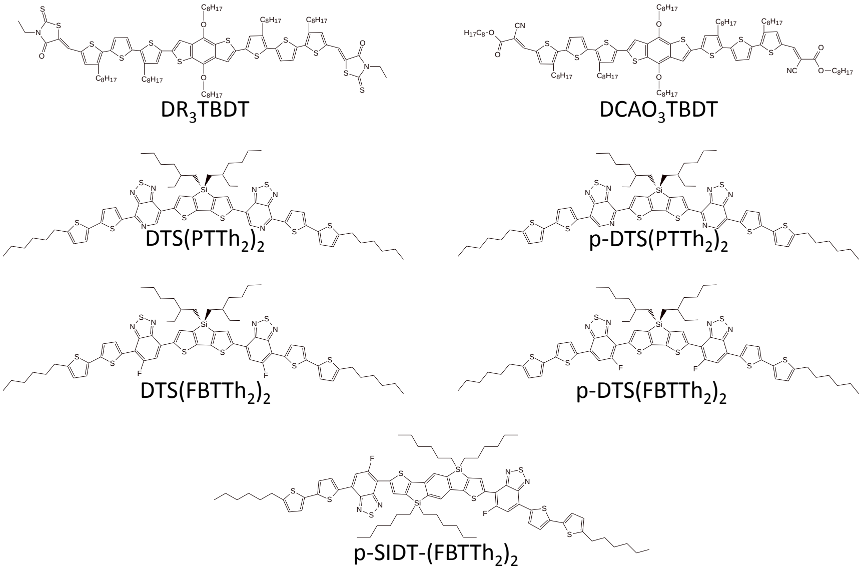

DR_3TBDT

$DCAO_3TBDT$

$DTS(PTTh_2)_2$

p-$DTS(PTTh_2)_2$

$DTS(FBTTh_2)_2$

p-$DTS(FBTTh_2)_2$

p-SIDT-$(FBTTh_2)_2$

Figure 5.1. Chemical structures of DR_3TBDT, $DCAO_3TBDT$, $DTS(PTTh_2)_2$, p-$DTS(PTTh_2)_2$, $DTS(FBTTh_2)_2$, p-$DTS(FBTTh_2)_2$, and p-SIDT-$(FBTTh_2)_2$.

In this work we have measured the 3D exciton diffusion length for compounds DR_3TBDT, $DCAO_3TBDT$, $DTS(PTTh_2)_2$, p-$DTS(PTTh_2)_2$, $DTS(FBTTh_2)_2$, p-$DTS(FBTTh_2)_2$, and p-SIDT-$(FBTTh_2)_2$ as shown in Figure 5.1. All compounds except $DTS(FBTTh_2)_2$, have been used to fabricate high performance OPV devices.[3–7,32] The device efficiency of $DTS(FBTTh_2)_2$ has not been published. In this work we find that the 3D exciton diffusion length varies between 2 – 13 nm and is correlated with the exciton trap density. Despite the significant variances in exciton diffusion lengths there does not appear to be a clear correlation between the solar cell device performance and the exciton diffusion length.

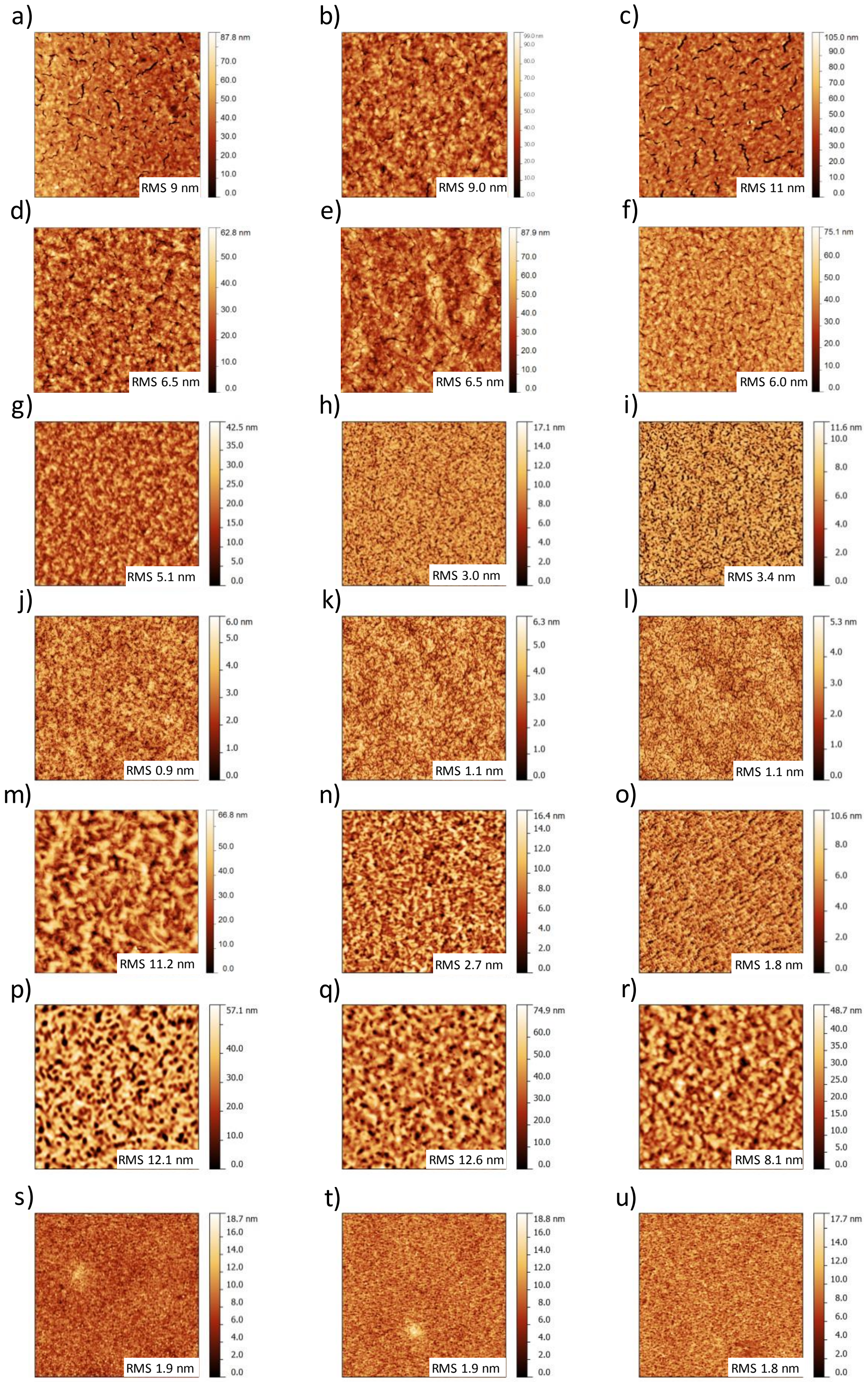

Figure 5.2. Surface topography of DR$_3$TBDT (a-c), DCAO$_3$TBDT (d-f), DTS(PTTh$_2$)$_2$ (g-i), p-DTS(PTTh$_2$)$_2$ (j-l), DTS(FBTTh$_2$)$_2$ (m-o), p-DTS(FBTTh$_2$)$_2$ (p-r), and p-SIDT-(FBTTh$_2$)$_2$ (s-u) with PCBM mass fractions of 0 (1st column), 0.11(2nd column), and 4.22% (3rd column).

5.2 Results and Discussion

The 3D exciton diffusion length for each of these materials was determined using the bulk quenching with Monte Carlo simulation technique.[22,26,33,34] Figure 5.2 shows the pristine and blend film morphologies measured with tapping mode atomic force microscopy. In general, all films exhibited rather featureless morphologies with root mean square (RMS) roughness's in the range 1 − 5 nm which may be an indication of weak molecular ordering in these films. Compound p-DTS(FBTTh$_2$)$_2$ is an exception with RMS roughness around 8 − 12 nm. Unlike bilayer techniques to measured exciton diffusion lengths,[26,35–40] the RMS roughness need not be less than 1 nm in the bulk quenching with Monte Carlo simulation technique for accurate measurements of the exciton diffusion length.

Table 1. Physical properties of compounds

Abbreviation	τ_{sol} (ps)	τ_{film} (ps)	Diffusion $\times 10^{-3}$ (cm^2s^{-1})	3D L_D (nm)	1D L_D (nm)	Trap Density $\times 10^{17}$ (cm^{-3})
DR$_3$TBDT	385	872	0.41	10.4	6.0	NA
DCAO$_3$TBDT	455	1537	0.28	11.4	6.6	NA
DTS(PTTh$_2$)$_2$	694	657	0.03	2.4	1.4	15.8
p-DTS(PTTh$_2$)$_2$	1163	971	0.08	4.7	2.7	18.8
DTS(FBTTh$_2$)$_2$	1450	1219	0.15	7.5	4.3	6.93
p-DTS(FBTTh$_2$)$_2$	1455	988	0.40	10.9	6.3	3.84
p-SIDT-(FBTTh$_2$)$_2$	2328	948	0.63	13.4	7.7	7.90

Table 1 summarizes the exciton diffusion parameters for the materials in this work. Compounds DR$_3$TBDT, DCAO$_3$TBDT, DTS(PTTh$_2$)$_2$, p-DTS(PTTh$_2$)$_2$, DTS(FBTTh$_2$)$_2$, p-DTS(FBTTh$_2$)$_2$, and p-SIDT-(FBTTh$_2$)$_2$ yielded 3D exciton diffusion lengths of 10.4, 11.4, 2.4, 4.7, 7.5, 10.9, and 13.4 nm. Using a Stern Volmer analysis technique,[26,41,42] the exciton trap densities were also determined as shown in Table 1. The trap density varies between (3.84 − 18.8) × 10^{17} cm^{-3}. The trap density of compounds DR$_3$TBDT and DCAO$_3$TBDT could not be determined due to the film lifetime being longer than the solution lifetime. Among the compounds studied here, DTS(PTTh$_2$)$_2$ and p-DTS(PTTh$_2$)$_2$ yielded significantly smaller exciton diffusion lengths of 2.4 and 4.7 nm, respectively. Interestingly, these two compounds also have the highest exciton trap density of 15.8 × 10^{17} and 18.8 × 10^{17} cm^{-3}, respectively. In other works, the origin of exciton traps has been attributed to grain boundaries, dopants, and water-oxygen complexes.[43–49] Previous works have also found that the exciton trap density can limit the exciton diffusion length.[41,42] In bilayer solar cells, a shorter exciton diffusion length has been correlated with a lower device performance.[15,27,29] From this result, one might expect compounds DTS(PTTh$_2$)$_2$ and p-DTS(PTTh$_2$)$_2$ with the highest exciton trap densities to yield OPV devices of the lowest efficiencies relative to other compounds in this work. In OPV devices compounds DR3TBDT, DCAO3TBDT, DTS(PTTh$_2$)$_2$, p-DTS(PTTh$_2$)$_2$, p-DTS(FBTTh$_2$)$_2$, and p-SIDT-(FBTTh$_2$)$_2$ have exhibited power conversion efficiencies (PCE) of 7.38, 4.56, 3.2, 6.7, 7.0, and 6.4% respectively.[3–7,32] The performance of DTS(FBTTh$_2$)$_2$ in solar cells has not been reported. Unlike previous studies in bilayers,[15,27,29] we do not observe a correlation between the device performance and the exciton diffusion length. From this result it may appear that the exciton diffusion length is an insignificant process in BHJ OPV devices. However, systems with significantly longer exciton diffusion lengths would be capable of maintaining a high exciton harvesting efficiency over a wider range of phase segregation morphologies. By relaxing the conditions necessary for efficient exciton harvesting it is possible to further optimize other processes such as charge generation, transport, and collection which would lead to greater device efficiencies.

5.3 Conclusion

In conclusion, we have measured the 3D exciton diffusion length in several small molecules that have achieved high performances in solution-processed BHJ OPV devices. The exciton diffusion length and exciton trap density varies between 2 − 13 nm and 10^{17} − 10^{18} cm^{-3}. We find a slight correlation between the exciton diffusion length and the exciton trap density. This aligns with other works which have shown that the exciton diffusion length is limited by the exciton trap density.[41] In this work we do not observe a correlation between the 3D exciton diffusion length and device performance. However, increasing the exciton diffusion length would allow for further optimization of other processes thereby enabling greater device efficiencies.

5.4 Experimental

All materials where synthesized as previously reported.[3–7,32] PCBM was acquired from Nano-C. Solution where prepared in chloroform at 4 mg/mL and stirred overnight at 50 °C. Films were spin-coated onto glass substrates at a spin speed of 400 rpm. The film thickness was controlled using a profilometer to make sure that all samples are at least 100 nm thick. To prevent photodegradation, all films were encapsulated in the glovebox with two-part epoxy and second glass substrate. Time-resolved PL measurements were performed by time-correlated single photon counter when exciting samples at 387 nm with frequency doubled 100 fs Ti-sapphire laser. Surface topographies where measured with an Innova (Veeco) atomic force microscopy instrument.

5.5 References:

(1) Shen, S.; Jiang, P.; He, C.; Zhang, J.; Shen, P.; Zhang, Y.; Yi, Y.; Zhang, Z.; Li, Z.; Li, Y. *Chem. Mater.* **2013**, *25*, 2274–2281.

(2) Liu, X.; Sun, Y.; Perez, L. A.; Wen, W.; Toney, M. F.; Heeger, A. J.; Bazan, G. C. *J. Am. Chem. Soc.* **2012**, *134*, 20609–20612.

(3) Welch, G. C.; Perez, L. A.; Hoven, C. V.; Zhang, Y.; Dang, X.-D.; Sharenko, A.; Toney, M. F.; Kramer, E. J.; Nguyen, T.-Q.; Bazan, G. C. *J. Mater. Chem.* **2011**, *21*, 12700–12709.

(4) Van der Poll, T. S.; Love, J. A.; Nguyen, T.-Q.; Bazan, G. C. *Adv. Mater.* **2012**, *24*, 3646–3649.

(5) Zhou, J.; Wan, X.; Liu, Y.; Zuo, Y.; Li, Z.; He, G.; Long, G.; Ni, W.; Li, C.; Su, X.; Chen, Y. *J. Am. Chem. Soc.* **2012**, *134*, 16345–16351.

(6) Sun, Y.; Welch, G. C.; Leong, W. L.; Takacs, C. J.; Bazan, G. C.; Heeger, A. J. *Nat. Mater.* **2012**, *11*, 44–48.

(7) Zhou, J.; Zuo, Y.; Wan, X.; Long, G.; Zhang, Q.; Ni, W.; Liu, Y.; Li, Z.; He, G.; Li, C.; Kan, B.; Li, M.; Chen, Y. *J. Am. Chem. Soc.* **2013**, *135*, 8484–8487.

(8) Roncali, J.; Leriche, P.; Blanchard, P. *Adv. Mater.* **2014**, *26*, 3821–3838.

(9) Vaubel, G.; Baessler, H. *Mol. Cryst. Liq. Cryst.* **1970**, *12*, 47–56.

(10) Gregg, B. A.; Sprague, J.; Peterson, M. W. *J. Phys. Chem. B* **1997**, *101*, 5362–5369.

(11) Stübinger, T.; Brütting, W. *J. Appl. Phys.* **2001**, *90*, 3632–3641.

(12) Yang, C. L.; Tang, Z. K.; Ge, W. K.; Wang, J. N.; Zhang, Z. L.; Jian, X. Y. *Appl. Phys. Lett.* **2003**, *83*, 1737–1739.

(13) Kawamura, Y.; Sasabe, H.; Adachi, C. *Jpn. J. Appl. Phys.* **2004**, *43*, 7729–7730.

(14) Bansal, A. K.; Holzer, W.; Penzkofer, A.; Tsuboi, T. *Chem. Phys.* **2006**, *330*, 118–129.

(15) Terao, Y.; Sasabe, H.; Adachi, C. *Appl. Phys. Lett.* **2007**, *90*, 103515–103515 – 3.

(16) Holzhey, A.; Uhrich, C.; Brier, E.; Reinhold, E.; Bäuerle, P.; Leo, K.; Hoffmann, M. *J. Appl. Phys.* **2008**, *104*, 064510–064510 – 8.

(17) Cook, S.; Furube, A.; Katoh, R.; Han, L. *Chem. Phys. Lett.* **2009**, *478*, 33–36.

(18) Gommans, H.; Schols, S.; Kadashchuk, A.; Heremans, P.; Meskers, S. C. J. *J. Phys. Chem. C* **2009**, *113*, 2974–2979.

(19) Lunt, R. R.; Giebink, N. C.; Belak, A. A.; Benziger, J. B.; Forrest, S. R. *J. Appl. Phys.* **2009**, *105*, 053711.

(20) Qin, D.; Gu, P.; Dhar, R. S.; Razavipour, S. G.; Ban, D. *Phys. Status Solidi A* **2011**, *208*, 1967–1971.

(21) Fravventura, M. C.; Hwang, J.; Suijkerbuijk, J. W. A.; Erk, P.; Siebbeles, L. D. A.; Savenije, T. J. *J. Phys. Chem. Lett.* **2012**, *3*, 2367–2373.

(22) Mikhnenko, O. V.; Lin, J.; Shu, Y.; Anthony, J. E.; Blom, P. W. M.; Nguyen, T.-Q.; Loi, M. A. *Phys. Chem. Chem. Phys.* **2012**, *14*, 14196–14201.

(23) Mikhnenko, O. V.; Ruiter, R.; Blom, P. W. M.; Loi, M. A. *Phys. Rev. Lett.* **2012**, *108*, 137401.

(24) Menke, S. M.; Luhman, W. A.; Holmes, R. J. *Nat. Mater.* **2013**, *12*, 152–157.

(25) Li, Z.; Zhang, X.; Woellner, C. F.; Lu, G. *Appl. Phys. Lett.* **2014**, *104*, 143303.

(26) Lin, J. D. A.; Mikhnenko, O. V.; Chen, J.; Masri, Z.; Ruseckas, A.; Mikhailovsky, A.; Raab, R. P.; Liu, J.; Blom, P. W. M.; Loi, M. A.; García-Cervera, C. J.; Samuel, I. D. W.; Nguyen, T.-Q. *Mater. Horiz.* **2014**, *1*, 280–285.
(27) Rim, S.-B.; Fink, R. F.; Schöneboom, J. C.; Erk, P.; Peumans, P. *Appl. Phys. Lett.* **2007**, *91*, 173504–173504 – 3.
(28) Siebbeles, L. D. A.; Huijser, A.; Savenije, T. J. *J. Mater. Chem.* **2009**, *19*, 6067–6072.
(29) Lunt, R. R.; Benziger, J. B.; Forrest, S. R. *Adv. Mater.* **2010**, *22*, 1233–1236.
(30) Wei, G.; Lunt, R. R.; Sun, K.; Wang, S.; Thompson, M. E.; Forrest, S. R. *Nano Lett.* **2010**, *10*, 3555–3559.
(31) Sim, M.; Shin, J.; Shim, C.; Kim, M.; Jo, S. B.; Kim, J.-H.; Cho, K. *J. Phys. Chem. C* **2014**, *118*, 760–766.
(32) Love, J. A.; Nagao, I.; Huang, Y.; Kuik, M.; Gupta, V.; Takacs, C. J.; Coughlin, J. E.; Qi, L.; van der Poll, T. S.; Kramer, E. J.; Heeger, A. J.; Nguyen, T.-Q.; Bazan, G. C. *J. Am. Chem. Soc.* **2014**, *136*, 3597–3606.
(33) Mikhnenko, O. V.; Azimi, H.; Scharber, M.; Morana, M.; Blom, P. W. M.; Loi, M. A. *Energy Environ. Sci.* **2012**, *5*, 6960–6965.
(34) Raisys, S.; Kazlauskas, K.; Daskeviciene, M.; Malinauskas, T.; Getautis, V.; Jursenas, S. *J. Mater. Chem. C* **2014**, *2*, 4792–4798.
(35) Peumans, P.; Yakimov, A.; Forrest, S. R. *J. Appl. Phys.* **2003**, *93*, 3693.
(36) Markov, D. E.; Tanase, C.; Blom, P. W. M.; Wildeman, J. *Phys. Rev. B* **2005**, *72*, 045217.
(37) Markov, D. E.; Amsterdam, E.; Blom, P. W. M.; Sieval, A. B.; Hummelen, J. C. *J. Phys. Chem. A* **2005**, *109*, 5266–5274.
(38) Scully, S. R.; McGehee, M. D. *J. Appl. Phys.* **2006**, *100*, 034907.
(39) Goh, C.; Scully, S. R.; McGehee, M. D. *J. Appl. Phys.* **2007**, *101*, 114503.
(40) Mikhnenko, O. V.; Cordella, F.; Sieval, A. B.; Hummelen, J. C.; Blom, P. W. M.; Loi, M. A. *J. Phys. Chem. B* **2008**, *112*, 11601–11604.
(41) Mikhnenko, O. V.; Kuik, M.; Lin, J.; van der Kaap, N.; Nguyen, T.-Q.; Blom, P. W. M. *Adv. Mater.* **2013**, 1–6.
(42) Lin, J. D. A.; Mikhnenko, O. V.; Poll, T. S. van der; Bazan, G. C.; Nguyen, T. *Adv. Mater.* **2014**, (Submitted).
(43) Athanasopoulos, S.; Hennebicq, E.; Beljonne, D.; Walker, A. B. *J. Phys. Chem. C* **2008**, *112*, 11532–11538.
(44) Fink, R. F.; Seibt, J.; Engel, V.; Renz, M.; Kaupp, M.; Lochbrunner, S.; Zhao, H.-M.; Pfister, J.; Würthner, F.; Engels, B. *J. Am. Chem. Soc.* **2008**, *130*, 12858–12859.
(45) Traub, M. C.; Vogelsang, J.; Plunkett, K. N.; Nuckolls, C.; Barbara, P. F.; Vanden Bout, D. A. *ACS Nano* **2012**, *6*, 523–529.
(46) Björn Gieseking, T. S. **2013**.
(47) Bjorgaard, J. A.; Köse, M. E. *J. Phys. Chem. C* **2014**, *118*, 5756–5761.
(48) Feng, S.-W. *Opt. Mater. Express* **2014**, *4*, 798–809.
(49) Kuik, M.; Wetzelaer, G.-J. A. H.; Nicolai, H. T.; Craciun, N. I.; De Leeuw, D. M.; Blom, P. W. M. *Adv. Mater.* **2014**, *26*, 512–531.

Chapter 6. Conclusions

Chapter 2 of this dissertation is driven by two guiding questions: (1) How does incremental and systematic chemical modifications impact blend film morphology, absorption, charge mobility, and device performance? (2) What factors can limit a materials potential device performance? To answer these questions, a class of DPP small molecules was used to investigate how molecular bulkiness and conjugation length impact blend film morphology, absorption, crystallinity, and device performance. In the class of small molecules studied, we show that micron scale phase segregation arises at medium and high donor:acceptor ratios when (1) the linear alkyl chains are either removal or replacement with bulky ethyl-hexyl groups or if (2) the backbone conjugation length is increased past a certain threshold. This micron scale phases segregation leads to device optimization at low donor:acceptor ratio where performance is limited by large differences in electron and hole mobilities. This work therefore affirms the need for future works to devote greater efforts in performing comprehensive characterization on not only the champion device but also similar derivatives. If additional resources were available, guiding questions for future studies related to this work include: (1) What specific driving forces induced micron scale phase segregation? (2) Can micron scale phase segregation be reduced with certain processing conditions?

Chapter 3 of this dissertation is driven by two guiding questions: (1) How do techniques to measure exciton diffusion length compare? (2) How does conjugation length and molecular bulkiness impact exciton diffusion length? To answer these questions, a class of DPP small molecules with incremental and systematic chemical modifications was used to compare the advantages and challenges in regards to the fabrication, measurement, analysis procedure for six techniques to measure the exciton diffusion length. It is determined that bulk quenching techniques are preferred over surface quenching techniques which require elaborate fabrication procedures, multiple measurements, and a number of assumptions in the analysis process. It is therefore recommended that future systematic studies of exciton diffusion length be performed with (1) the BQ-MC technique which serves a robust method, (2) BQ-SV which can be used to extract the exciton trap density, and (3) the FRET technique which would help elucidate trends in exciton diffusion lengths. This study also found that decreasing the conjugation length in a small molecule leads to an enhancement in the exciton diffusion length while replacing the linear alkyl chains with bulky ethyl-hexyl groups has no significant. If additional resources were available, guiding questions for future studies related to this work include: (1) How does the analysis procedure between the techniques compare mathematically? (2) How does the photocurrent method compare with the photoluminescent techniques studied here? (3) Can the exciton diffusion length be measured in actual BHJ films rather than just bilayers or dilute PCBM films?

Chapter 3 of this dissertation is driven by two guiding questions: (1) How does processing conditions impact exciton diffusion length? (2) What is the relationship between the exciton diffusion length and the exciton trap density? To answer these questions, we used the BQ-MC and BQ-SV techniques to measure the temperature-dependent exciton diffusion length in a small molecule system which had previously shown significant enhancements in performance when processed with DIO. Interestingly, we find that processing with DIO leads to a slight increase in molecular ordering yet a reduction in the exciton diffusion length. Using temperature dependent studies and the BQ-SV technique, we show that the reduction in exciton diffusion length is directly related to the increase in exciton trap density. As a result, this work brings to light the impact of processing conditions and trap states on the exciton diffusion length. It therefore provides the motivation for futures studied to identify the origin and composition of these trap states. If additional resources were available, guiding questions for future studies related to this work include: (1) What is the origin of these exciton trap states? (2) Are free charge carriers created at these trap sites? (3) How is an exciton trap related to charge trap?

Chapter 5 of this dissertation is driven by two guiding questions: (1) How does the exciton diffusion lengths in high performance OPVs compare? (2) How do exciton trap density relate to the exciton diffusion length and device performance? To answer these questions, we used the BQ-MC and BQ-SV techniques to probe the exciton diffusion length and exciton trap density in several small molecules which have previously shown high device performances. It is found that the exciton diffusion length and exciton trap density varies between 2 − 13 nm and 10^{17} −10^{18} cm^{-3}. We observe a slight correlation between the exciton diffusion length and the exciton trap density. In this work we do not observe a correlation between the 3D exciton diffusion length and device performance. However, increasing the exciton diffusion length would allow for further optimization of other processes thereby enabling greater device efficiencies. For this reason, future works may focus on finding methods to reduce the density of exciton trap sites and extend the exciton diffusion length. If additional resources were available, guiding questions for future studies related to this work include: (1) What caused the differences in exciton diffusion lengths and exciton trap densities in these materials? (2) Would filling trap sites alter the optimal device performance of a material?

In closing, this dissertation has cleared the ambiguities between techniques used to measure exciton diffusion length and has identified specific techniques which are idea for systematic studies of exciton diffusion length. This study has also confirmed that the exciton diffusion length is directly limited by exciton trap states and should be investigated further. These results therefore provide a clear roadmap for future studies which will accelerate the advancement in organic photovoltaic efficiencies thereby brining a clean and renewable energy source closer to our roofs.